GPR wavefield phenomena in the presence of boreholes and permittivity gradients

Thomas Simader

Master's Thesis

Supervisor: Prof. Jan van der Kruk

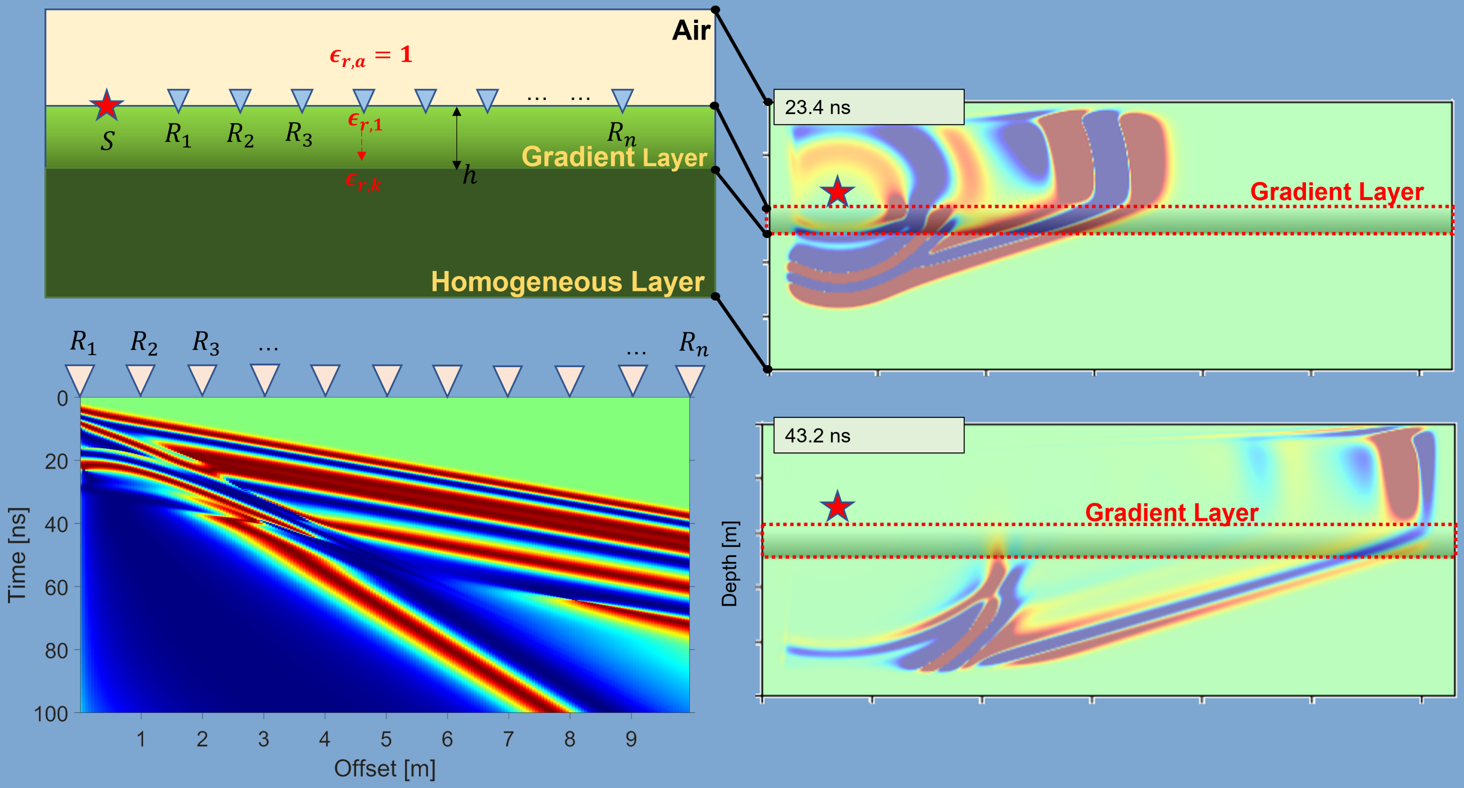

IDEA League

JÜLICH Forschungszentrum

GPR wavefield phenomena in the presence of boreholes and permittivity gradients

by

Thomas Simader

to obtain the degree of Master of Science

at

ETH Zürich, Switzerland

RWTH Aachen, Germany

TU Delft, The Netherlands

to be defended on Wednesday, August 16, 2023, at 10:40am.

Student number:	438470		
Project duration:	March 17, 2023 – August 4, 2023		
Committee members:	Prof. Jan van der Kruk	Research Center Jülich	1st Examiner
	Dr. Ranajit Ghose	TU Delft	2nd Examiner
	Prof. Anja Klotzsche	Research Center Jülich	

Zentrales Prüfungsamt/Central Examination Office

Eidesstattliche Versicherung
Statutory Declaration in Lieu of an Oath

Simader, Thomas

Name, Vorname/Last Name, First Name

438470

Matrikelnummer (freiwillige Angabe)
Matriculation No. (optional)

Ich versichere hiermit an Eides Statt, dass ich die vorliegende Arbeit/Bachelorarbeit/ Masterarbeit* mit dem Titel
I hereby declare in lieu of an oath that I have completed the present paper/Bachelor thesis/Master thesis* entitled

GPR wavefield phenomena in the presence of boreholes and permittivity gradients

selbstständig und ohne unzulässige fremde Hilfe (insbes. akademisches Ghostwriting) erbracht habe. Ich habe keine anderen als die angegebenen Quellen und Hilfsmittel benutzt. Für den Fall, dass die Arbeit zusätzlich auf einem Datenträger eingereicht wird, erkläre ich, dass die schriftliche und die elektronische Form vollständig übereinstimmen. Die Arbeit hat in gleicher oder ähnlicher Form noch keiner Prüfungsbehörde vorgelegen.
independently and without illegitimate assistance from third parties (such as academic ghostwriters). I have used no other than the specified sources and aids. In case that the thesis is additionally submitted in an electronic format, I declare that the written and electronic versions are fully identical. The thesis has not been submitted to any examination body in this, or similar, form.

Aachen, August 3, 2023

Ort, Datum/City, Date

*Nichtzutreffendes bitte streichen
*Please delete as appropriate

Belehrung:
Official Notification:

§ 156 StGB: Falsche Versicherung an Eides Statt
Wer vor einer zur Abnahme einer Versicherung an Eides Statt zuständigen Behörde eine solche Versicherung falsch abgibt oder unter Berufung auf eine solche Versicherung falsch aussagt, wird mit Freiheitsstrafe bis zu drei Jahren oder mit Geldstrafe bestraft.
Para. 156 StGB (German Criminal Code): False Statutory Declarations
Whoever before a public authority competent to administer statutory declarations falsely makes such a declaration or falsely testifies while referring to such a declaration shall be liable to imprisonment not exceeding three years or a fine.
§ 161 StGB: Fahrlässiger Falscheid; fahrlässige falsche Versicherung an Eides Statt
(1) Wenn eine der in den §§ 154 bis 156 bezeichneten Handlungen aus Fahrlässigkeit begangen worden ist, so tritt Freiheitsstrafe bis zu einem Jahr oder Geldstrafe ein.
(2) Straflosigkeit tritt ein, wenn der Täter die falsche Angabe rechtzeitig berichtigt. Die Vorschriften des § 158 Abs. 2 und 3 gelten entsprechend.
Para. 161 StGB (German Criminal Code): False Statutory Declarations Due to Negligence
(1) If a person commits one of the offences listed in sections 154 through 156 negligently the penalty shall be imprisonment not exceeding one year or a fine.
(2) The offender shall be exempt from liability if he or she corrects their false testimony in time. The provisions of section 158 (2) and (3) shall apply accordingly.

Die vorstehende Belehrung habe ich zur Kenntnis genommen:
I have read and understood the above official notification:

Aachen, August 3, 2023

Ort, Datum/City, Date

Unterschrift/Signature

Abstract

Ground penetrating radar (GPR) data has proven to be a powerful tool for non-invasively estimating the electrical properties of the shallow subsurface. Petrophysical relationships allow them to be converted into hydrological parameters such as soil water content (SWC) and porosity. In the presence of thin layers, complex wave phenomena can occur that are usually ignored in standard processing. Recent developments in modeling tools and computation power allow us to include detailed modeling in advanced inversion algorithms, such as full-waveform inversion (FWI). In this thesis, GPR wave phenomena occurring due to the presence of boreholes in crosshole tomography and the presence of permittivity gradients in surface GPR data acquisition will be investigated. First, these phenomena need to be identified and understood so that they can be effectively included in advanced inversion algorithms.

Using the finite difference time-domain solver gprMax, various models with different borehole radii and different permittivity distributions are evaluated. Additionally, a resistor loaded finite-length antenna model is built to compare its radiative properties with a point dipole source in crosshole GPR applications. The results reveal that the differences between these two antenna types are small, but not equal. The dominant factor that influences the radiated wavefields is found to be the properties of the surrounding medium. For increasing vertical offsets, elongated wavetrains are observed, which are probably caused by waveguiding effects of the water-filled boreholes. The permittivity gradient models for surface GPR reveal scenario-dependent phenomena, notably the presence of a lower halfspace ground wave and dispersive wave propagation for increasing and decreasing permittivity gradients, respectively. Overall, the results suggest that integrating parameters into the FWI workflow, which account for surface gradients, could be beneficial and lead to improved imaging capabilities.

Acknowledgements

I am deeply grateful to my supervisor Prof. Jan van der Kruk for his constant support and guidance throughout this project. This thesis would not have been possible without his advice, patience, and motivation. The in-person meetings are particularly highlighted, leaving me motivated and eager to continue my research. I am thankful for the insightful discussions and constant feedback, especially since my background in Electromagnetism was not strong. Eventually, I have no regrets about taking on this challenge.

My gratitude extends to Dr. Johannes Keller for his assistance in setting up the IT framework for running simulations on the supercomputer. Thank you for answering any questions related to IT. Unfortunately, we did not manage to run the inversion with spotpy-gprmax, but I am sure that it will work soon! Additionally, I would also like to thank the JSC of the Research Center Jülich for granting access to JURECA.

To the members of our working group at the IBG3-Institute - Prof. Anja Klotzsche, Dominik Hoven, Sophia Schiebel and Brianna Mueller - thank you for creating a warm and supportive atmosphere which is highly important to be able to focus. Your guidance in both personal and professional matters, along with the help you provided, was truly valuable, not to mention the numerous car rides generously provided from Aachen to Jülich by Dominik.

A special thanks to Dr. Amirpasha Mozaffari for the wonderful box full of interesting books before leaving to continue his career in Barcelona. Additionally, my appreciation goes to Dr. Carsten Sperl for sending me a printed version of his dissertation, considering that creating PDF versions was not a common practice back in 1999. Many aspects of the dissertation were very important to this thesis.

Due to the relatively short project duration, it was natural to feel stressed. Thanks to my friends, for helping me to cope with the pressure and our late-night sessions! I am deeply grateful to my parents for their constant support in every decision I have made so far.

Thomas Simader
Aachen, August 3, 2023

Table of Contents

Nomenclature **xi**

Acronyms **xiii**

1 Introduction **1**

1.1 Motivation: Quantitative estimation of material properties of the vadose zone with geophysical methods . . . 1

1.2 Study goal: Understanding wavefield phenomena in complex structures . . . 2

2 Theory **5**

2.1 EM Basics . . . 5

2.2 GPR . . . 7

2.2.1 Wave propagation regime . . . 7

2.2.2 Penetration depth and resolution . . . 9

2.2.3 Survey modes . . . 10

2.2.4 Homogeneous and inhomogeneous waves . . . 10

2.2.5 Signal propagation on a dielectric halfspace . . . 11

2.2.6 Closed form expressions for DGW and DAW . . . 14

2.2.7 Reflection and transmission . . . 15

2.3 Previous studies assessing gradients using GPR . . . 16

3 Numerical modeling of boreholes and permittivity gradients **19**

3.1 Software: gprMax . . . 19

3.2 Stability criteria . . . 21

3.3 Model of a resistor loaded finite length antenna (RLFLA) . . . 21

3.4 Borehole model . . . 22

3.5 Gradient model . . . 23

3.6 Experimental determination of an appropriate parametrization of the PML region . . . 25

4 Influence of boreholes on crosshole GPR **27**

5 Influence of permittivity gradients on surface GPR **33**

5.1 Simulations in 2D . . . 33

5.1.1 First analysis of trace-normalized B-scans . . . 33

5.1.2 Amplitude analysis . . . 45

5.1.3 Analysis of frequency spectra . . . 46

5.1.4 Hilbert gain reveals more multiples and an additional ground wave . . . 48

5.2 Introduction of a lower halfspace ground wave . . . 50

5.3 Validation with a 3D simulation and finite-length antenna . . . 60

5.4 Summary: Observed wavefield phenomena for different permittivity distributions . . . 61

6 Conclusion and Outlook **63**

Bibliography **65**

List of Figures **71**

List of Tables **73**

A Appendix **A1**
A.1 Soft and hard sources A1
A.2 NMO for a flat reflector A3
A.3 B-scans with gain filter A4

Nomenclature

Conventions

a	Scalar quantity
$\bar{a}$	Vector quantity
$\tilde{a}$	Tensor quantity

Constants

ϵ_0	Permittivity in free space (8.854×10^{-12} F m^{-1})
μ_0	Magnetic permeability in free space ($4\pi \times 10^{-7}$ H m^{-1})
c_0	Speed of light in free space 0.29979 m ns^{-1})
Z_0	Wave impedance in free space ($376.6\,\Omega$)

Electromagnetism

α	Attenuation coefficient [m^{-1}]
ϵ	Permittivity [F m^{-1}]
ϵ_r	Relative permittivity [-]
$\frac{dD}{dt}$	Displacement current density [A m^{-2}]
κ	wavenumber [m^{-1}]
λ	Wavelength [m]
μ	Magnetic permeability [H m^{-1}]
μ_r	Relative magnetic permeability [-]
ω	Angular frequency [Hz]
ρ	Volume charge density [C m^{-3}]
σ	Electrical conductivity [S m^{-1}]
σ^*	Equivalent magnetic loss [Ω m^{-1}]
θ_c	Critical angle [°]
B	Magnetic induction [T or Wb m^{-2}]
D	Electric displacement vector [C m^{-2}]
E	Electric field strength [V m^{-1}]
f	Frequency [Hz]
f_c	Center frequency [Hz]
f_t	Transition frequency to reach the wave-like propagation regime [Hz]
H	Magnetic field strength [A m^{-1}]
J	Current density [A m^{-2}]
j	Imaginary Unit
J_c	Current density (induced current) [A m^{-2}]
J_{ex}	Current density (source) [A m^{-2}]
M	Equivalent magnetic current density [V m^{-2}]
v	Velocity [m s^{-1}]
Z	Wave impedance [Ω]

Numerical modeling

Strong contrast: Permittivity contrast of 5 and 12.5

Weak contrast: Permittivity contrast of 5 and 6

Acronyms

CFL Courant Friedrichs Lewy.

CMP common-midpoint.

DAW direct air wave.

DGW direct ground wave.

EM electromagnetism.

FDTD finite difference time-domain.

FFT fast Fourier transform.

FWI full waveform inversion.

GPR Ground Penetrating Radar.

gprMax simulation software for EM wave propagation.

LHGW lower halfspace ground wave.

NMO normal moveout.

PEC perfect electric conductor.

PML perfectly matched layer.

RLFLA resistor loaded finite-length antenna.

SWC soil water content.

TE transverse electric.

TM transverse magnetic.

WARR wide-angle reflection and refraction.

1

Introduction

The concept of uniformity has its roots in classical Greek philosophy since Aristotle, but its importance to science in the 20th century is largely derived from the works of Newton and Leibniz (Denham, 1982). One fundamental principle is that

> Natura non facit saltus ("Nature makes no jumps"),

as stated by Leibniz in the beginning of the 18th century in the context of infinitesimal calculus (Bell, 2005). The idea was later adopted in geological gradualism. It states that processes or changes in nature do not occur abruptly and suddenly - discontinuously - but rather fundamentally unfold continuously and steadily (Huggett, 1999b). Gradualists explained geological features as the result of slowly acting processes such as erosion, while catastrophists argued that the Earth had been shaped mainly by a series of violent events or catastrophes, either over a relatively short time or over many millions of years (Huggett, 1999a). The idea of gradualism was further developed by Lyell in 1830 to the principle of uniformatism, which is widely accepted today.

This theory suggests that gradual changes in material properties must be present on the Earth. When we try to map the subsurface with geophysical methods, it is often convenient to assume sharp transitions between two materials. Nevertheless, it might be useful to incorporate the inherent gradualism of nature in a priori assumptions.

1.1. Motivation: Quantitative estimation of material properties of the vadose zone with geophysical methods

In recent years, the characterization of the vadose zone has increasingly gained interest. It is often referred to as the unsaturated zone and can reach thicknesses from a few centimeters to several hundred meters (Ojha et al., 2008). However, it is mostly the shallow soil profile that is of the most hydrological importance because it controls various factors such as water storage, movement, run-off and recharge. Consequently, it is a crucial parameter for plant growth. It also regulates the transpiration of plants and plays an important role in dividing the incoming solar energy into sensible and latent heat, thus controlling evaporation (Robinson, 2017).

Ground Penetrating Radar (GPR) has proven to be a very useful noninvasive electromagnetic (EM) method to characterize shallow soil conditions. It offers valuable estimations of soil water content (SWC) and soil hydraulic parameters necessary to understand highly dynamic hydrological processes that naturally occur in soil. SWC is considered as a key factor in agriculture and irrigation management, soil erosion control, rock and soil mechanics, hydrology and water resource management, as well as Earth system modeling (X. Liu et al., 2019).

The basic principle of GPR is sending EM signals into the ground and receiving the impulse response from the subsurface. Inversion schemes allow retrieving the EM property distribution of the ground from the measured signal, mainly the permittivity and conductivity, using the travel time and amplitude information. Next, hydrological parameters, such as SWC and porosity, can be obtained with petrophysical relationships. Inversion tries to estimate a model that can explain the measured data reasonably well. Inversion, nevertheless, is a non-trivial process because it is defined as an ill-posed mathematical problem. In contrast to forward problems, the inverse problem is non-unique, meaning that more than one model can fit the data, and can be unstable (Gosselin et al., 2022). Conventional ray-based techniques only use parts of the measured data and simplified approximations of the reality that can contain relatively large errors (Meles, 2011). In recent years, the well-known concept of full waveform inversion (FWI) from the seismic community has been applied also to GPR data. It overcomes the limitations of ray-based inversion by applying accurate forward modeling and using significant parts of the measured data to return reliable quantitative estimates of both permittivity and conductivity. Significant milestones have been reached by Busch et al. (2012), Ernst (2007), Klotzsche et al. (2010), Meles et al. (2010), and van der Kruk et al. (2018).

For example, Busch et al. (2014) showed that FWI can reliably map EM properties of the shallow subsurface compared to conventional measuring instruments. The subsurface was approximated with a homogeneous halfspace in the study. In general, many inversion schemes are based on the assumption of a ”horizontally layered model of the subsurface” (Busch, 2014). However, as indicated in the beginning, subsurface deposits can show a gradual shift in petrophysical characteristics both at the contact zone or transition zone (steep gradient) and inside a layer (smooth gradient) (Hanafy & al Hagrey, 2006). For instance, van der Kruk (2001) noticed an along depth increasing permittivity when analyzing soil samples in the upper 50 cm of a pit. Especially the physical properties of the shallow subsurface experience fluctuations over both short and large time scales. Temperature can significantly vary within the first decimeters along diurnal and seasonal cycles (Bonan, 2019). Although permittivity tends to increase with decreasing temperature, this temperature dependence is neglected in many practical GPR applications (Cassidy, 2009). Additionally, infiltration and run-off events can create smooth permittivity profiles, as shown by Mangel et al. (2015) and Klenk et al. (2015). Steelman and Endres (2010) demonstrated experimentally that ”significant variations can occur in the nature of the near-surface EM wavefields over both long and short time scales”.

1.2. Study goal: Understanding wavefield phenomena in complex structures

In the context of examining realistic wavefield phenomena, we will first explore the impact of water-filled boreholes on the shape of the received wavelet for crosshole GPR. This study builds upon the preliminary research project module, which is conducted to familiarize ourselves with the fundamental theory of the thesis topic before its official start. It involves constructing a model of finite-length antennas in a finite difference model. This research is particularly important as finite-length antennas are being utilized in inversion techniques for ongoing projects at the Research Centre Jülich. It will be a minor chapter within this thesis.

Additionally, in times when a quantitative retrievement of hydrological properties has gained a lot of interest, maybe the smooth variation of hydrogeophysical properties should be included in the forward modeling of inversion schemes. In this project, as a preliminary study, we want to focus on the effect of smooth permittivity gradients on the received wavefields for surface GPR. We want to use forward models to explain wavefield interactions and setups in complex environments based on physical equations. For this, we evaluate forward models containing different permittivity distributions in the shallow subsurface. In particular, we want to find typical phenomena and patterns for smooth permittivity distributions that allow a first-estimate categorization and identification of the gradient and the involved phenomena.

Structure of the thesis The thesis begins with an overview of EM principles, followed by an introduction to GPR in chapter 2. Chapter 3 discusses the finite difference time-domain (FDTD) method and introduces the forward simulation software gprMax. Additionally, this chapter presents the numerical models for the finite length antenna, crosshole, and surface GPR. Moving on to chapter 4, the results for the borehole model are presented and discussed. In chapter 5, the simulation results and analysis for permittivity gradients are shown and discussed. Finally, chapter 6 provides the conclusion and outlook.

2

Theory

2.1. EM Basics

The famous Maxwell's equations describe EM wave propagation. Maxwell summarized the work of various researchers in the compact form of four equations. Before him, light and electromagnetic effects were two independent phenomena. He was one pioneer to unify these relationships which are fundamental for classic EM theory, ranging from induction, radio waves, resistivity, circuit theory, etc. (Basu & Dhasmana, 2023). In this work, special focus on GPR antenna radiations towards a soil environment will be given.

Maxwell's modified circuit Law:

$$\bar{\nabla} \times \bar{H} = \frac{\partial \bar{D}}{\partial t} + \bar{J}, \tag{2.1a}$$

Faraday's Law of Induction:

$$\bar{\nabla} \times \bar{E} = -\frac{\partial \bar{B}}{\partial t} - \bar{M}, \tag{2.1b}$$

Gauss' theorem in electrostatics:

$$\bar{\nabla} \cdot \bar{D} = \rho, \tag{2.1c}$$

Gauss' theorem in magnetostatics:

$$\bar{\nabla} \cdot \bar{B} = 0, \tag{2.1d}$$

where

$\bar{H}$ = Magnetic field strength vector [$\mathrm{A\,m^{-1}}$],
$\bar{D}$ = Electric displacement vector [$\mathrm{C\,m^{-2}}$],
$\bar{J}$ = Current density vector [$\mathrm{A\,m^{-2}}$],
$\bar{E}$ = Electric field strength vector [$\mathrm{V\,m^{-1}}$],
$\bar{M}$ = Equivalent magnetic current density [$\mathrm{V\,m^{-2}}$],
$\bar{B}$ = Magnetic flux density vector [T or $\mathrm{Wb\,m^{-2}}$],
ρ = Volume charge density [$\mathrm{C\,m^{-3}}$].

The current density vector consists of two terms $\bar{J} = \bar{J}_c + \bar{J}_{ex}$, where $\bar{J}_c$ denotes the conduction (induced) current density and $\bar{J}_{ex}$ the external or impressed (source) current density. Similarly, the magnetic current density vector $\bar{M} = \sigma^* \bar{H} + \bar{M}_{ex}$ consists of two terms, where σ^* [$\Omega\,\mathrm{m^{-1}}$] is the equivalent magnetic loss and $\bar{M}_{ex}$ the source. The Maxwell equations demonstrate how the electric and magnetic fields are interrelated and how they are generated by the source terms (Meles, 2011).

The associated constitutive relationships introduce the material properties ϵ,σ, and μ, which are needed to describe a material's response to an applied EM field. While Maxwell's equations mathematically describe the physics of EM fields, Eqs. (2.2) to (2.4) quantify material properties. Combining both provides the foundation for quantitatively describing GPR signals:

$$\bar{D} = \tilde{\epsilon}\bar{E}, \tag{2.2}$$
$$\bar{J}_c = \tilde{\sigma}\bar{E}, \tag{2.3}$$
$$\bar{B} = \tilde{\mu}\bar{H}, \tag{2.4}$$

where

$\tilde{\epsilon}$ = Dielectric permittivity [F m^{-1}],
$\tilde{\sigma}$ = Electrical conductivity [S m^{-1}],
$\tilde{\mu}$ = Magnetic permeability [H m^{-1}].

Dielectric permittivity characterizes the response of charges confined within a material structure when an electric field is present. Although bound charges cannot move freely, they still undergo a slight displacement in response to an alternating electric field. When the resulting internal electric field counterbalances the external electric field, the charges reach a state of equilibrium and stop moving (Olhoeft, 1998). This separation of charges is known as polarization and can be of various types (for example elliptical, linear, or circular [1]). When the external field is removed, the stored energy is released, causing the charges to move back to their original positions. The displacement and polarization processes store electric field energy, and the amount stored during each cycle of the alternating electric field determines the real part of the dielectric permittivity. It is often expressed relative to the dielectric permittivity of free space, see Eq. (2.5). Additionally, a small amount of energy is dissipated as heat as a result of resistance in charge transport during displacement. The extent of energy dissipation determines the imaginary component of the dielectric permittivity (Neal, 2004).

$$\epsilon_r = \frac{\epsilon}{\epsilon_0}, \tag{2.5}$$

where

$\epsilon_0 = 8.854 \times 10^{-12}$ F m^{-1} (permittivity of free space).

Electrical conductivity In the presence of an electric field, σ characterizes the movement of free charges and accounts for part of the dissipation (conduction loss) of energy (Annan, 2009). In addition to the charge motions associated with polarization phenomena, these motions occur throughout each half cycle of an alternating electric field, regardless of its frequency. Regarding GPR, the most significant energy losses based on conduction arise from ionic charge transport in water and electrochemical processes related to cation exchange in clay minerals (Neal, 2004).

Magnetic permeability is analogous to the dielectric permittivity and quantifies the storage and dissipation of magnetic field energy through induced magnetization. Similar to dielectric permittivity, magnetic permeability can be divided into its real and imaginary components and is often expressed relative to the magnetic permeability of free space (Neal, 2004). Often, μ is simplified to be equal to the value of the free space $\mu_0 = 1.26 \times 10^{-6}\,\mathrm{H\,m^{-1}}$. In the presence of ferromagnetic materials, this simplification may no longer be valid (Olhoeft, 1998).

---

[1] A detailed description of polarities is given in Annan (2005)

The material properties are tensor quantities and can be nonlinear, e.g. $\tilde{\sigma} = \tilde{\sigma}(E)$. In this work, the three quantities are treated as scalar quantities, as is common practice in the GPR community, where σ and ϵ are the most important ones. A list of some typical ranges of these material properties is given in Table 2.1. In particular, the presence of water ($\epsilon_r \approx 80$) in a material can have a huge impact on its bulk permittivity values.

Material	Static conductivity	Relative permittivity
Air	0	1
Clay-dry	1-100	2-20
Clay-wet	100-1000	15-40
Concrete-dry	1-10	4-10
Concrete-wet	10-100	10-20
Freshwater	0.1-10	78 (25deg) - 88
Freshwater Ice	0.000001-1	3
Seawater	4000	81-88
Seawater Ice	10-100	4-8
Sandstone-dry	0.001-0.0000001	4-7
Sandstone-wet	0.01-0.001	5-15
Shale-saturated	10-100	6-9
Sand-dry	0.0001-1	3-6
Sand-wet	0.1-10	10-30

Table 2.1: Typical values of relative permittivity (real component) and static conductivity for common subsurface materials at an antenna frequency of 100 MHz (after Cassidy, 2009).

2.2. GPR

Ground Penetrating Radar (GPR) is a high-resolution geophysical technique that offers imaging capabilities utilizing the propagation of high-frequency EM waves. This method enables the visualization of subsurface structures by detecting variations in dielectric properties. GPR operates by emitting a transient EM pulse into the ground through an antenna, typically with a center frequency ranging from 10 MHz to 2000 MHz. Abrupt changes in dielectric properties cause reflections back to the surface, which are captured by the receiving antenna. The recorded signal, measured in terms of amplitude and polarity relative to travel time, can provide valuable information about the subsurface.

2.2.1. Wave propagation regime

Eqs. (2.1a) to (2.1d) describe the coupled relationship between electric and magnetic fields varying in time. When electric fields change, they create magnetic fields, which, in turn, induce electric fields. This continuous interplay between the two fields results in their movement through space. These fields may diffuse or propagate as waves, depending on the extent of losses. In GPR applications, we are primarily interested in wave-like behavior at high frequencies (Rubin & Hubbard, 2005).

At low frequencies, the wave properties (ϵ, σ, and μ) are frequency-dependent, which indicates a diffuse field behavior. At high frequencies, those properties become more or less frequency-independent, leading to a propagation, non-dispersive character. This is of great importance to GPR applications. In the following, we assume the frequencies to be high enough to be in the wave-like propagation regime.

For a simple material, the transition frequency f_t to reach this regime is defined as (Annan, 2009):

$$f_t = \frac{\sigma}{2\pi\epsilon}. \tag{2.6}$$

Nevertheless, as the frequency increases, both velocity and attenuation will also increase in any physical situation. For most GPR problems, changes in attenuation are more significant than changes in velocity (Annan, 2005).

The wave character can be seen by looking at the EM wave equation for a charge-free ($\rho = 0$) and external source-free medium. Taking the curl of Faraday's law in Eq. (2.1b), substituting with Eq. (2.1a) and using the constitutive relation yields (Kamberaj, 2022):

$$\bar{\nabla} \times \bar{\nabla} \times \bar{E} + \mu\sigma \cdot \frac{\partial \bar{E}}{\partial t} + \mu\varepsilon \cdot \frac{\partial^2 \bar{E}}{\partial t^2} = 0. \tag{2.7}$$

In Eq. (2.7), the second term is related to the energy dissipation and the third term to the energy storage whose time-varying circulation creates an electric field as expressed in the first term. GPR is most effective when energy dissipation is small, which leads to a higher penetration depth (see section 2.2.2).

The velocity v of electromagnetic waves in a host material is (Neal, 2004):

$$v = \frac{c}{\sqrt{\varepsilon_\mathrm{r}\mu_\mathrm{r}\frac{1+\sqrt{1+(\sigma/\omega\varepsilon)^2}}{2}}}. \tag{2.8}$$

In low loss conditions ($\sigma << \omega\epsilon$) and assuming non-magnetic materials, Eq. (2.8) reduces to

$$v = \frac{c_0}{\sqrt{\epsilon_r}}, \tag{2.9}$$

where v is

$$v = \lambda \cdot f. \tag{2.10}$$

This is a common approximation for most GPR applications. It is evident that an increasing permittivity of soil leads to a decreasing propagation velocity of the EM waves.

When a EM wave travels through space, its amplitude A declines exponentially from its initial A_0 with distance z in the form of:

$$A = A_0 \exp(-\alpha z). \tag{2.11}$$

The attenuation coefficient α is defined as (Sperl, 1999):

$$\alpha = \omega\sqrt{\varepsilon\mu\frac{\sqrt{1+(\sigma/\omega\varepsilon)^2}-1}{2}}. \tag{2.12a}$$

for low loss materials it reduces to

$$\alpha = \frac{\sigma}{2}\sqrt{\frac{\mu}{\epsilon}}. \tag{2.12b}$$

It is important to note that the attenuation is proportional to the electrical conductivity. The reciprocal of Eq. (2.12b) is commonly referred to as the skin depth, which is the depth at which the $\bar{E}$ field amplitude has decayed to e^{-1} compared to its initial amplitude. In the context of GPR, the most significant conduction-based losses are caused by ionic charge transport in water and electrochemical processes associated with cation exchange on clay minerals (Ruffet et al., 1995).

Other important processes related to a decrease in signal strength are spherical spreading of the energy, reflection/transmission losses at interfaces and scattering of energy. Scattering losses are especially significant if objects have a dimension similar to the wavelength, and are therefore most pronounced for higher frequencies (Annan, 2005).

2.2.2. Penetration depth and resolution

The penetration depth is primarily controlled by the GPR center frequency, electrical conductivity and the attenuation of the subsurface deposits. In deposits with low losses (resistive deposits), the choice of the center frequency in the GPR affects the penetration depth. Lower frequencies achieve higher penetration depths, while higher frequencies result in shallower penetration (Annan, 2005).

It is convenient to separate resolution into two components: longitudinal or temporal resolution Δr, which refers to resolution in range or depth, and lateral resolution Δl, see Fig. 2.1. The Rayleigh criterion relates the ability to distinguish between two closely spaced reflectors as

$$\Delta r \geq \frac{\lambda}{4}, \tag{2.13}$$

where λ is the dominant wavelength. On the other hand, lateral resolution refers to the ability to distinguish between two scatter points separated by a specific horizontal distance under the source-receiver center point. It is closely connected to the radius of the first Fresnel zone, leading to (Annan, 2005):

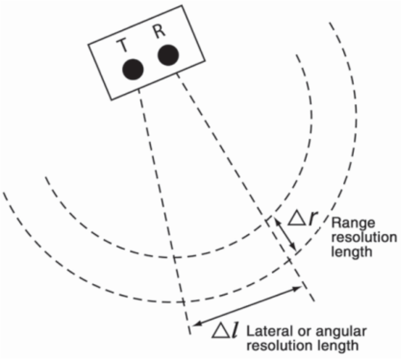
T
R
Δr Range resolution length
Δl Lateral or angular resolution length

Figure 2.1: GPR resolution can be divided into two parts: range resolution and lateral or angular resolution (Annan, 2005).

$$\Delta l \geq \sqrt{\frac{d\lambda}{2}}, \tag{2.14}$$

where d is the vertical depth. The term bandwidth is related to the frequency spectrum ranging from -3 dB $(50\,\%)$ to the center frequency f_c of the signal. Eqs. (2.13) and (2.14) are valid assuming that the ratio of bandwidth to f_c is approximately one (Annan, 2005). From Eqs. (2.13) and (2.14) it becomes evident that there must be a trade-off between archiving a high penetration depth and acquiring the desired resolution. High frequency components experience a higher attenuation, making the subsurface act as a low pass filter. On the other hand, high frequencies lead to smaller wavelengths, which leads to a higher resolution.

2.2.3. Survey modes

There exist different survey modes to conduct a GPR survey, which can generally be differentiated into surface, crosshole, and off-ground applications. In this thesis, we examine surface GPR (top row in 2.2) and crosshole GPR (bottom row in 2.2).

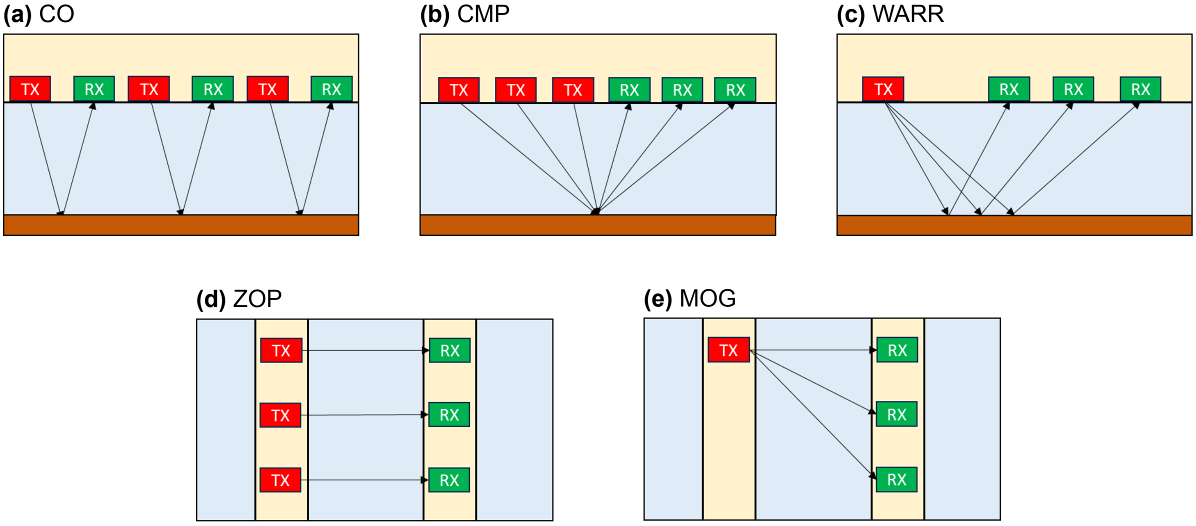

Figure 2.2: Typical surface (upper row) and crosshole (bottom row) GPR survey modes (adapted from Zhang et al., 2022). Tx denotes the transmitter and Rx the receiver.

For surface GPR, a common-offset (CO) configuration means that the antennas are deployed in a fixed geometry, such as antenna separation, orientation, and polarization. Measurements are made at regular spatial intervals, where both the receiver and the transmitter are moved. Often, CO is used for imaging purposes or if advanced data processing is applied. In a common midpoint (CMP) survey, the antenna separation is increased for each recording, while they are kept over a common mid-point. This can be useful for estimating the radar signal velocity versus depth in the ground. Wide-angle reflection and refraction (WARR) keep the position of the transmitter fixed while moving the receiver (Annan, 2009).

The survey modes relevant crosshole GPR will be further discussed in chapter 4.

2.2.4. Homogeneous and inhomogeneous waves

In surface GPR, dipole antennas are often used to generate spherical waves that radiate into the subsurface. It is useful to examine the reflection and refraction that occur at the air-soil interface to understand the wave types generated by a GPR antenna. The radiated spherical wavefront can be described by a superposition of homogeneous and inhomogeneous planar wavefronts (Sperl, 1999). When finite source dimensions and wavelengths are ignored, each point along the air-soil interface can be locally seen as a planar wave impinging at a certain incidence angle. Consider a wave propagating in horizontally layered media from a medium with v_1 to a medium with v_2 where $v_1 > v_2$, see Fig. 2.3. Incident signals can hit the interface at any angle θ_1 between $0°$ and $90°$. According to Snell's law in Eq. (2.15), the angle θ_2 is then limited for $0 < \theta_2 < \theta_c$, where θ_c is the critical angle (Annan, 2005):

$$\frac{\sin\theta_1}{\sin\theta_2} = \frac{v_1}{v_2} = \frac{\sqrt{\epsilon_2}}{\sqrt{\epsilon_1}}, \tag{2.15}$$

if $\theta_1 = 90°$

$$\theta_c = \sin^{-1}\frac{\sqrt{\epsilon_1}}{\sqrt{\epsilon_2}}. \tag{2.16}$$

Thus, the maximum angle that a signal can be refracted down occurs for $\theta_2 = \theta_c$ when it propagates horizontally in medium 1. In case a signal travels upward from medium 2 at $\theta_2 = \theta_c$, the refracted signal travels horizontally in medium 1. If $\theta_2 > \theta_c$, then $\sin\theta_1$ must be greater than 1 which is not possible for real angles. This leads to θ_1 being a complex angle with a pure imaginary cosine (Jackson & Müller, 2020):

$$\cos\theta_1 = -j\sqrt{\left(\frac{\sin\theta_2 v_2}{v_1}\right)^2 - 1} = -j\sqrt{\left(\frac{\sin\theta_2}{\sin\theta_c}\right)^2 - 1}. \tag{2.17}$$

Physically, this means that the refracted wave propagates along the interface and exponentially decays in the direction of the faster medium (Jackson & Müller, 2020). The refracted wave according to Eq. (2.17) is inhomogeneous and called an evanescent wave, which only exists at the boundary between materials or in the vicinity of localized field sources. The reflected wave undergoes total reflection. (Annan, 2005).

If $v_1 < v_2$, a homogeneous planar wave can be transformed into an inhomogeneous planar wave. Also, if $v_1 > v_2$, an inhomogeneous planar wave can be transformed into a homogeneous planar wave for angles greater than θ_c (Du, 1996 as cited in Sperl, 1999, p.30).

The relationship of amplitudes of the reflected and refracted parts in Fig. 2.3 is discussed in section 2.2.7.

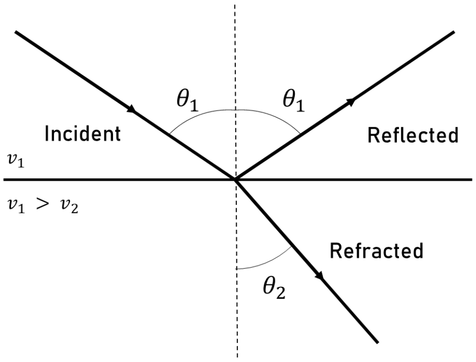

Figure 2.3: When the wave passes from one medium to another medium with a different velocity, it undergoes refraction at the interface. Due to the lower velocity in the second medium, the angle of refraction becomes smaller than the angle of incidence (adapted from Kearey et al., 2013).

2.2.5. Signal propagation on a dielectric half-space

Whereas propagation in a homogeneous space is rather straightforward, signal propagation in a dielectric half-space is more complicated. The radiation pattern is schematically depicted in Fig. 2.4 for the case when the source is placed directly at the air-soil interface. One spherical wave is radiated in air, labeled (1) in Fig. 2.4. On the ground, the signal divides into two components. One component takes the form of a spherical wave (2) that expands outward in all directions (Huisman et al., 2003). One part of the spherical wave (2) is caused by incident homogeneous waves and can be present only for angles smaller than the critical angle θ_c (Sperl, 1999). For a homogeneous soil having a permittivity $\epsilon_r = 5$, this leads only to $\theta_c = 26.6°$. According to the transformations explained in the previous section, the incident inhomogeneous waves can reach refractive angles higher than θ_c, causing refracted homogeneous waves in the soil. One part of an inhomogeneous incident wave transformed into a homogeneous of (2) traveling along the air-soil interface is called the direct ground wave (DGW). However, this signal is not measured by the GPR receiver. Instead, it measures the evanescent (inhomogeneous) air wave raised by the ground wave (3). This wave needs to fulfill the EM boundary conditions: The electric and magnetic fields in the plane of the interface must be the same on either side of the boundary. Additionally, the electric current and magnetic flux density crossing the boundary must be the same on either side of the boundary (Annan, 2005). Thus, (3) has the same amplitude and velocity as the ground wave. Due to its evanescent nature, its amplitude decays exponentially with distance above the surface (Sperl, 1999). The other component (4) travels as a planar wave-front at the critical angle θ_c for a lossless medium linking (2) and (1) due to the continuity requirement for EM fields at an interface (Annan, 2009).

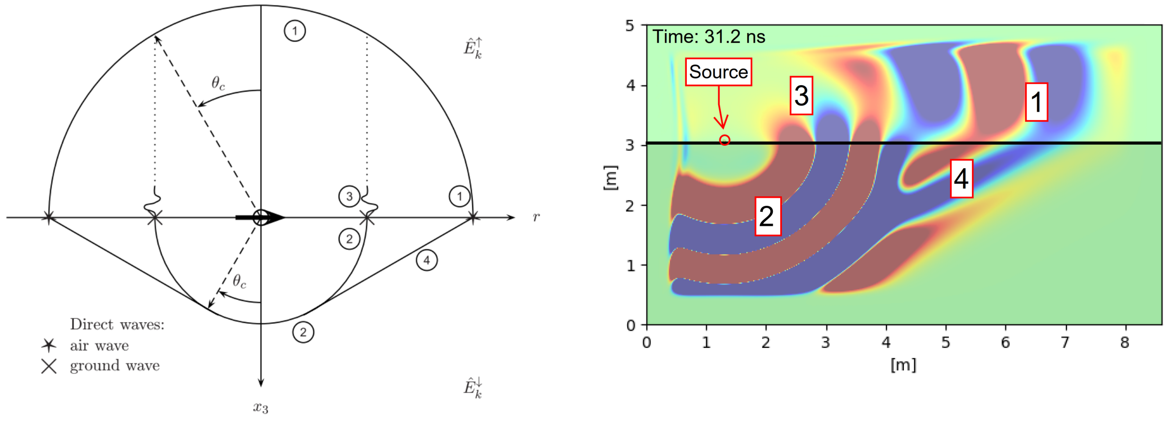

(a) Schematic example from (van der Kruk, 2001) for the spreading of wavefronts.

(b) Snapshot at 31.2 ns from a source placed close to an homogeneous halfspace with $\epsilon_r = 5$. The interface is marked with a bold black line.

Figure 2.4: Waves spreading out from a source located on the air-soil interface.

1. spherical air wave,
2. spherical ground wave,
3. inhomogeneous wave in air,
4. head wave in subsurface.

When placing a receiver next to the antenna, several propagation paths are possible, as indicated in Fig. 2.5a. Direct waves, either the direct air wave (DAW) or direct ground wave (DGW), travel in a straight path between transmitter and receiver. The velocity of the former is $c_0 = 0.3\,\mathrm{m\,ns^{-1}}$ and the latter travels at the velocity of the near-surface soil. However, the exact sensing depth of the ground wave is not trivial, as will be explained in the next paragraph. A contrast in EM properties in the subsurface will additionally generate reflected and refracted waves. Critical airwave refractions occur when the reflected energy at θ_c returns to the surface. They are often seen in GPR data as events having an airwave velocity, but which arrive later than the DAW. If the underlying medium has a higher velocity than the overlying one, refracted energy travels along the underlying layer and can arrive at the receiver before the reflected wave at longer antenna offsets (Grote et al., 2003). Fig. 2.5b shows a so-called B-scan of the waves traveling in Fig. 2.5a, which is a collection of time-dependent data from the receiver points along the surface (trace or A-scan).

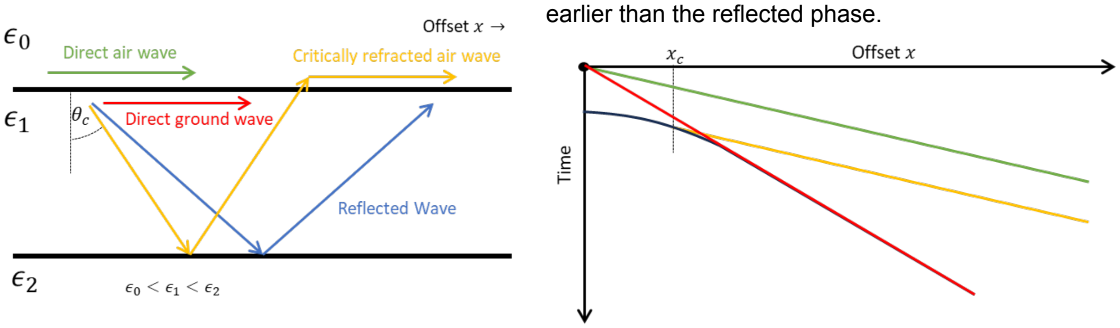

(a) Raypaths are often used to describe the waves traveling from the source to the receiver.

(b) The arrival times are plotted against the separation between the source and receiver. x_c is referred to as the critical distance, where the refracted phase arrives earlier than the reflected phase.

Figure 2.5: Typical ray paths (a) and corresponding B-scan (b), adapted from Annan (2005).

Direct ground wave (DGW) The groundwave travels at the velocity of the near-surface soil, so it arrives at the receiver after the airwave. As direct waves have a linear relationship between travel time t and offset x, their velocity can be estimated as $v = \Delta x/\Delta t$ when using a multi-offset configuration. Assuming a homogeneous soil, Eq. (2.9) can be used to estimate the permittivity of the near subsurface from the DGW (Grote et al., 2003).

Practically, it can be challenging to determine the exact depth of influence or sampling depth z_s of the DGW. Grote et al. (2010) collected approaches from several researches to characterize z_s.

Some approximate z_s with up to half the Fresnel zone, as commonly accepted for seismic ground waves: $z_s = 0.5 \cdot \sqrt{\frac{vd}{f_c}}$, where v is the EM velocity of the soil, d the separation distance between the transmitting and receiving antennas, and f_c the central frequency of the GPR signal. From this equation, it follows that z_s increases with larger offsets and decreases with increasing SWC. Other researchers suggest that z_s depends on the wavelength λ and is not affected by d, such as the approximation from Du (1996) suggesting that the sampling depth ranges from a half wavelength to a full wavelength. The empirical approximation from Sperl (1999) is $z_s = 0.145\sqrt{\lambda}$, where different linearly increasing permittivity gradients were used. Sperl defined z_s as the depth within one layer which significantly determines the velocity of the groundwave.

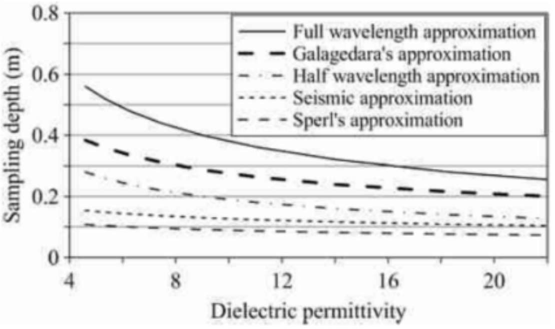

Figure 2.6: Predicted sampling depths z_s of DGW for 250 MHz antennas vary among different models (Grote et al., 2010).

Galagedara et al. (2005) approximation was derived by experimentally reducing the thickness of a wet soil overlying a thick very dry layer. The z_s was derived where the DGW velocity differed 5% from the velocity of a wave traveling only in the upper layer. The derived expression is $z_s = 0.6015\lambda + 0.0468$.

Fig. 2.6 shows the predicted sampling depth for the different approximations. The variations of the models are especially noticeable when dealing with low permittivity. Nevertheless, f_c varies significantly in air and soil, as will be shown in section 5.1.1. Neither approximation specifies which frequency to use, but mostly the central frequency of the antenna as stated by the GPR equipment manufacturer is used (Grote et al., 2010). Grote et al. (2010) experimentally determined z_s for dry and saturated sand for three frequencies and varying thicknesses above a constant base layer. After analyzing the data, z_s appears to be frequency dependent, with a negative correlation between the central frequency and the sampling depth.

It should be noted that there is no consensus within research about the sampling depth z_s. The approximations use different models and assumptions to determine z_s. Especially in heterogeneous scenarios the true sampling depth might differ significantly. In chapter 5, a more detailed look will be held on the generation of the DGW.

2.2.6. Closed form expressions for DGW and DAW

Closed-form expressions for the DAW and DGW radiated from an infinitesimal point source close to a homogeneous halfspace were provided by van der Kruk and Slob (2002). When the source and receiver are both oriented perpendicular to the plane of incidence, this is called a broadside configuration or transverse electric (TE) mode. This refers to the orientation of the electric field vector to the plane of incidence. Analogously, in an endfire configuration, the transverse magnetic (TM) mode refers to the orientation of the magnetic field with respect to the plane of incidence (van der Kruk et al., 2010). This decomposition is strictly dependent on the interface geometry and is not related to the EM fields specifically (Annan, 2005).

The expressions in the time domain are

$$E^{DAW}(x;t) = \frac{Z_0}{2\pi(1-\varepsilon_r)|x|^2} W\left(t - \frac{|x|}{c_0}\right), \tag{2.18}$$

$$E^{DGW}(x;t) = \frac{-\sqrt{\varepsilon_r} Z_0 \exp\left(-\frac{\sigma Z_1}{2}|x|\right)}{2\pi(1-\varepsilon_r)|x|^2} W\left(t - \frac{|x|}{c_1}\right), \tag{2.19}$$

where

x = distance from source to reciever along survey direction,
$W(t)$ = Initial wavelet at the feedpoint in the middle of the antenna,
$Z_0 = \sqrt{\frac{\mu_0}{\varepsilon_0}}$,
$Z_1 = \frac{Z_0}{\sqrt{\varepsilon_r}}$,
$c_0 = \frac{1}{\sqrt{\varepsilon_0 \mu_0}}$,
$c_1 = \frac{c_0}{\sqrt{\varepsilon_r}}$.

These expressions are valid assuming a high frequency approximation $(1 >> \sigma_1/\omega\epsilon_1)$ and a large-offset (far field) approximation. It can be seen in Eqs. (2.18) and (2.19) that both fields are proportional to the receiver offset $|x|^{-2}$ and can best be described as spherical waves traveling through the air-soil interface instead of lossy waves propagating at the interface. Furthermore, the attenuation factor $\exp(-\sigma Z_1 |x|/2)$ in Eq. (2.19) depends on both electrical permittivity and conductivity. Whereas a higher conductivity leads to a stronger decay, a higher permittivity leads to a lower decay. The amplitude attenuation relationship can be used to determine the conductivity, provided that the velocity of the ground wave is known. The wavelet shapes that propagate along the air-ground interface are similar to the initial wavelet $W(t)$; however, the ground wavelet undergoes a polarity reversal of $180°$ due to the minus sign in Eq. (2.19) (van der Kruk & Slob, 2002).

2.2.7. Reflection and transmission

According to Snell's law introduced in Eq. (2.15), the incidence of an EM wave on a laterally extended interface between two media with a sudden change of electrical properties generates a reflected and a refracted wave. The EM boundary conditions require:

$$I_m + R_m I_m = T_m I_m, \tag{2.20}$$

where

m = subscript for either TE or TM mode,
I = incident field strength (either electric or magnetic),
R = reflection coefficient,
T = transmission coefficient.

Both the reflection and transmission coefficient can be described by the Fresnel equations (Annan, 2005):

$$R_{\mathrm{TE}} = \frac{Y_1 \cos\theta_1 - Y_2 \cos\theta_2}{Y_1 \cos\theta_1 + Y_2 \cos\theta_2}, \tag{2.21a}$$

$$R_{\mathrm{TM}} = \frac{Z_1 \cos\theta_1 - Z_2 \cos\theta_2}{Z_1 \cos\theta_1 + Z_2 \cos\theta_2}, \tag{2.21b}$$

$$T_{\mathrm{TE}} = 1 + R_{\mathrm{TE}} = \frac{2Y_1 \cos\theta_1}{Y_1 \cos\theta_1 + Y_2 \cos\theta_2}, \tag{2.21c}$$

$$T_{\mathrm{TM}} = 1 + R_{\mathrm{TM}} = \frac{2Z_1 \cos\theta_1}{Z_1 \cos\theta_1 + Z_2 \cos\theta_2}, \tag{2.21d}$$

where $Z = Z_0/\sqrt{\epsilon}$ denotes the impedance and Y the admittance, which is the reciprocal of Z. For a normal incidence angle ($\theta_1 = 0$) and assuming low loss and non-magnetic conditions, the reflection coefficients for the two modes are indistinguishable:

$$R \approx \frac{v_2 - v_1}{v_2 + v_1} \approx \frac{\sqrt{\epsilon_1} - \sqrt{\epsilon_2}}{\sqrt{\epsilon_1} + \sqrt{\epsilon_2}}. \tag{2.22}$$

When evaluating Eqs. (2.21a) to (2.22), four important points should be considered (Annan, 2005):

1. The reflection magnitude becomes larger at larger angles.
2. For a TM mode, the reflection coefficient can reach zero for a certain angle of incidence. This angle is known as the Brewster angle.
3. When waves transition from a low velocity to a high velocity medium, the reflection coefficients reach a value of one for angles beyond the critical angles. This results in a complete reflection of the waves. However, as explained earlier, fields do exist in the other material but exhibit characteristics of evanescent waves.
4. The sign of the reflection coefficients can be either positive or negative. A positive reflection coefficient means that the reflected fields are in the same direction as the incident field, while a negative coefficient is associated with a polarity reversal.

Reflected GPR signals exhibit varying wavelet shapes, primarily influenced by the electrical properties, composition, shape, and size of the target. Additionally, wavelet shapes are influenced by the contrast in dielectric properties between the target and the surrounding background material (Zadhoush & Giannopoulos, 2022). When a layer is significantly thinner compared to all wavelengths present in the incident signal, the reflected signal resembles the time derivative of the incident signal. The amplitude is multiplied by a constant that linearly depends on layer thickness. For a complete derivation, please refer to the work of Annan (2005).

2.3. Previous studies assessing gradients using GPR

In civil engineering, the use of GPR is of interest because the acquired data can provide important information about structural details and material properties of the inspected object. Recent research has focused on concrete constructions and bituminous pavements.

For example, Benedetto and Pajewski (2015) show a core taken from a subbase slab made of cement-stabilized sand whose permittivity monotonically increases from 3.8 to 5 along its length of 20 cm. When performing 1D simulations of the concrete slab, the shape, and amplitude of the surface reflection depend on the center frequency of the emitted antenna signal, although the medium is non-dispersive. We will investigate WARR surveys where not only surface reflections are recorded.

Hugenschmidt and Loser (2008) added different concentrations of chloride to a concrete sample with a metal plate at the bottom and stored them at different relative humidities for 97 days. They showed that the reflection amplitudes on the concrete surface increased with increasing moisture and chlorides, whereas the amplitudes on the bottom of the specimen decreased. The ratio of both amplitudes revealed a relationship between moisture and chloride content. Kalogeropoulos et al. (2011) continued the research and introduced an FWI approach to assess chloride gradients in concrete. Research from Hugenschmidt and Loser (2008) had been done assuming a homogeneous chloride distribution inside the specimen. Investigating chloride gradients over the element thickness is an important step because they occur in reality. The gradients are caused by capillarity and diffusion processes within the pores caused by atmospheric conditions. The chloride contents from the measurements were in agreement with the conductivity gradient from inversion results. The forward model and inversion assume only a conductivity gradient and a constant permittivity. In this work, we will focus on the effects of permittivity gradients.

Chinh Mai (2022) studied with numerical simulations the effect caused by linearly increasing permittivity gradients on the GPR signal. Gradients simulate real conditions in concrete, as shown by Kalogeropoulos et al. (2011). The main findings are that increasing the gradient thickness by adding thin permittivity layers results in a drop in the estimated velocity of the DGW. When a certain permittivity gradient thickness is reached, the estimated DGW velocity remains invariant with respect to the gradient thickness.

When it comes to the subsurface, there often is a smooth nature of water content profiles (Mangel et al., 2017). In case of an infiltration event, the water content decreases with depth, leading to a decreasing permittivity gradient. Mangel et al. (2017) showed that when the wetting front is in the shallow subsurface, shallow reflections occur that interfere with the ground wave. This leads to difficulties in separating the reflection from the ground wave. Also, according to Snell’s law, the critical angle is reached at relatively low values due to the high velocity contrast between the saturated and unsaturated layers. The resulting total internal reflection traps the wave within the shallow wetted zone, which acts as a waveguide. Waveguides cause dispersion that results in frequency-dependent velocities in the GPR signal. Constructive interference of the critical reflections can cause late-arrival, high-amplitude events in the data. A more detailed explanation of waveguides is given in section 5.1.1. Mangel et al. (2015) demonstrated that assuming a layered structure in the inversion scheme only represents the average variability of the SWC in each layer. However, the wetting front varies with depth due to capillary effects. The information content of dispersive data allows modeling the permittivity variations as a piecewise-linear model that better reproduces the water content variability. The method was validated in an infiltration experiment and showed potential to monitor dynamic shallow subsurface hydrologic events.

Dagenbach (2012) investigated the effect of permittivity gradients present in the capillary fringe zone. This zone refers to the area from the water table to the capillary rise of the water. Different mathematical models, such as the Brooks-Corey or van Genuchten model, exist to describe the permittivity gradient in this zone, which is nonlinear. Dagenbach focused on the effect of the reflected signal for stationary, and non-stationary scenarios (draining and pumping). One of the conclusions was the significant change in the reflected signal for non-stationary cases compared to the stationary ones. Dagenbach focussed on common offset survey modes. In this setup, an analysis of the DGW is not possible. As stated before, we will focus on a WARR survey to include the spatial variability of the DGW in the analysis.

Gulevich et al. (2022) concluded that the water depth estimation in a freshwater body is based on the distribution of electric conductivity and permittivity in the near-bottom layer. Naturally, this layer is inhomogeneous. Numerical modeling of a vertical permittivity gradient from 81 to 9 below a homogeneous water body reveals that the presence of additional reflective boundaries in the radargram can suggest variations in the electrical properties. The multiple boundaries in the gradient can hide the reflection from the bottom of the water body, making the interpretation of data more challenging. The effect of the gradient on the GPR signal was only evaluated for a zero-offset A-scan. Prokopovich et al. (2018) implemented a semi-analytical expression using the Wentzel-Kramers-Brillouin approximation to describe EM wave propagation in smooth permittivity gradients in 2D lossless media. They validated the results of their expression with numerical solutions for A-scans for a WARR setup, where the soil consists of two homogeneous layers that are connected by a permittivity transition zone to simulate a water pond with a silty bottom, similar to Gulevich et al. (2022).

Sperl (1999) conducted numerical studies for a WARR survey where the subsurface contains linearly increasing permittivity gradients. His empirical formula to determine the sensing depth of the DGW has been discussed in section 2.2.5. His findings will be further addressed in chapter 5.

To summarize, in this study we want to focus on areas that have not been extensively examined before, this includes

1. Assessing increasing and decreasing surface permittivity gradients that are measured with a WARR survey with a numerical forward model.
2. Understanding and potentially finding typical wavefield characteristics in gradient structures.
3. Analyzing both the DAW, DGW, and other events coming from the ground.

3

Numerical modeling of boreholes and permittivity gradients

Forward simulations are performed with *gprMax* (Warren, 2021): a free and open source software package for numerical modeling of EM wave propagation, including interaction with structures. Its first version was released in 1996 and was primarily designed for modeling GPR applications.

3.1. Software: gprMax

GprMax uses a finite difference time-domain (FDTD) scheme with second-order accurate derivatives in space and time to solve Maxwell's equations in 3D. The creators of gprMax use Yee's algorithm for FDTD, where the so-called Yee cells cubically discretize the three-dimensional domain (Yee, 1966). The E and H components are staggered along the interfaces of the cells, resulting in each E-field component being surrounded by four circulating H-field components and vice versa by half the cell size. Electric field components are tangential to the cell and magnetic field components are normal to it (see Fig. 3.1). In the following, we will only discuss the computation of the E_x and H_x components for both the continuous and discrete schemes, as the calculation of the other components is analogous. A comprehensive description can be found in Taflove et al., 2005.

From Eqs. (2.1a) to (2.1d), a system of coupled scalar equations can be formed:.

$$\frac{\partial H_x}{\partial t} = \frac{1}{\mu}\left[\frac{\partial E_y}{\partial z} - \frac{\partial E_z}{\partial y} - \left(M_{ex_x} + \sigma^* H_x\right)\right], \tag{3.1}$$

$$\frac{\partial E_x}{\partial t} = \frac{1}{\varepsilon}\left[\frac{\partial H_z}{\partial y} - \frac{\partial H_y}{\partial z} - \left(J_{ex_x} + \sigma E_x\right)\right]. \tag{3.2}$$

The notation for the discretization of time and space is:

$$(x, y, z, t) = (i\Delta x, j\Delta y, k\Delta z, n\Delta t). \tag{3.3}$$

This leads to the notation of an arbitrary continuous function u to.

$$u(x, y, z, t) = u|^n_{i,j,k}. \tag{3.4}$$

By applying a leapfrog time-stepping method, the E-field components are updated using the previously calculated H-field components, followed by the H-field components being updated with the previously calculated E-field components. This cycle is repeated for each time step Δt where E and H are sepa-

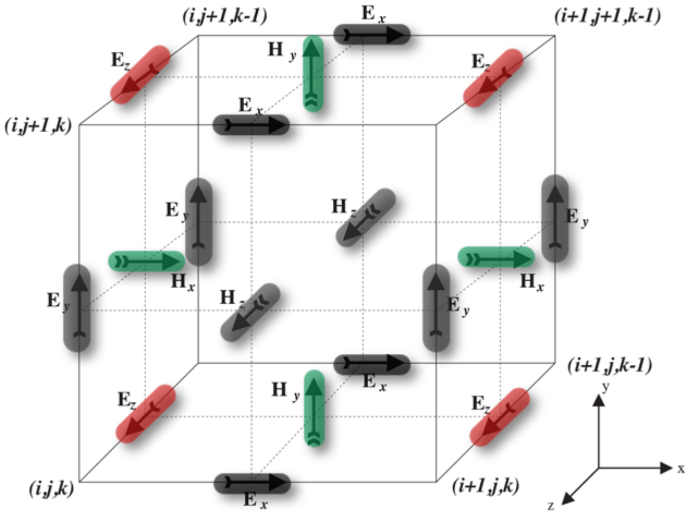

Figure 3.1: Single FDTD Yee cell showing electric (red), magnetic (green) field components for 2D TM z-direction mode after Warren and Giannopoulos (2022). The width of the z-direction is set to the width of one cell size. Thus, the simulations will be carried out in the TM mode. This means that only the E_z, H_x, and H_y components (marked red and green) will be present, while the other components (marked gray) will be set to zero.

rated by $\Delta t/2$ (Warren, 2009). The finite difference expressions of second-order accuracy are:

$$
\begin{aligned}
E_x\Big|_{i,j+1/2,k+1/2}^{n+1/2} &= \left(\frac{1-\dfrac{\sigma_{i,j+1/2,k+1/2}\Delta t}{2\varepsilon_{i,j+1/2,k+1/2}}}{1+\dfrac{\sigma_{i,j+1/2,k+1/2}\Delta t}{2\varepsilon_{i,j+1/2,k+1/2}}}\right) E_x\Big|_{i,j+1/2,k+1/2}^{n-1/2} \\
&+ \left(\frac{\dfrac{\Delta t}{\varepsilon_{i,j+1/2,k+1/2}}}{1+\dfrac{\sigma_{i,j+1/2,k+1/2}\Delta t}{2\varepsilon_{i,j+1/2,k+1/2}}}\right) \times \left(\begin{matrix} \dfrac{H_z\big|_{i,j+1,k+1/2}^{n} - H_z\big|_{i,j,k+1/2}^{n}}{\Delta y} \\ -\dfrac{H_y\big|_{i,j+1/2,k+1}^{n} - H_y\big|_{i,j+1/2,k}^{n}}{\Delta z} \\ -J_{ex_x}\Big|_{i,j+1/2,k+1/2}^{n} \end{matrix}\right),
\end{aligned}
\tag{3.5}
$$

$$
\begin{aligned}
H_x\Big|_{i-1/2,j+1,k+1}^{n+1} &= \left(\frac{1-\dfrac{\sigma^*_{i-1/2,j+1,k+1}\Delta t}{2\mu_{i-1/2,j+1,k+1}}}{1+\dfrac{\sigma^*_{i-1/2,j+1,k+1}\Delta t}{2\mu_{i-1/2,j+1,k+1}}}\right) H_x\Big|_{i-1/2,j+1,k+1}^{n} \\
&+ \left(\frac{\dfrac{\Delta t}{\mu_{i-1/2,j+1,k+1}}}{1+\dfrac{\sigma^*_{i-1/2,j+1,k+1}\Delta t}{2\mu_{i-1/2,j+1,k+1}}}\right) \times \left(\begin{matrix} \dfrac{E_y\big|_{i-1/2,j+1,k+3/2}^{n+1/2} - E_y\big|_{i-1/2,j+1,k+1/2}^{n+1/2}}{\Delta z} \\ -\dfrac{E_z\big|_{i-1/2,j+3/2,k+1}^{n+1/2} - E_z\big|_{i-1/2,j+1/2,k+1}^{n+1/2}}{\Delta y} \\ -M_{ex_x}\Big|_{i-1/2,j+1,k+1}^{n+1/2} \end{matrix}\right).
\end{aligned}
\tag{3.6}
$$

Simulations can be conducted in a 2D domain by setting one extent of the domain equal to the corresponding Yee cell size in that direction. In this case, the E and H components that are parallel to the 2D plane remain invariant and are set to zero (Warren & Giannopoulos, 2022).

3.2. Stability criteria

Numerical Dispersion Due to the nature of the FDTD method as an explicit time-stepping technique, it is only conditionally stable: its time step is constrained by the Courant Friedrichs Lewy (CFL) stability condition, which relates the spatial discretization to the time step. For a three-dimensional medium, it is defined as (Taflove et al., 2005):

$$\Delta t \leq \frac{1}{c_0\sqrt{\frac{1}{\Delta x^2}+\frac{1}{\Delta y^2}+\frac{1}{\Delta z^2}}}. \tag{3.7}$$

This criterion prevents numerical dispersion, which occurs when different frequencies of the wavefields propagate slower or faster compared to the correct speed of wave propagation in the medium. This leads to numerical artifacts in the solution (Robertsson & Blanch, 2020). It occurs when the wavefield is discretized with an insufficient number of grid points per wavelength (Igel, 2017). To keep numerical dispersive phenomena small, the discretization step should be at least ten times smaller than the smallest wavelength of the propagating electromagnetic fields, as a rule of thumb (Warren & Giannopoulos, 2022).

Perfectly matched layer (PML) The GPR forward problem is classified as an initial value open boundary problem, meaning that to obtain a solution, one has to define an initial condition (that is, the excitation of the GPR transmitting antenna). Fields propagate through space to reach a zero value at infinity, since there is usually no particular boundary that limits the geometry of the problem (Giannopoulos, 2005). Thus, an important factor of gprMax is the implementation of absorbing boundary conditions applied at the edges of the computational domain to simulate an infinite boundary and eliminate undesired reflections from the edge of the domain. For this, perfectly matched layer (PML) is a very efficient type of absorbing boundary conditions. The waves are gradually attenuated towards the boundary in a transition zone, which prevents causing additional reflections compared to a rapid change in attenuation (Robertsson & Blanch, 2020). In the continuous framework, a PML model is designed to ensure that outgoing waves are perfectly transmitted at the interface between the physical domain and the absorbing layers, regardless of their non-zero angles of incidence and non-zero angular frequencies. Moreover, once inside the PML, these waves are damped exponentially along the direction perpendicular to the interface. However, in a discretized framework, such as in FDTD, the property of perfectly matching (reflectionless) is not fulfilled due to the numerical dispersion inherent to any discretization scheme. The finite thickness of the absorbing layer might not completely dampen outgoing waves, causing them to reflect at the exterior boundary and propagate back into the physical model domain. Although being damped by an exponential factor twice, they can still cause spurious waves with a non-zero amplitude (Pled & Desceliers, 2022). GprMax uses a special type of PML corresponding to the complex frequency-shifted approach of Giannopoulos (2012).

The briefly mentioned implementations allow gprMax to be a simple, fully explicit, general, and robust technique. The main weakness is related to the discretization of the entire modeling domain, which may require a considerable amount of computational resources (Warren, 2021).

3.3. Model of a resistor loaded finite length antenna (RLFLA)

GPR surveys conducted since the early 1970s used some form of resistively loaded dipole antenna to obtain a short pulse required for high-depth resolution (Arcone, 1995).

According to Lampe (2003), the perfect GPR antenna design would include features such as (1) consistent antenna characteristics under varying acquisition conditions, (2) emission of a stable broadband pulse, and (3) an efficient transmitter. In the case of the latter, the antenna's resistance should be kept to a minimum. However, undamped antennas tend to produce multiple reflections from both ends, which can result in a ”ringy” signal. The multiple reflections of current are undesirable in a GPR system as they might overshadow the returns of a target. This issue can be mitigated by adding resistors to the antenna, which can reduce or even eliminate internal reflections. Wu and King (1965) introduced the concept of putting a tapered resistive profile on a cylindrical antenna that increases towards the antenna ends.

One advantage of the Wu and King profile over other resistive profiles is that the signal maintains a certain bandwidth (Martel, 2002), which is an important factor for condition (2). When using Wu and King resistive loading, the effective electrical length of the antenna is decreased, resulting in radiative properties that resemble those of an infinitesimal electric dipole, regardless of the frequency (Tronicke & Holliger, 2004). Nevertheless, when choosing to resistively load the antenna arms, one must be aware of the trade-off between ringing suppression and antenna radiation efficiency in condition (3). Antenna manufacturers often find a compromise in the spectrum of Wu and King loading and an unloaded antenna.

Mozaffari et al. (2022) modeled a resistor loaded finite-length antenna (RLFLA) in 3D with gprMax that is based on a 200 MHz PulseEKKO antenna. We built the same antenna using the parameters given in his work. A cross-section of the antenna model is given in Fig. 3.2. As indicated, each resistively loaded arm of the dipole has a length of 24 cm. A cylindrical PEC is used as a transmission wire that consists of ten 1 cm long resistor segments with $\sigma = 0.1\,\mathrm{mS\,m^{-1}}$ at each side. The feeding gap, in which a voltage source is placed, is mesh size-dependent and should have the length of one Yee cell. The voltage source is a hard source[1] having an internal resistance of zero. The transmission wire is surrounded by an insulating material having $\epsilon_r = 4$ and $\sigma = 1 \times 10^{-7}\,\mathrm{mS\,m^{-1}}$. The total length of the antenna is 1.2 m, the radius of the insulating material is 3 cm, and of the wire is 2 cm.

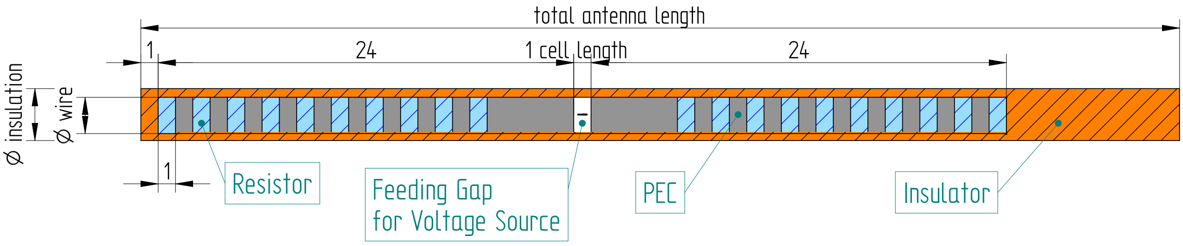

Figure 3.2: Cross-section of the RLFLA model in gprMax. All units are given in cm.

3.4. Borehole model

To investigate realistic radiated wavefields in crosshole tomography, a 3D domain containing two vertical boreholes is created in gprMax as shown in Fig. 3.3. The boreholes have the same radius r_b and are horizontally separated by Δx. Also, their borehole filling shares the same EM properties $\epsilon_{r,b}$ and σ_b. The transmitting (TX) and receiving (RX) RLFLA model is placed in each borehole. The feeding gaps of the antennas can have a vertical offset depending on the value of the straight ray angle α, as commonly found in multi-offset gathers (MOG) in crosshole GPR. The boreholes are surrounded by a homogeneous medium having $\epsilon_{r,m}$ and σ_m.

---

[1] Detailed explanations of soft and hard sources are given in the Appendix A.1.

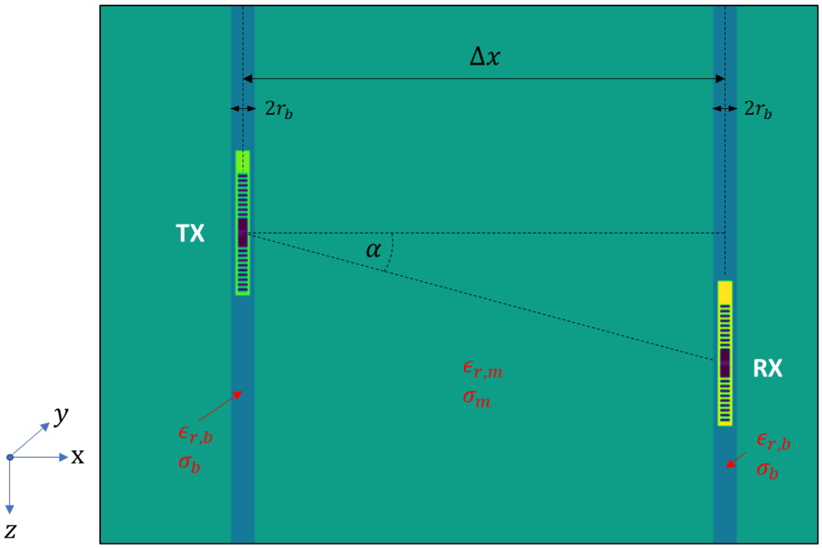

Figure 3.3: Cross-section of the borehole model in gprMax (TM mode).

3.5. Gradient model

A 3D model is built in gprMax for surface GPR to investigate the effects of permittivity gradients starting at the air-soil interface on the received GPR signal. The model is shown in Fig. 3.4. A WARR survey mode is chosen in a broadside configuration (TE mode), where S is the y-polarized source and R is the receiver. They are not directly placed on the air-soil interface, but five cells above to better simulate real conditions where direct ground coupling is not possible. All materials in the model are assumed to be horizontally layered. The relative magnetic permeability μ_r is 1 and the magnetic loss σ^* is 0. The spatial discretization Δs is 1 cm in all directions of the model to avoid numerical dispersion and to provide a sufficiently smooth gradient. The degrees of freedom are denoted with variables in Fig. 3.4. The initial offset is denoted with dx_1, the receiver spacing with $dx_2 = dx_3 = \ldots = dx_n$, and the largest offset with Δx. The gradient layer has an initial permittivity of $\epsilon_{r,1}$. For each cell in the z-direction within the gradient layer, the permittivity value changes $\Delta\epsilon_r = \frac{\epsilon_{r,k}-\epsilon_{r,1}}{h}$, where $k = h/\Delta s$ is the total number of cells in the vertical direction of the gradient layer. Depending on the initial value $\epsilon_{r,1}$ and the end value $\epsilon_{r,k}$, $\Delta\epsilon_r$ can be positive or negative, leading to an increasing or decreasing permittivity gradient. A homogeneous layer follows after the gradient layer having a permittivity value of $\epsilon_{r,k}$. The model can run in 2D by setting the extent of the y-direction to the size of a single cell, as explained in section 3.1.

In this work, four different set-ups are investigated.

1. Homogeneous halfspace,
2. Two-layer case,
3. Decreasing gradients,
4. Increasing gradients.

The homogeneous halfspace has a uniform permittivity in the soil of $\epsilon_{r,1} = \epsilon_{r,k}$. In the two-layer case, the gradient layer has a uniform permittivity of $\epsilon_{r,1} = \epsilon_{r,2} = \ldots = \epsilon_{r,k-1}$ and the homogeneous layer has a uniform permittivity of $\epsilon_{r,k}$. For a decreasing gradient, $\epsilon_{r,1} > \epsilon_{r,k}$, and for an increasing gradient

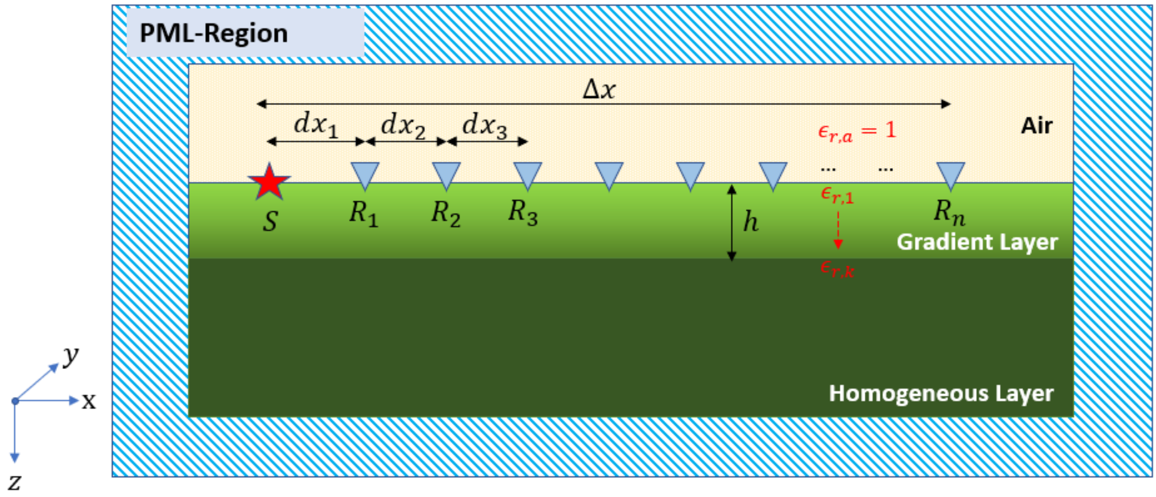

Figure 3.4: Schematic cross-section of the gradient model. It is invariant in the y-direction.

$\epsilon_{r,1} < \epsilon_{r,k}$. According to Eq. (2.9), the relationship between EM velocity and ϵ_r is $v \propto \frac{1}{\sqrt{\epsilon_r}}$. For each case, an exemplary permittivity and velocity distribution of the model is given in Fig. 3.5.

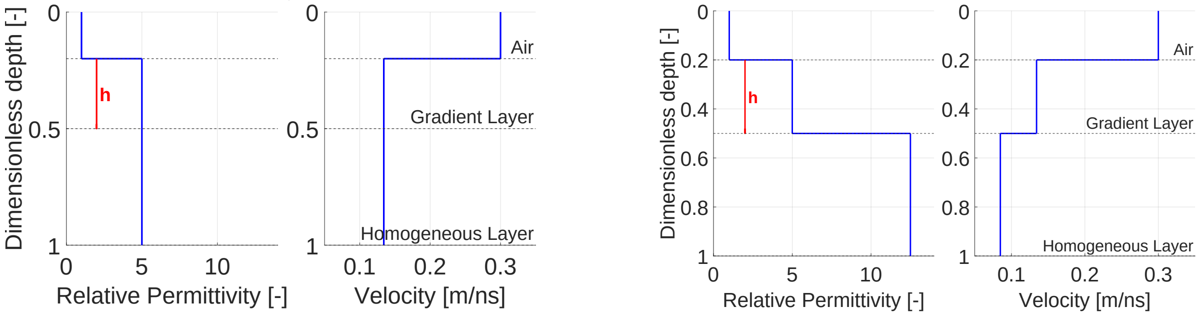
(a) Homogeneous case ($\epsilon_{r,1} = 5$).

(b) Two-layer case ($\epsilon_{r,1} = 5$ and $\epsilon_{r,k} = 12.5$).

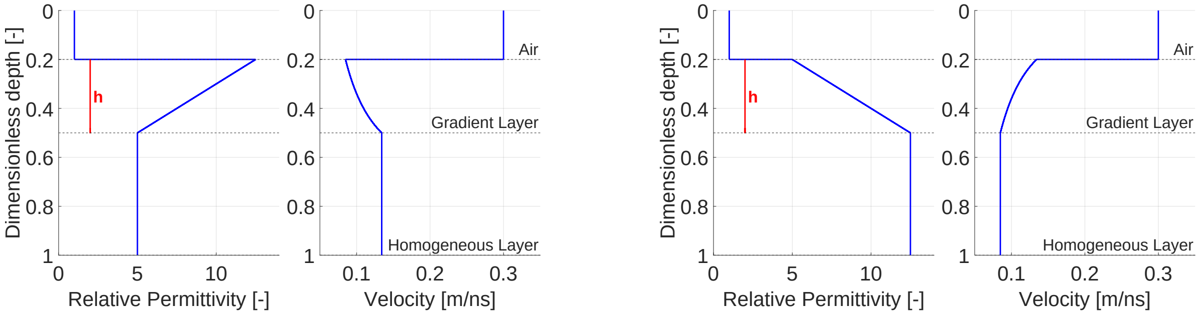
(c) Decreasing gradient ($\epsilon_{r,1} = 12.5$ and $\epsilon_{r,k} = 5$).

(d) Increasing gradient ($\epsilon_{r,1} = 5$ and $\epsilon_{r,k} = 12.5$).

Figure 3.5: Schematic permittivity and velocity distribution of the gradient model shown in Fig. 3.4 with a dimensionless depth. The height h of the gradient layer is denoted with a red line.

Fig. 3.6 shows a flowchart for the steps involved for creating and processing the model in Fig. 3.4. Initially, a Python code is utilized to generate an input (.in) file, incorporating the free parameters displayed in the green box. The author is responsible for developing the framework to generate the input file. Next, the generated input is passed to gprMax where the actual EM wave propagation is simulated. This process yields output (.out) and geometry (.vti) files, which are then separately processed in MATLAB and Python, respectively.

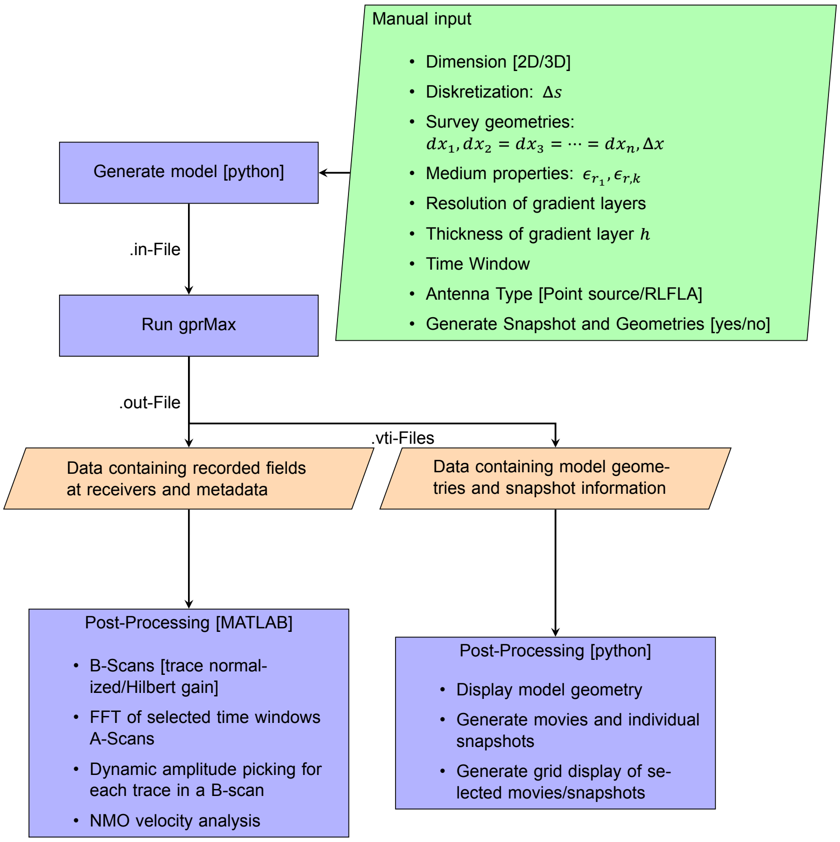
Manual input
Dimension [2D/3D]
Diskretization: Δs
Survey geometries: $dx_1, dx_2 = dx_3 = \cdots = dx_n, \Delta x$
Medium properties: $\epsilon_{r_1}, \epsilon_{r,k}$
Resolution of gradient layers
Thickness of gradient layer h
Time Window
Antenna Type [Point source/RLFLA]
Generate Snapshot and Geometries [yes/no]
Generate model [python]
.in-File
Run gprMax
.out-File
.vti-Files
Data containing recorded fields at receivers and metadata
Data containing model geometries and snapshot information
Post-Processing [MATLAB]
B-Scans [trace normalized/Hilbert gain]
FFT of selected time windows A-Scans
Dynamic amplitude picking for each trace in a B-scan
NMO velocity analysis
Post-Processing [python]
Display model geometry
Generate movies and individual snapshots
Generate grid display of selected movies/snapshots

Figure 3.6: Flowchart for creating and processing the model shown in Fig. 3.4.

3.6. Experimental determination of an appropriate parametrization of the PML region

In view of correct modeling, there exist rules of thumb regarding the parameterization of the PML region (Warren & Giannopoulos, 2022). It is recommended to keep sources and receivers at least 15 cell lengths away from the start of the PML region. Also, the thickness of the absorbing layer should be comparable to half of the largest wavelength in the simulation.

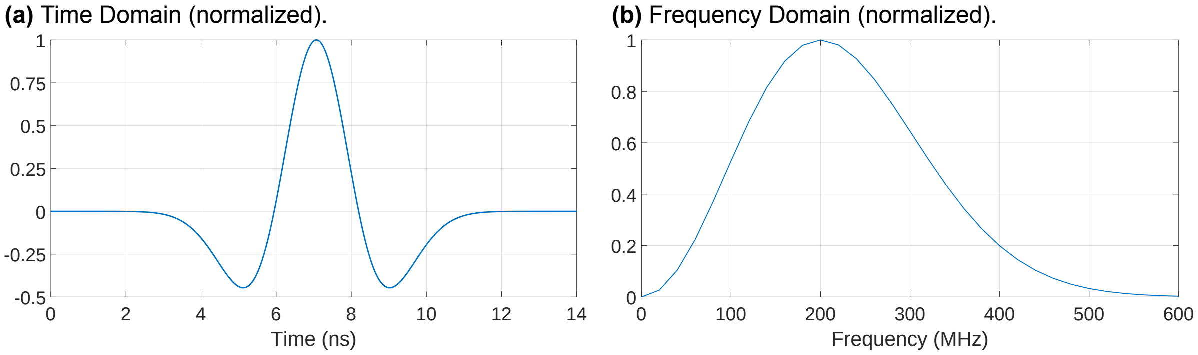
(a) Time Domain (normalized).

(b) Frequency Domain (normalized).

Figure 3.7: Ricker wavelet with 200 MHz center frequency.

In the following, the effect of the PML region thickness for a homogeneous halfspace with $\epsilon_{r,1} = 5$ is investigated in a 2D domain with a 200 MHz Hertzian dipole as the source. The dipole is excited with the Ricker wavelet shown in Fig. 3.7, the negative second derivative of a Gaussian pulse. Eventually, we want to find an appropriate thickness for the PML region for the model.

The PML region surrounding the 2D domain is progressively increased for $n_{pml} = [20, 50, 80, 100, 150, 200, 300]$ cells. For 20 cells (Fig. 3.8a), spurious reflections can be seen in the trace-normalized B-scan, especially towards larger offsets (red circle). This thickness is apparently too small and allows outgoing waves to reach the exterior of the PML domain and get reflected into the physical domain. If not aware of the importance of the PML region, one could easily falsely interpret the spurious reflections, especially for models with more complex setups than the homogeneous case. For increasing thicknesses, the spurious reflections are no longer visible on the B-Scan anymore, as shown in Figs. 3.8b and 3.8c for 50 and 100 PML cells, respectively. To further investigate the presence of artificial reflections, difference plots between adjacent thicknesses n^{i}_{pml} and n^{i+1}_{pml} are compared. Three are shown in Figs. 3.8d to 3.8f. The difference in 80 and 50 PML cells clearly shows the presence of artificial, non-physical reflections on the lower left side of the domain, which are not acceptable. Difference plots for increasing PML thicknesses (Figs. 3.8e and 3.8f) still show discrepancies. As previously mentioned, the finite thickness of the PML regions does not allow to 'perfectly' match outgoing waves, and a certain impedance contrast will always be present. Waves that are reflected from the PML region back into the physical domain will have a phase and amplitude difference depending on the thickness of the PML region. This will lead to discontinuously distributed energy in the difference plots. However, these phenomena are still present for 300 PML cells and are not significant. When inspecting the individual traces, an acceptable overlap is observable. To find a good compromise between computation time and accuracy, 100 PMLs are chosen for the simulations.

(a) 20 PML layers. **(b)** 50 PML layers. **(c)** 100 PML layers.

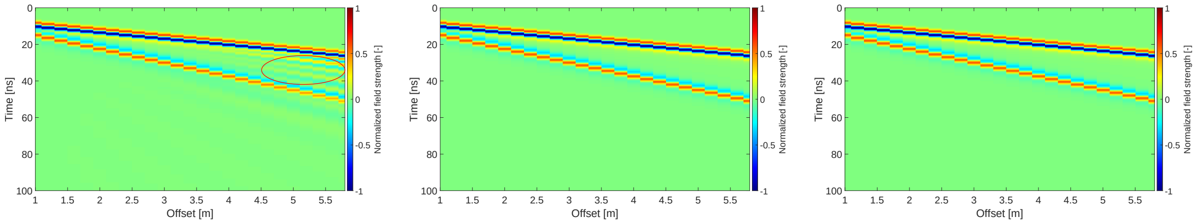

(d) Difference plot of B-Scan with 80 and 50 PML cells. **(e)** Difference plot of B-Scan with 100 and 80 PML cells. **(f)** Difference plot of B-Scan with 150 and 100 PML cells.

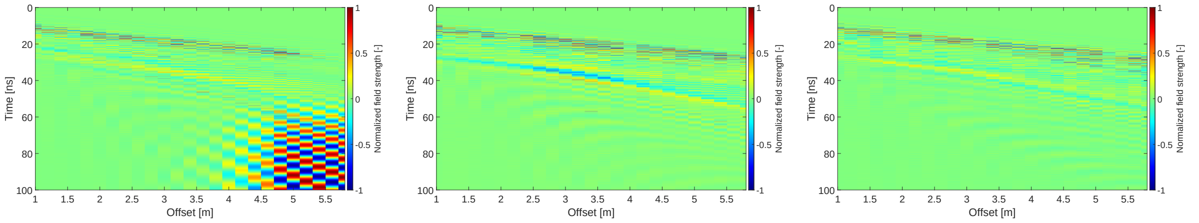

Figure 3.8: B-Scans for a homogeneous halfspace in 2D for $\epsilon_{r,1} = 5$ and a Hertzian dipole excited with a 200 MHz Ricker wavelet and a mesh size of 1 cm. Each trace in the B-scan is normalized with respect to its absolute maximum. In (a), the artificial reflections caused by the PML region can be seen in the normalized B-Scan (red circle).

4

Influence of boreholes on crosshole GPR

Crosshole GPR has become increasingly popular for high-resolution imaging of the shallow subsurface over the past decade (Irving & Knight, 2006). It has demonstrated its ability to accurately provide shallow subsurface electrical characteristics, which can be transformed into hydrological parameters using petrophysical relationships. This technique has proven to be a strong tool for mapping and evaluating aquifers, mainly due to its high resolution and sensitivity to factors such as porosity and SWC (Klotzsche, 2013, p.3).

Several survey modes exist, such as the zero offset profiling (ZOP) or multi-offset gather (MOG) mode. The latter is the basis for tomographic inversion. Whereas the transmitter and receiver are located at the same depth for ZOP, the transmitter remains fixed in MOG while the receiver is systematically lowered at regular intervals along one borehole, as indicated in Fig. 2.2. This approach involves multiple positions of the transmitter, ensuring a large sampling of the medium between the boreholes using a multitude of rays and angles. The denser the ray coverage within a region, the higher the resolution (Klotzsche, 2013).

For many years, it has been common practice to exclude high angle ray paths due to an increase in the apparent velocity. The apparent velocity is calculated by dividing the direct distance between the transmitter and receiver with the first arrival time (Mozaffari et al., 2022). Initially, this artifact was attributed to antenna distortion due to different velocities in the antenna and the surrounding medium. Distortion occurs when waveforms originating from different parts of the antenna do not reach the reflection field point in phase. A closed-formed solution for a loaded dipole in air exists explaining this phenomenon (Arcone, 1995). Additionally, if the velocity of the antenna insulation is higher than the surrounding medium, then the possibility would exist at high transmitter-receiver angles for the first-arriving energy to travel between the tips of the antennas (Irving & Knight, 2005).

Mozaffari et al. (2022) showed with numerical modeling of a RLFLA that this artifact is actually attributed to the refractions occurring at the interfaces between the borehole fluid and the subsurface. By determining the refractions at the interfaces with numerical modeling in gprMax, the increase in apparent velocity for high angle data could be accurately explained.

In general, the presence of both water and air-filled wells results in changes in radiated wavefronts, waveforms, and resonant frequencies compared to a dipole antenna placed in homogeneous media. The effects of boreholes, whether filled with water or air, should not be ignored in the design of antennas (S. Liu & Sato, 2005).

Tronicke and Holliger (2004) claim that there are two primary distinctions in the case of water-filled boreholes: a shift towards lower frequencies in the spectral range and a less concentrated radiation

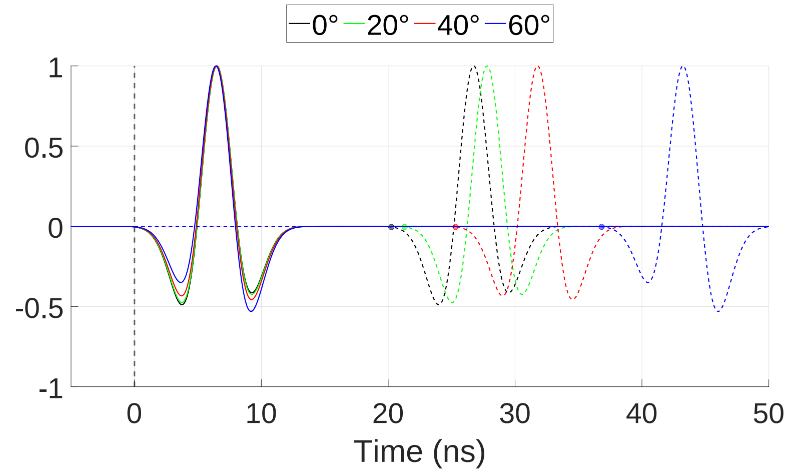

Figure 4.1: Demonstration of algorithm for first break picking for a 100 MHz Hertzian dipole separated 5 m and different straight ray angles. The dashed lines are the original traces. The solid lines represent the aligned traces on their first break at $t = 0$ ns, which is at 1% of their first local minimum amplitude, denoted with the colored dots.

pattern. The frequency shift is most likely attributed to waveguide effects occurring within the water-filled borehole. Designing an antenna that performs well in both water and air-filled boreholes requires a trade-off regarding resonant frequencies (S. Liu & Sato, 2005).

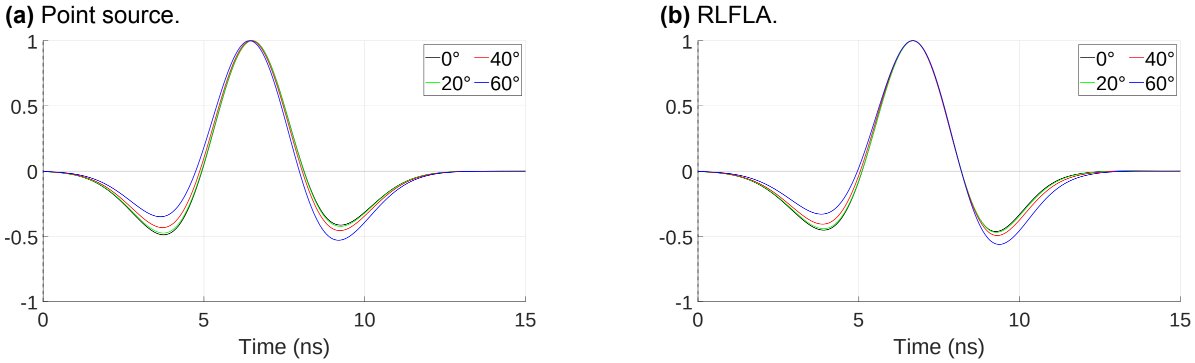
(a) Point source.

(b) RLFLA.

Figure 4.2: Simulations in free space for $\Delta x = 5$ m.

The objective is to assess the behavior of the received signal in borehole environments and different vertical antenna offsets to support ongoing projects focused on inversion of crosshole GPR data. Increasing computing power allows the 3D forward calculation for each iteration in the inversion process to include a finite-length antenna and boreholes, which is an innovation in this field. We will try to evaluate the advantages of including a RLFLA in the forward model instead of a point source, which is common practice. The point source is a Hertzian dipole excited with a 100 MHz wavelet with the shape of the first derivative of a Gaussian pulse. The RLFLA is excited with a 92 MHz Gaussian pulse. The former is classified as a soft source and the latter as a hard source (see Appendix A.1). By knowing their relationship according to Eq. (A.4), the resulting emitted electrical fields have a similar shape to a Ricker wavelet. As the sources are polarized in the z-direction, the E_z field is measured and evaluated.

To compensate for different arrival times due to different straight ray angles α, an algorithm has been developed that picks the time when the amplitude exceeds 1% of the first local minimum of each trace. The algorithm is demonstrated for simulations of the point source in free space for different straight ray

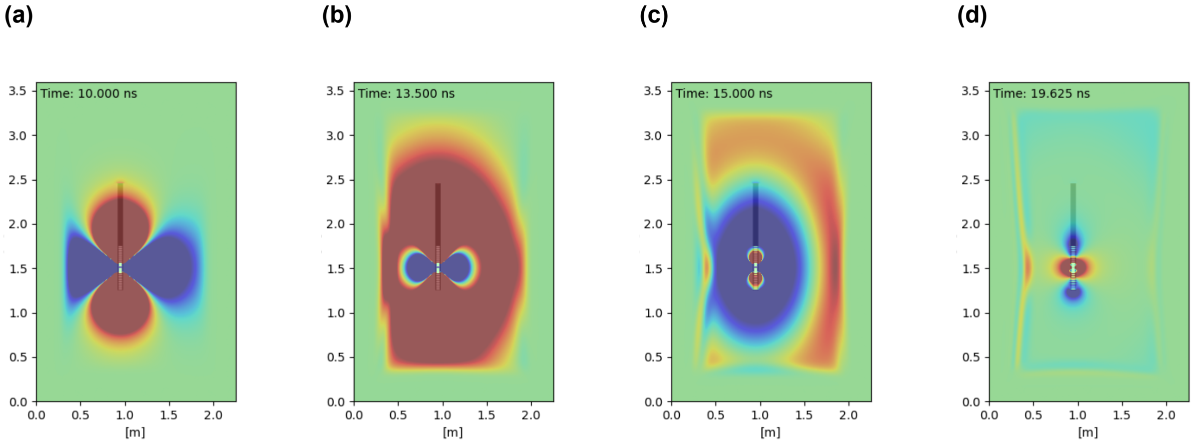

Figure 4.3: Snapshots for a RLFLA placed in free space.

angles α in Fig. 4.1. Note that each trace is normalized with respect to its absolute maximum to provide a better comparison.

The aligned traces in Fig. 4.1 are shown in detail in Fig. 4.2a together for the results if a RLFLA is used instead of a point source in Fig. 4.2b. In free space, the tendency of the waveform shape depending on the straight path angle α is quite similar for both the point source and the RLFLA. The position of the main lobe remains nearly constant for all cases.

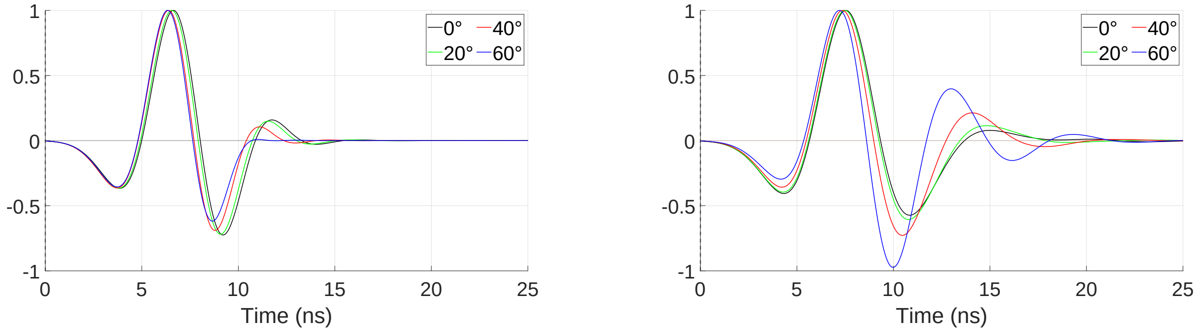

(a) Point source, $r_b = 2$ cm.

(b) RLFLA, $r_b = 5$ cm.

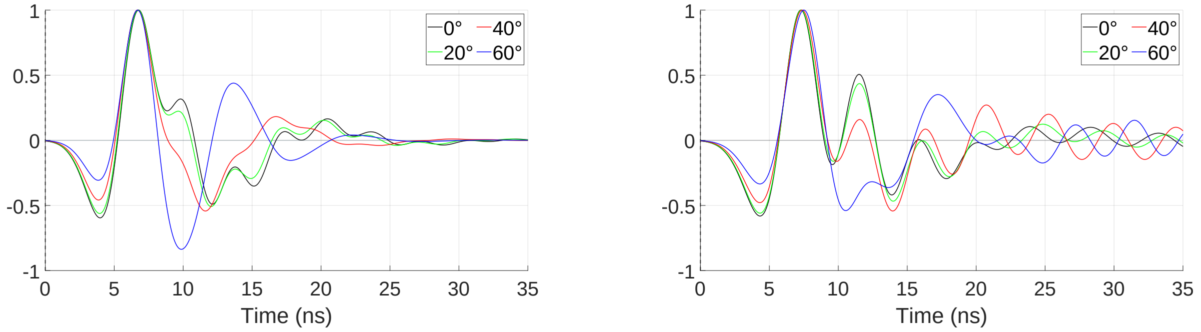

(c) Point source, $r_b = 7$ cm.

(d) RLFLA, $r_b = 10$ cm.

Figure 4.4: Simulations in water-filled boreholes for $\Delta x = 5$ m.

An increasing value of α appears to reduce the magnitude of the first side lobe and increase the magnitude of the second side lobe. Fig. 4.3 shows snapshots of the RLFLA placed in free space. The two received negative side lobes in Fig. 4.2 can be seen as the blue wavefronts at 10 ns in Fig. 4.3a and at 15 ns in Fig. 4.3c. At 13.5 ns, the positive main lobe is visible as the red wavefront at 13.5 ns in Fig. 4.3b. In Fig. 4.3d, the RLFLA is not radiating anymore.

Next, we use the borehole model shown in Fig. 3.3 to simulate water-filled boreholes placed in saturated gravel. We use $\epsilon_{r,b} = 80$, $\epsilon_{r,m} = 12.5$, and $\sigma_b = \sigma_m = 0.1$ mS m^{-1}. As the radius of the RLFLA is 3 cm and the point source has no dimension, we use a discrepancy of 3 cm for the respective radius r_b such that the waves travel through a similar layer of water within the borehole. In this way, we are consistent and can compare the results.

In Fig. 4.4, the aligned traces for different radii r_b are compared, where in Figs. 4.4a and 4.4b an additional positive lobe at the end of the received wavelet can be seen. One explanation for this phenomenon could be interference between the first emitted signal traveling from the transmitter towards the receiver and the first reflection at the opposite water-gravel interface also traveling towards the receiver. Note that no borehole casing is included in the model shown in Fig. 3.3. The additional positive cycle at the end of the received signal might be the main lobe of the reflected signal that is traveling toward the receiver. At 22.8 ns in Fig. 4.5 an additional positive wavefront can be seen compared to the radiation in free space in Fig. 4.3d at 19.625 ns. The interference effects seem to be more prominent for the finite-length antenna.

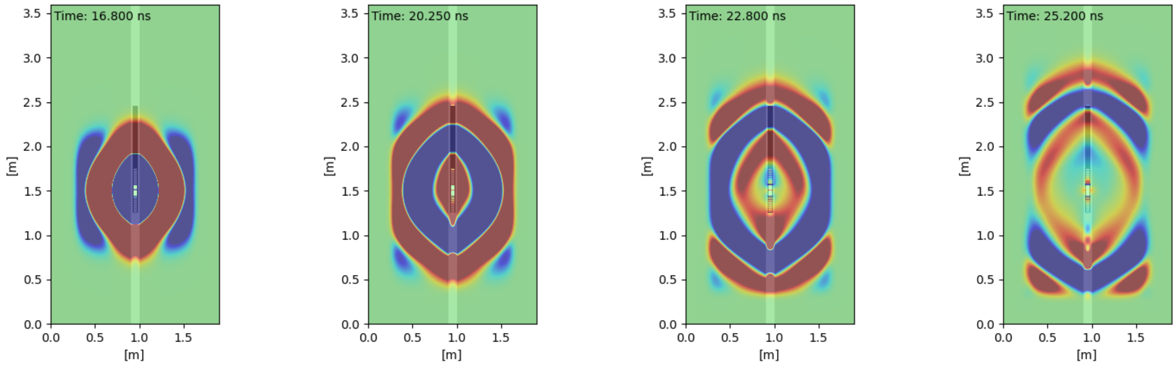

Figure 4.5: Snapshots for a RLFLA placed in a water-filled borehole with $r_b = 5$ cm.

Figs. 4.4c and 4.4d show the results for even larger borehole radii r_b. For both the finite-length antenna and point sources, long-lasting oscillations are present at the end of the signal. In contrast to lower r_b, these have multiple peaks and seem to be more prominent for the RLFLA. Tronicke and Holliger (2004) reported that a water-filled borehole can act as a dispersive waveguide similar to a fiber optic cable. This effect is visible in the snapshots in Fig. 4.6, where elongated wave trains are traveling along the cylindrical borehole. As the borehole in Fig. 4.4c has a 3 cm lower r_b than Fig. 4.4d, these waveguide effects are not expected to be as strong due to higher cut-off frequencies[1].

Overall, similar wavefields are obtained for both the point dipole and the finite-length antenna in free space. In contrast to an unloaded antenna, where polarity shifts for increasing straight ray angles were reported (S. Liu & Sato, 2005), the radiative properties of the RLFLA are quite similar to those of an infinitesimal electric dipole. This is also true for small borehole diameters (Figs. 4.4a and 4.4b). Nevertheless, the measured wavefield seems to be very sensitive to the radius of the water-filled borehole

---

[1] A more detailed discussion on waveguides is given in section 5.1.

r_b, as has been shown in Figs. 4.4c and 4.4d. The resulting wavefield consisting of multiple internal reflections becomes very complex and largely depends on the size of the water column, which acts as a cylindrical waveguide. These effects are both present for point sources and finite-length antennas. Nevertheless, due to the complex wavefield interactions, where the antenna body is an additional reflector, and sensitivity to the water column, it might be worth including a finite-length antenna in the forward model. Note that the point source is a soft source, meaning that is does not interact with (and reflect) any incident waves.

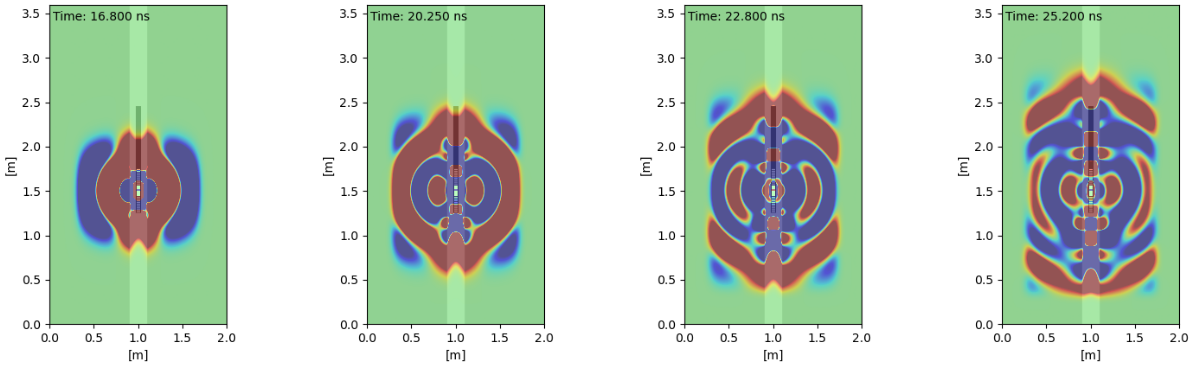

Figure 4.6: Snapshots for a RLFLA placed in a water-filled borehole with $r_b = 10\,\mathrm{cm}$.

5

Influence of permittivity gradients on surface GPR

As indicated in the introduction, inhomogeneities naturally occur in real media, including smooth permittivity distributions. The interaction of GPR signals with this kind of inhomogeneity can be very complex. However, the research in this area is limited, particularly in understanding and examining these phenomena within common survey modes like WARR or CMP, as discussed in section 2.3.

In section 5.1, we analyze the four different setups of the gradient model in section 3.5 in a 2D domain. We begin by assessing the homogeneous halfspace, followed by the two-layer case, and finally, the scenarios involving decreasing and increasing gradients. Although only 3D media occur in nature, we justify the investigation of 2D media for two reasons. Firstly, our model is invariant in the horizontal direction, and secondly to reduce computation time and enable more efficient analysis.

We gradually increase the complexity of the analysis of the simulations. First, we visually evaluate prominent differences of each B-scan in section 5.1.1. Next, we perform an amplitude analysis (5.1.2), a frequency analysis (5.1.3), and apply a gain on the traces (5.1.4). The new features we discovered by this analysis are further investigated in section 5.2. Finally, section 5.3 and 5.4 provide a validation of highlighted findings in 3D and a summary.

5.1. Simulations in 2D

All simulations are performed for lossless media with a Hertzian dipole excited with the 200 MHz Ricker wavelet shown in Fig. 3.7. The initial offset is $dx_1 = 0.5$ m, as it is common practice in real-site investigations. The maximum offset is $\Delta x = 10.1$ m and the receiver spacing is uniform $dx_2 = dx_3 = \dots = dx_{49} = 0.2$ m.

In the following, two new terminologies are introduced:

Strong contrast stands for a permittivity contrast of either 5 to 12.5 or 12.5 or 5. These values have been used by Mozaffari et al. (2022) to simulate unstaturated ($\epsilon_r = 5$) and saturated ($\epsilon_r = 12.5$) gravel.

Weak contrast represents a permittivity contrast of 5 to 6 or 6 to 5, which could occur in different compacted sand sediment layers.

5.1.1. First analysis of trace-normalized B-scans

Homogeneous halfspace Two B-scans of homogeneous halfspaces with permittivities of 5 and 20 are shown in Fig. 5.1. As expected, only the direct air wave (DAW) and direct ground wave (DGW) are visible (see explanations in section 2.2.5). The inspection of the snapshots in Fig. 5.2 confirms that only the two direct waves can be recorded by receivers that are placed close to the air-soil interface. When the permittivity increases, the DGW decreases in velocity, which is visible on its steeper slope in the B-scan.

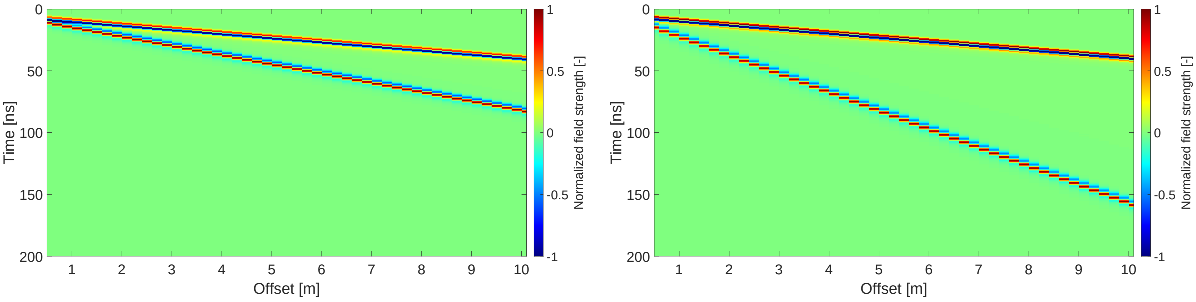

(a) $\epsilon_{r,1} = 5.$ **(b)** $\epsilon_{r,1} = 20.$

Figure 5.1: B-scans for homogeneous halfspaces. Each trace in the B-scan is normalized with respect to its absolute maximum.

For the B-scan in Fig. 5.1a, the trace at an offset position 5.3 m is shown as an example in Fig. 5.3a. The distance to the source is sufficiently high to distinguish both DAW and DGW because they do not interfere. Note the similarity of the two waves with the initial Ricker wavelet shown in Fig. 3.7a and that the two waves have a polarity reversal. Thus, the observations for a homogeneous halfspace are in agreement with Eqs. (2.18) and (2.19). The ground wave resembles the initial Ricker wavelet the most.

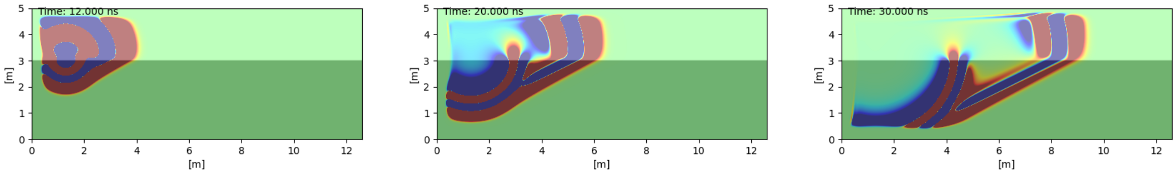

Figure 5.2: Snapshots for a homogeneous halfspace with $\epsilon_r = 5$ at 12 ns, 20 ns and 30 ns.

The observation of the frequency domain of both direct waves (Figs. 5.3b and 5.3c) reveals that the center frequency of the DAW with 161 MHz is higher than the one of the DGW with 135 MHz. To further get an impression of the frequency behavior with respect to the underlying halfspace, the center frequencies of the DAW and DGW are determined for increasing permittivities. The results are displayed in Fig. 5.4. The groundwave frequency tends to decrease, and the airwave tends to increase for increasing permittivities. Thus, both waves are sensitive to the permittivity of the soil, even the air wave which does not propagate through it. The small oscillations in Fig. 5.4, especially for the ground wave, might be caused by the manual time window placement of the picking algorithm developed by the author for this project (a detailed description is given in section 5.1.3).

In addition, the amplitude ratio of the air and ground waves is compared for increasing permittivities in Fig. 5.5. A detailed description of the methodology is given in section 5.1.2. The ratio seems to increase for higher permittivity values. It is evident that the permittivity of the subsoil affects not only the center frequencies of the respective direct waves but also their amplitude ratio. One reason for this might be the increasing reflection coefficient at the air-soil interface for larger permittivity contrasts, see Eq. (2.22). As the ratios are discussed for 2D media, it is worth examining the geometrical spreading of spherical waves in 2D and 3D media. Regardless of dimension, the energy density U is proportional to the square of the measured amplitude E: $U \propto E^2$ (Liner, 2016, p.15). In a 3D medium, the amplitude of

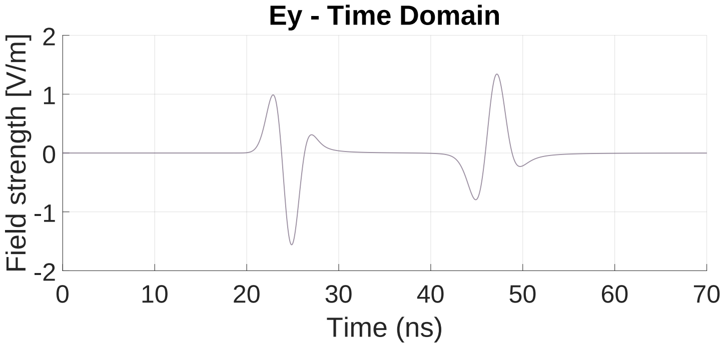

(a) A-Scan.

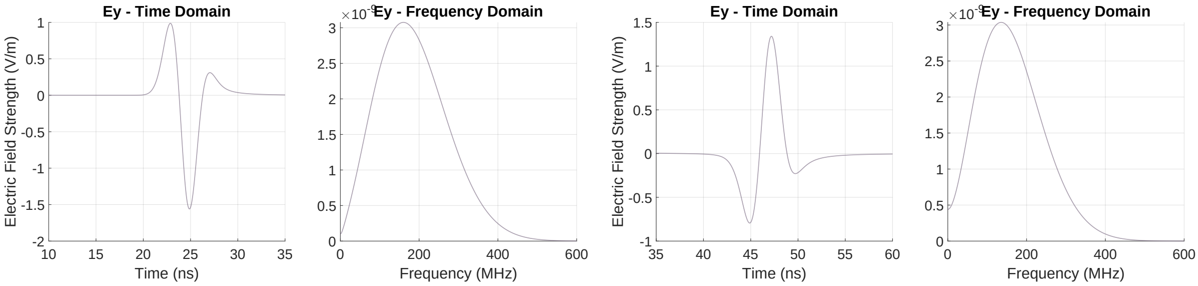

(b) DAW present in the time window from 10 to 35 ns and its FFT.

(c) DGW present in the time window from 35 to 60 ns and its FFT.

Figure 5.3: A-Scan for an offset $dx_{25} = 5.3$ m of Fig. 5.1a (homogeneous halfspace with $\epsilon_r = 5$) in (a), and time windows for the DAW and DGW in (b) and (c).

a spherical wave at a distance r decays as $E_{3D} \propto \frac{1}{r}$ because at the wavefront the energy is spread over the surface of a sphere, leading to $U_{3D} \propto \frac{1}{r^2}$. In 2D, the wavefronts are circular, leading to $E_{2D} \propto \frac{1}{\sqrt{r}}$ and $U \propto \frac{1}{r}$. Thus, the curve in Fig. 5.5 would look differently for a 3D medium, but the tendency would stay the same.

Two-layer case Before looking at the phenomena occurring in surface gradients, we want to examine the two-layer cases for both permittivity contrasts. In case of the strong contrast, which simulates unsaturated and saturated gravel, no sharp boundaries between these two will exist in nature. Instead, there might be a capillary fringe and transition zone that can be described by mathematical models

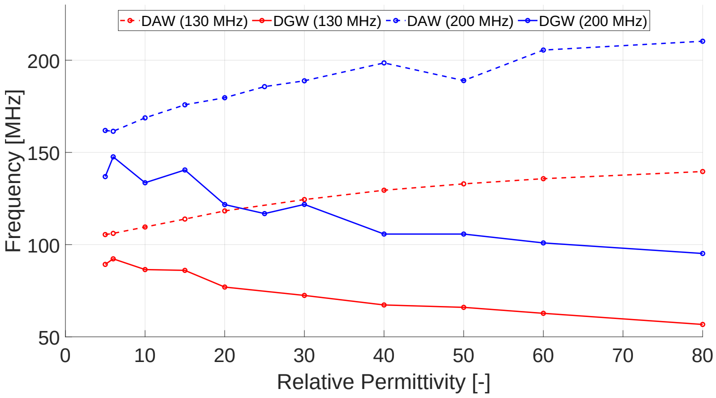

Figure 5.4: Center frequencies f_c of the DAW and DGW for increasing permittivity in a homogeneous halfspace.

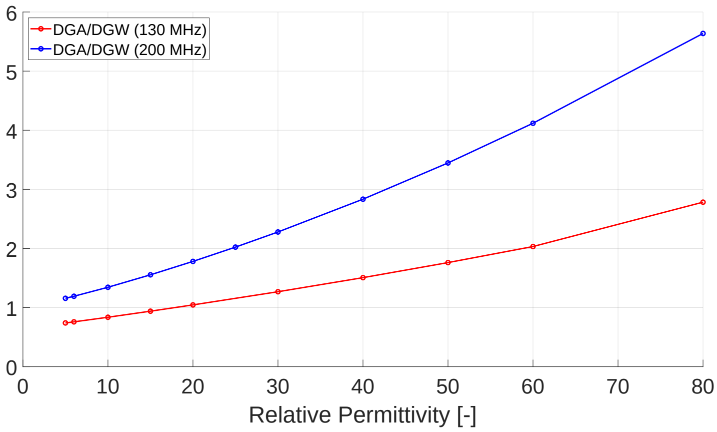

Figure 5.5: Ratio of the peak amplitude of the DAW and DGW for increasing permittivity in a homogeneous halfspace.

such as the van-Genuchten or Corey-Brooks formula. Nevertheless, it is of interest to see the behavior of GPR signals in such an environment because we can later compare it to the gradient cases. Furthermore, even stronger contrasts can occur in nature, such as ice ($\epsilon_r \approx 3.2$) overlying a water layer ($\epsilon_r \approx 80$) (van der Kruk et al., 2007).

The B-scans for different heights of the first layer for a strong contrast are displayed in Fig. 5.7. For the case with $\epsilon_{r,1} = 12.5$ and $\epsilon_{r,k} = 5$ (right column), the ground wave is ambiguous. This happens due to the presence of surface waveguides, which can be present if the underlying layer has either a lower or a much larger permittivity than the upper soil layer (van der Kruk et al., 2009). The former applies to the permittivity distribution in Fig. 5.7b ($\epsilon_{r,1} > \epsilon_{r,k}$). Then, the first layer is called a low-velocity waveguide, which allows total reflections beyond the critical angle on the upper and lower interfaces of the first layer. The EM waves are trapped within the waveguide and reflected internally, which results in a series of interfering multiples. For surface waveguides, the signal travels as an elongated wavetrain over large distances, more than 10 m, which is visible as a package of dispersed waves in the B-scan (van der Kruk et al., 2009). As a result, a lot of energy is present within a waveguide. A few selected snapshots for Fig. 5.7h are displayed in Fig. 5.6 where waveguide propagation in the upper layer (dark region) is clearly visible. In contrast to the snapshots of the homogeneous halfspace in Fig. 5.2, multiple wavefronts propagate through air apart from the DAW. They are caused by upgoing reflected waves when part of their energy is transmitted through the air-soil interface. It follows from the trace normalized B-scan that their energy must be relatively low compared to the waves within the waveguide. Note that in the right column of Fig. 5.7 almost no air wave is visible, meaning that a much higher contribution is coming from within the waveguide layer.

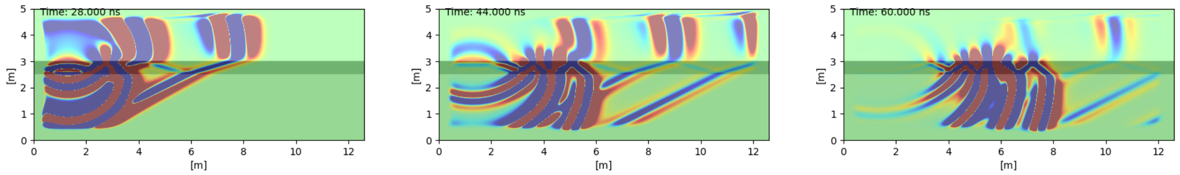

Figure 5.6: Snapshots for the two-layer case in Fig. 5.7h (strong contrast $\epsilon_{r,1} > \epsilon_{r,k}$ for $h = 50$ cm) at 28 ns, 44 ns and 60 ns. The upper soil layer (dark region) acts as a waveguide.

Additionally, the geometrical spreading within a waveguide is $E_{3D,waveguide} \propto \frac{1}{\sqrt{r}}$ due to the propagation in a confined geometry, whereas typical bodywaves have a spreading of $E_{3D,waveguide} \propto \frac{1}{r}$ (van der

Kruk et al., 2009). In a 2D medium, the discrepancy is even higher. Furthermore, the dispersive signal is characterized by the presence of shingled reflections in the data, resembling a tiled pattern on a rooftop (van der Kruk et al., 2009). One can construct an apparent phase velocity from the shingled reflections that represent the phase velocities and one overall group velocity. In Figs. 5.7f and 5.7h, the phase and group velocities are marked with dashed and solid arrows, respectively. This is one major characteristic of dispersive signals where frequency-dependent phase velocities are present. A list of three key features to identify dispersive GPR signals is given by van der Kruk et al. (2009):

1. When the data is normalized based on the maximum amplitude for each trace (trace-normalized), it becomes evident that the majority of energy is concentrated in the dispersive waves.
2. The data contains shingling reflections, which are indicators of distinct phase and group velocities.
3. The spectrum of phase velocities clearly demonstrates the existence of a phase velocity that varies with frequency.

From Fig. 5.7 it is evident that the dispersive phenomena depend on the thickness of the waveguide. Generally, dispersive-wave propagation will occur if the thickness of the upper layer is in the order of a wavelength (van der Kruk et al., 2006).

Fig. 5.7a shows a permittivity distribution for a so-called leaky waveguide. It has similar properties to the low-velocity waveguide. One major difference is that the permittivity of the underlying layer is higher and that total reflection occurs only at the upper interface. Despite the lower interface being a strong reflector, a certain amount of energy is still transmitted through it.

In our simulations, dispersive phenomena are also present in the leaky waveguide scenario for the strong contrast, but only in the case for $h = 25\,\mathrm{m}$ and $h = 50\,\mathrm{cm}$ (Figs. 5.7e and 5.7g). This can be explained by the so-called cut-off frequency $f_{cut,n}$. Below $f_{cut,0}$, there is no solution for the fundamental equation of modal theory, which describes the modes within a waveguide and accounts for dispersion phenomena. The cut-off frequencies for different n correspond to the propagation of higher-order modes. Above each cut-off frequency, the average amplitude increases strongly in the frequency spectrum. The expression $f_{cut,n}$ in Eq. (5.1) is valid for TE mode assuming that the reflection coefficient from the waveguide layer to the underlying layer is -1 (van der Kruk et al., 2007):

Height [cm]	Permittivity		
	5	6	12.5
10	375	335	221
25	150	134	88
50	75	67	44

Table 5.1: Cut-off frequencies $f_{cut,0}$ in MHz according to Eq. (5.1) for different heights and permittivities.

$$f_{cut,n} = \frac{(2n+1)c_0}{4h\sqrt{\epsilon_{r,1} - 1}} \quad \text{for} \quad n = 0, 1, 2, \dots . \tag{5.1}$$

Table 5.1 shows the respective $f_{cut,0}$ for different heights h and permittivities ϵ_r used in our simulations. We know from the previous section that the center frequencies of a $200\,\mathrm{MHz}$ source tend to be lower in soil. If the permittivity of the first layer is 12.5, waveguide propagation is observed for all thicknesses meaning that the cut-off frequency is sufficiently low to let higher-order TE modes propagate. For lower permittivities, $f_{cut,0}$ is higher than $300\,\mathrm{MHz}$ for $h = 10\,\mathrm{cm}$. We can assume that no significant frequencies are present in the ground wave in these spectral ranges. Thus, we only see dispersive behavior in the left column of Fig. 5.7 for Figs. 5.7e and 5.7g.

Fig. 5.8 displays the resulting B-scans for a weak contrast. In the case, where the upper layer has a higher permittivity than the underlying layer (right column), dispersive phenomena are observed for

$h = 25$ cm and $h = 50$ cm. They are not as pronounced as for the strong contrast, and for $h = 10$ cm the B-scan resembles the one for a homogeneous halfspace. It is important to note that a smaller contrast will result in a lower reflection coefficient and a larger critical angle θ_c. Note that a higher permittivity in the waveguide layer will lower its cut-off frequency, compare $f_{cut,0}$ for $\epsilon_r = 12.5$. In the case, where the underlying layer has a higher permittivity, dispersive behavior is only observed for $h = 50$ cm. Eq. (5.1) is valid for a reflection coefficient of -1 which is neither completely fulfilled for the weak nor strong contrast. Thus, the cut-off frequencies serve as an indicator for waveguide propagation. By visually comparing the cases of both contrasts, it follows that the amount of critically refracted airwaves is reduced significantly in the weak contrasts compared to strong contrasts. Also, the dispersive behavior is not as prominent as for strong contrasts.

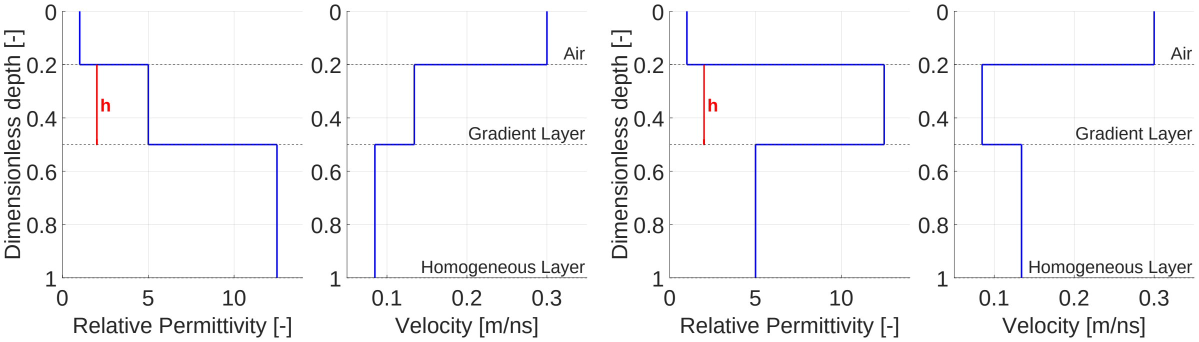

(a) Two-layer case ($\epsilon_{r,1} = 5$ and $\epsilon_{r,k} = 12.5$). **(b)** Two-layer case ($\epsilon_{r,1} = 12.5$ and $\epsilon_{r,k} = 5$).

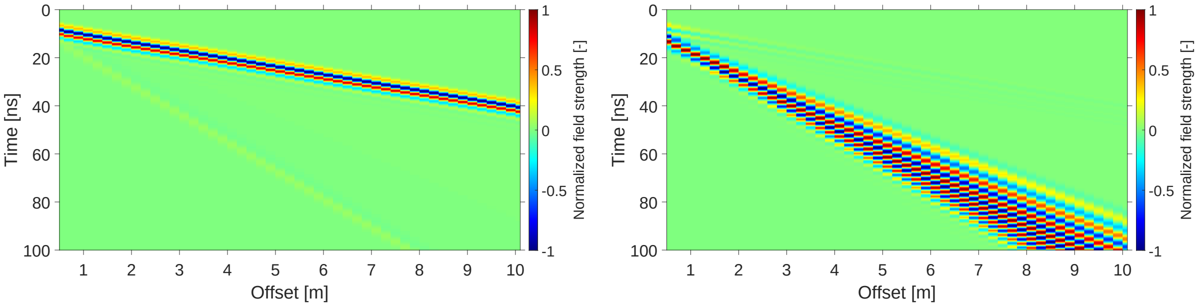

(c) $h = 10$ cm. **(d)** $h = 10$ cm.

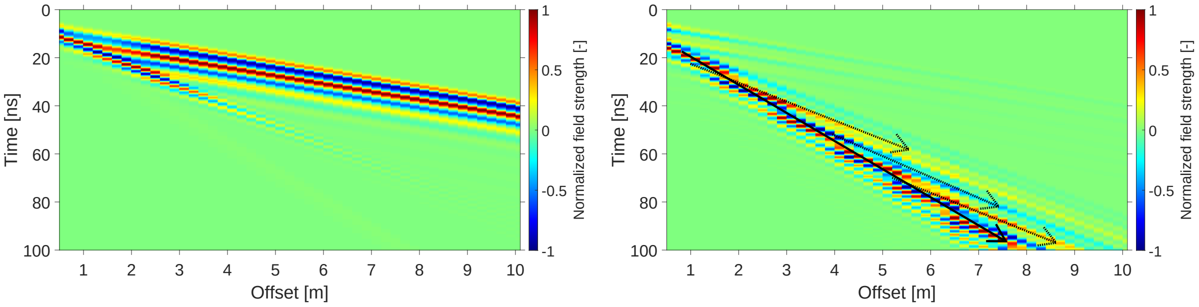

(e) $h = 25$ cm. **(f)** $h = 25$ cm.

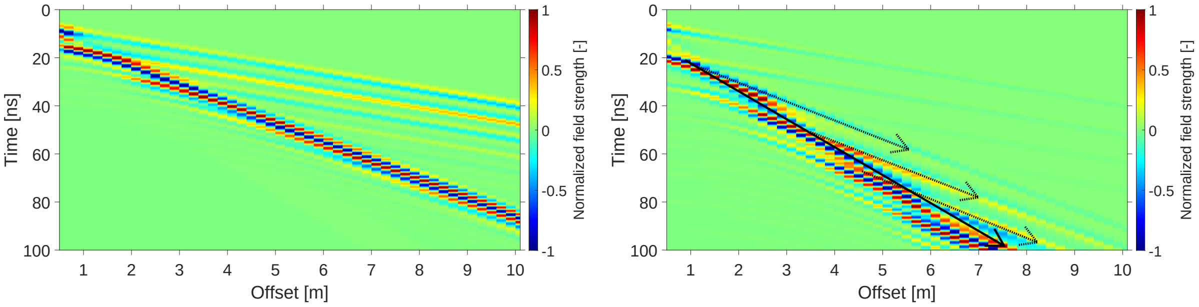

(g) $h = 50$ cm. **(h)** $h = 50$ cm.

Figure 5.7: Simulated B-scans for the two-layer case with a strong contrast. The left column shows scenarios according to (a), where the thickness h of the gradient layer is increased from 10 cm, 25 cm to 50 cm. The right column is analogous for the scenario in (b). The Hertzian Dipole is excited with a 200 MHz Ricker wavelet. Each trace in the B-scan is normalized with respect to its absolute maximum.

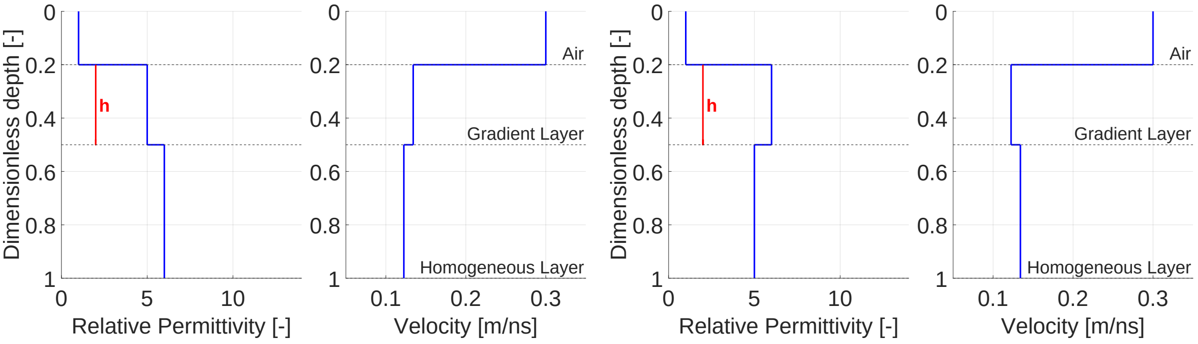

(a) Two-layer case ($\epsilon_{r,1} = 5$ and $\epsilon_{r,k} = 6$).

(b) Two-layer case ($\epsilon_{r,1} = 6$ and $\epsilon_{r,k} = 5$).

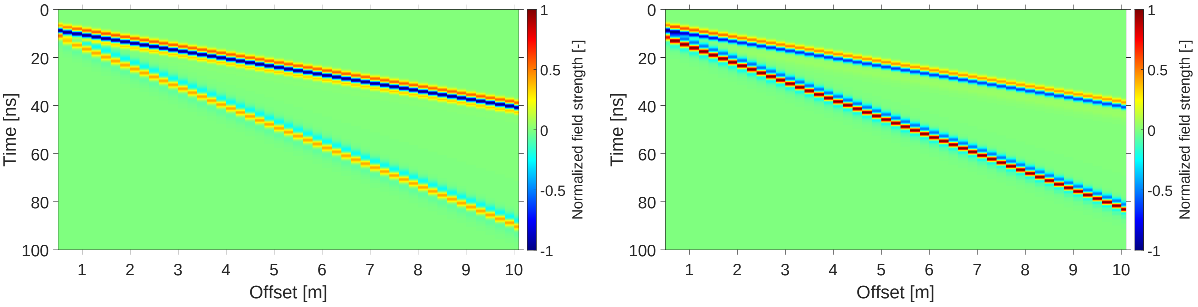

(c) $h = 10$ cm.

(d) $h = 10$ cm.

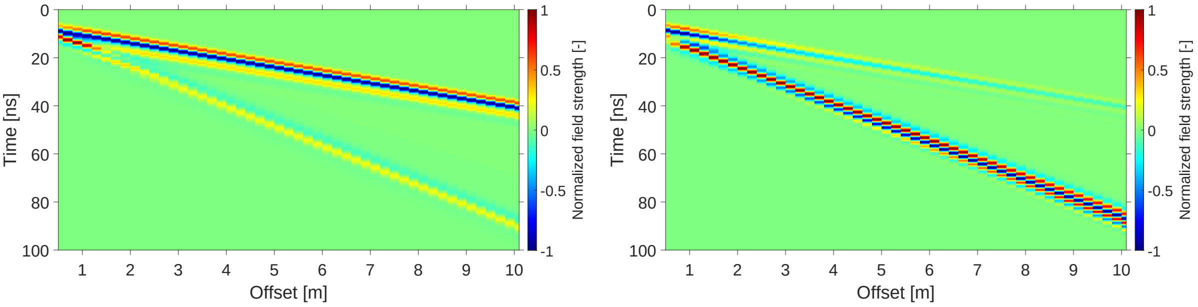

(e) $h = 25$ cm.

(f) $h = 25$ cm.

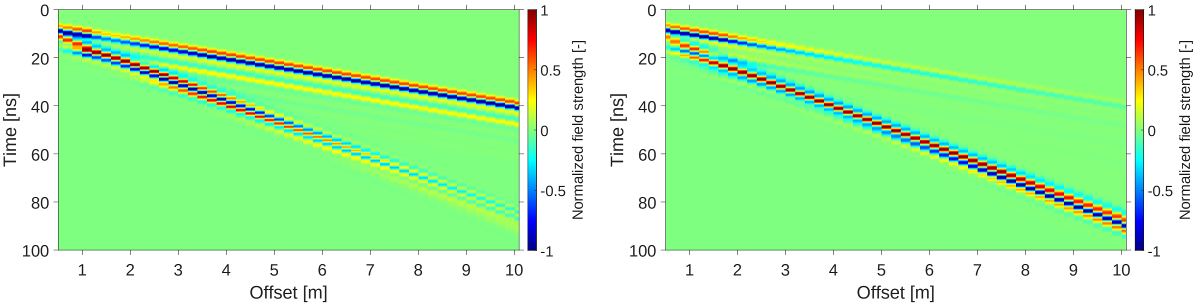

(g) $h = 50$ cm.

(h) $h = 50$ cm.

Figure 5.8: Simulated B-scans for the two-layer case with a weak contrast. The left column shows scenarios according to (a), where the thickness h of the gradient layer is increased from 10 cm, 25 cm to 50 cm. The right column is analogous for the scenario in (b). The Hertzian Dipole is excited with a 200 MHz Ricker wavelet. Each trace in the B-scan is normalized with respect to its absolute maximum.

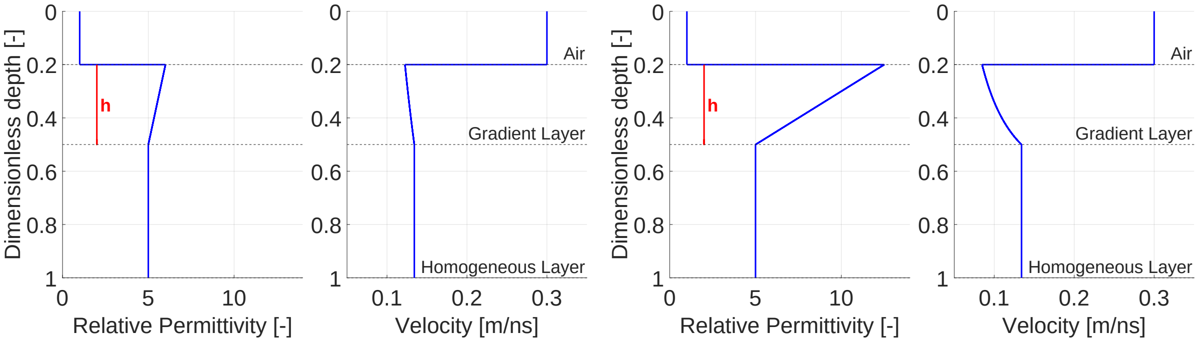
(a) Decreasing gradient ($\epsilon_{r,1} = 6$ and $\epsilon_{r,k} = 5$).

(b) Decreasing gradient ($\epsilon_{r,1} = 12.5$ and $\epsilon_{r,k} = 5$).

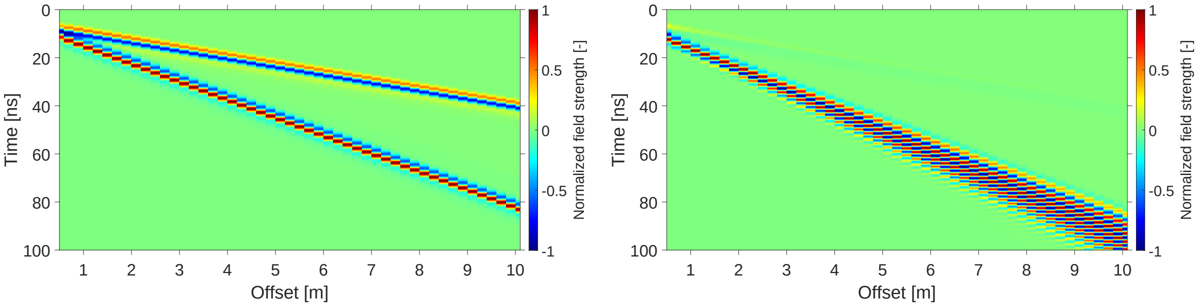
(c) $h = 10$ cm.

(d) $h = 10$ cm.

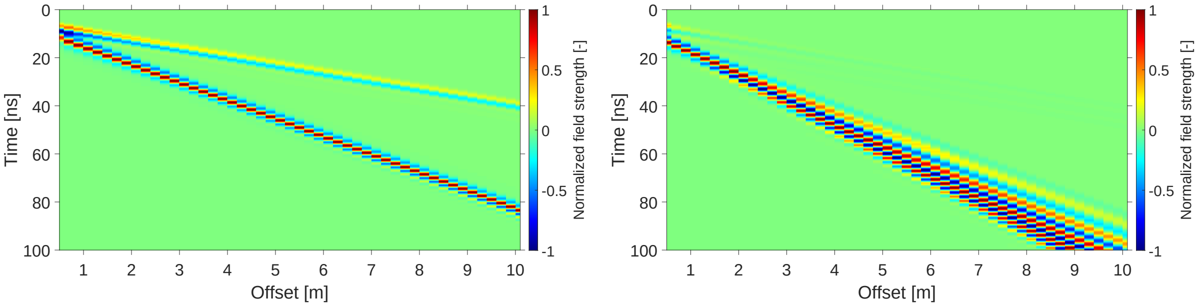
(e) $h = 25$ cm.

(f) $h = 25$ cm.

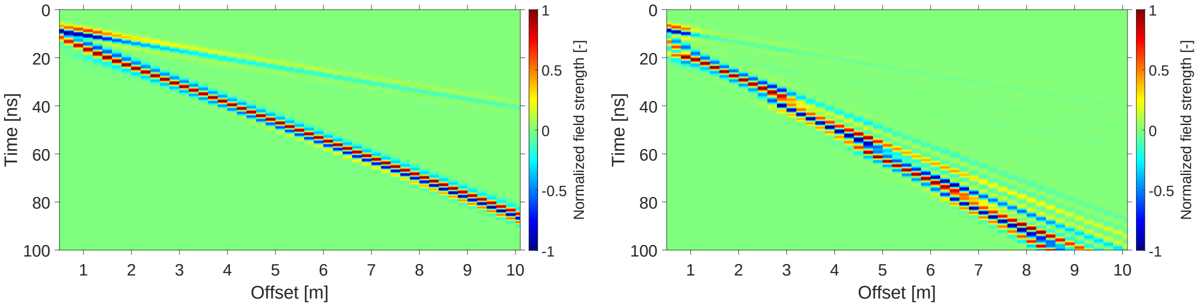
(g) $h = 50$ cm.

(h) $h = 50$ cm.

Figure 5.9: Simulated B-scans for decreasing gradients. The left column shows scenarios according to (a), where the thickness h of the gradient layer is increased from 10 cm, 25 cm to 50 cm. The right column is analogous for the scenario in (b). The Hertzian Dipole is excited with a 200 MHz Ricker wavelet. Each trace in the B-scan is normalized with respect to its absolute maximum.

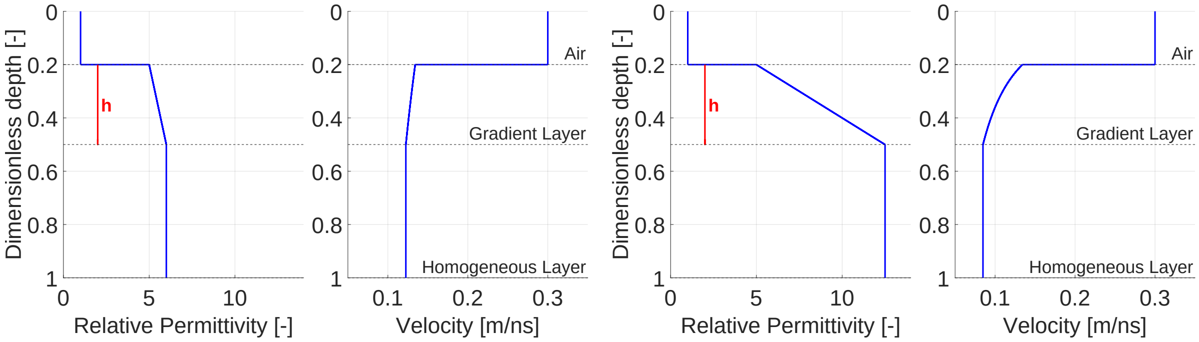
(a) Increasing gradient ($\epsilon_{r,1} = 5$ and $\epsilon_{r,k} = 6$).

(b) Increasing gradient ($\epsilon_{r,1} = 5$ and $\epsilon_{r,k} = 12.5$).

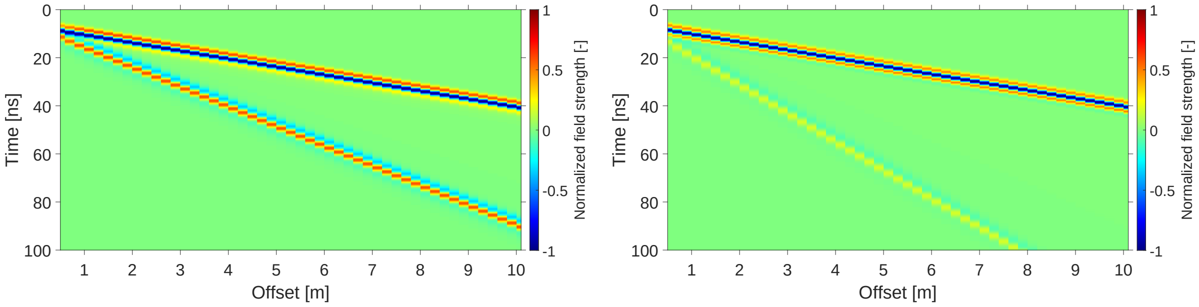
(c) $h = 10$ cm.

(d) $h = 10$ cm.

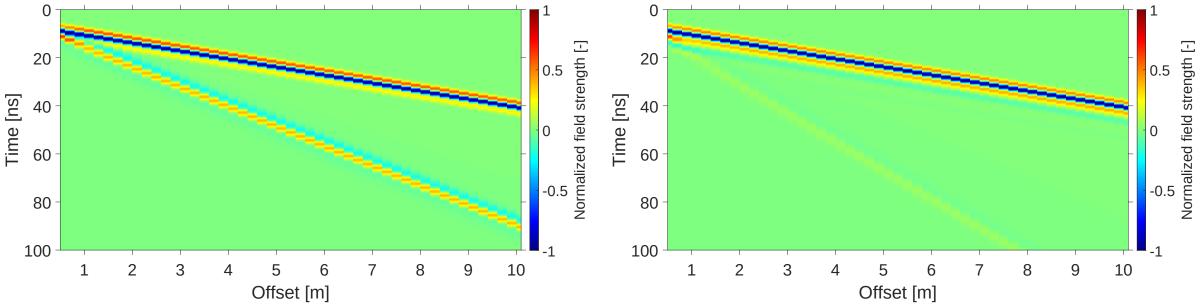
(e) $h = 25$ cm.

(f) $h = 25$ cm.

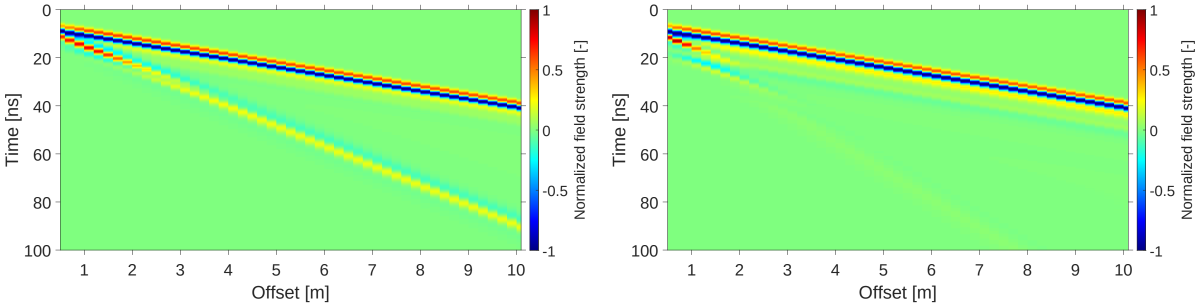
(g) $h = 50$ cm.

(h) $h = 50$ cm.

Figure 5.10: Simulated B-scans for increasing gradients. The left column shows scenarios according to (a), where the thickness h of the gradient layer is increased from 10 cm, 25 cm to 50 cm. The right column is analogous for the scenario in (b). The Hertzian Dipole is excited with a 200 MHz Ricker wavelet. Each trace in the B-scan is normalized with respect to its absolute maximum.

Decreasing gradients Fig. 5.9 shows simulations for decreasing permittivity gradients for weak (left column) and strong (right column) contrasts.

For the strong contrast, similar low-velocity waveguide phenomena as in the two-layer case are observed. The DAW is barely visible because the energy contribution coming from the ground is very high. Snapshots for the strong contrast and $h = 50$ cm are shown in Fig. 5.11 at the same time points as for the snapshots for the two-layer case in Fig. 5.6. It follows that the gradient layer can act as a waveguide. The velocity 'fan' of the ground waves coming from the waveguide seems to be narrower than for the two-layer case. To get a better impression, we visually evaluate the time window in which shingling reflections are observed for the largest offset at 10.1 m. The results are shown in Table 5.2. It seems that the time window of the two-layer case is significantly larger than the gradient, having a length of ca. factor 2 compared to the decreasing gradient. One reason for this could be that cut-off frequencies in the decreasing gradient are higher than in a two-layer case. The gradient consists of k layers whose permittivity is gradually decreased. From Eq. (5.1), it follows that a lower permittivity leads to a higher cut-off frequency. Although each layer within the gradient has a thickness of 1 cm which is significantly lower than the dominating wavelength ($\lambda \approx 42$ cm for $\epsilon_r = 12.5$ and $f_c = 200$ MHz), dispersive wave propagation occurs.

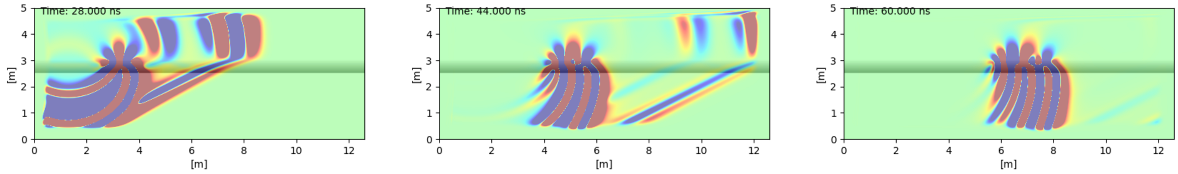

Figure 5.11: Snapshots for the decreasing gradient in Fig. 5.9h (strong contrast for $h = 50$ cm) at 28 ns, 44 ns and 60 ns. The gradient layer (dark region) acts as a waveguide.

	Two-Layer ($\epsilon_{r,1} = 12.5, \epsilon_{r,k} = 5$)			Increasing Gradient ($\epsilon_{r,1} = 12.5, \epsilon_{r,k} = 5$)		
h [cm]	t_{Start}[ns]	t_{End}[ns]	**time window** [ns]	t_{Start}[ns]	t_{End}[ns]	**time window** [ns]
10	83	128	**45**	85	111	**26**
25	87	147	**60**	85	120	**35**
50	93	158	**65**	88	120	**32**

Table 5.2: Time window of the last trace, at 10.1 m offset, where shingling reflections are present in the two-layer and decreasing gradient case. The respective times are manually picked by the author.

For decreasing gradients, it seems to be harder to see reflection hyperbolas in comparison to the two-layer case (compare to Figs. 5.7f and 5.7h). Fig. 5.12 shows two traces at 4.3 m offset for a strong contrast of a gradient and two-layer case. The dashed red line shows a critically refracted air wave, which is barely visible in the gradient case. Only with the usage of a smaller time window in Fig. 5.12b, the critically refracted air wave can be seen, as it has a very low amplitude. The red solid circles Fig. 5.12a show clearly identifiable reflections, which have the shape of the first derivative of the input wavelet, refer to section 2.2.7. They are not visible for the gradient case (green line).

For weak contrasts, there are almost no airwaves visible in the B-scan, like in the two-layer case. This means that the highest contributions are coming from the ground. Similar to the strong contrast, waveguide propagation occurs for 25 cm and 50 cm. Like in the two-layer case, no waveguide propagation is visible for 10 cm due to the high cutoff frequency (Table 5.1). In general, the B-scans for the two-layer and gradient cases resemble each other more for weak contrasts, compared to strong permittivity

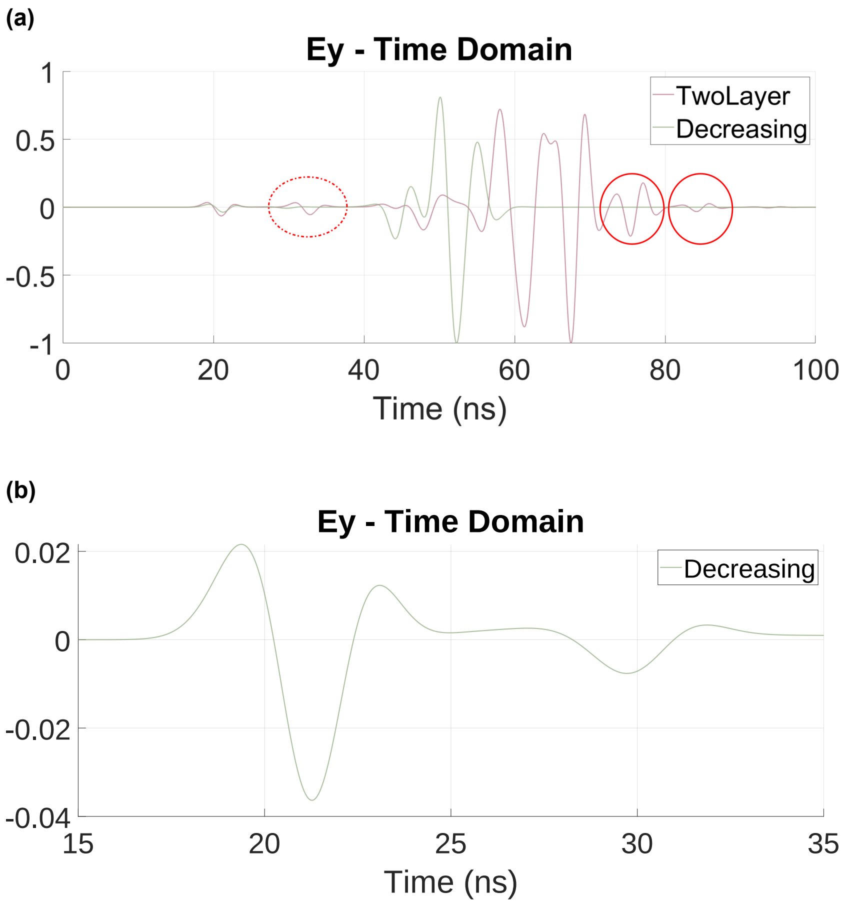

Figure 5.12: (a): Traces at 4.3 m offset from the B-scans of a two-layer case (Fig. 5.7h) and decreasing gradient (Fig. 5.10h) of a strong contrast for $h = 50$ cm. (b): Time window from 15 to 35 ns for the decreasing gradient.

contrasts. The higher the gradient thickness, the more pronounced the events coming from the ground.

Increasing gradients Fig. 5.10 shows the simulation results for an increasing gradient with low and strong contrast, respectively. The first notable aspect is that no dispersion phenomena are occurring in any scenario. The DAW and DGW are clearly separable for most scenarios. Nevertheless, the intensity of the groundwave seems to become smaller as the gradient thickness is increased. For example, the DGW is hardly visible at all in Fig. 5.10h. In contrast to the decreasing gradient, most energy contributions seem to come from the DAW. This phenomenon is intuitively understandable with the application of Snell's law, as described in Eq. (2.15). In the context of an increasing permittivity gradient, incident waves experience continuous refraction towards the incident normal, rather than the lateral direction where the receivers are positioned. Consequently, this refraction pattern limits the amount of energy received. A schematic visualization of wavefield interactions within an increasing permittivity gradient is shown in Fig. 5.13. Thus, the inspection of the snapshots for a strong contrast and $h = 50$ cm in Fig. 5.14 reveals that most of the energy in the ground is relatively quickly refracted downwards towards the homogeneous layer.

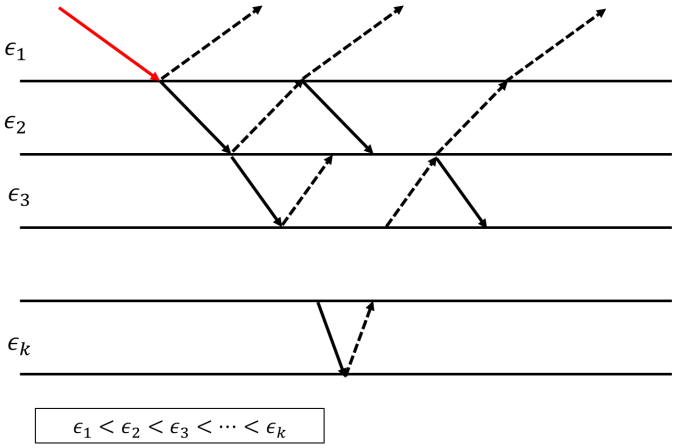

Figure 5.13: Wavefield interaction in an increasing permittivity gradient, where the gradient layer is approximated to consist of horizontal layers with infinitesimal thickness. The red arrow denotes an incident ray. The solid black arrows represent some down going wavefields whereas the dashed black arrows denote up going wavefields. In reality, the down and upward going signals can interfere, leading to highly complex down and up going wavefields.

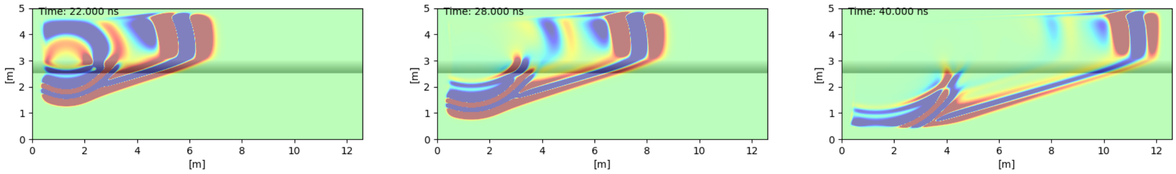

Figure 5.14: Snapshots for the increasing gradient in Fig. 5.10h (strong contrast for $h = 50$ cm) at 22 ns, 28 ns and 40 ns.

5.1.2. Amplitude analysis

To further investigate the simulation results and how the different permittivity distributions affect the observed wavefields, the ratio of the DAW and DGW is analyzed. For this, an automated picking algorithm was developed by the author, where a linear velocity line in the B-scan is manually picked by the user with a time buffer zone on each side of the line. Next, the algorithm extracts the respective time window for each trace and picks an amplitude according to a selection criterion (first local maximum or global maximum). The intermediate results of the algorithm are shown in Fig. 5.15 for a homogeneous halfspace. For the DAW, the absolute negative amplitude is picked due to the polarity reversal as shown in Fig. 5.3b and the maximum positive amplitude is picked for the DGW. If the DGW is not unambiguously identifiable, such as in waveguide propagation, the maximum amplitude within the contribution from the ground is picked. The ratio is defined as *picked amplitude from air wave / picked amplitude from ground wave*.

Although simulations are conducted in 2D and often shielded antennas are used for surface GPR applications, the amplitude ratios can still show us inherent properties of the wavefields dependent on the permittivity distribution. Tables 5.3 and 5.4 display the calculated ratios for the weak and strong contrast, respectively. Note that for the two-layer case ($\epsilon_{r,1} > \epsilon_{r,k}$) and the decreasing gradient the ratios are relatively small, especially for the strong contrast that has a ratio of less than 0.10. As expected, waveguide propagation leads to a relatively low ratio. For lower thicknesses, a higher ratio is notable because the waves in the ground do not get trapped in a surface waveguide.

The most significant observation is the pronounced ratio in the case of increasing gradients, particularly for scenarios with a strong contrast, where the ratio surpasses two-digit numbers. This might be due

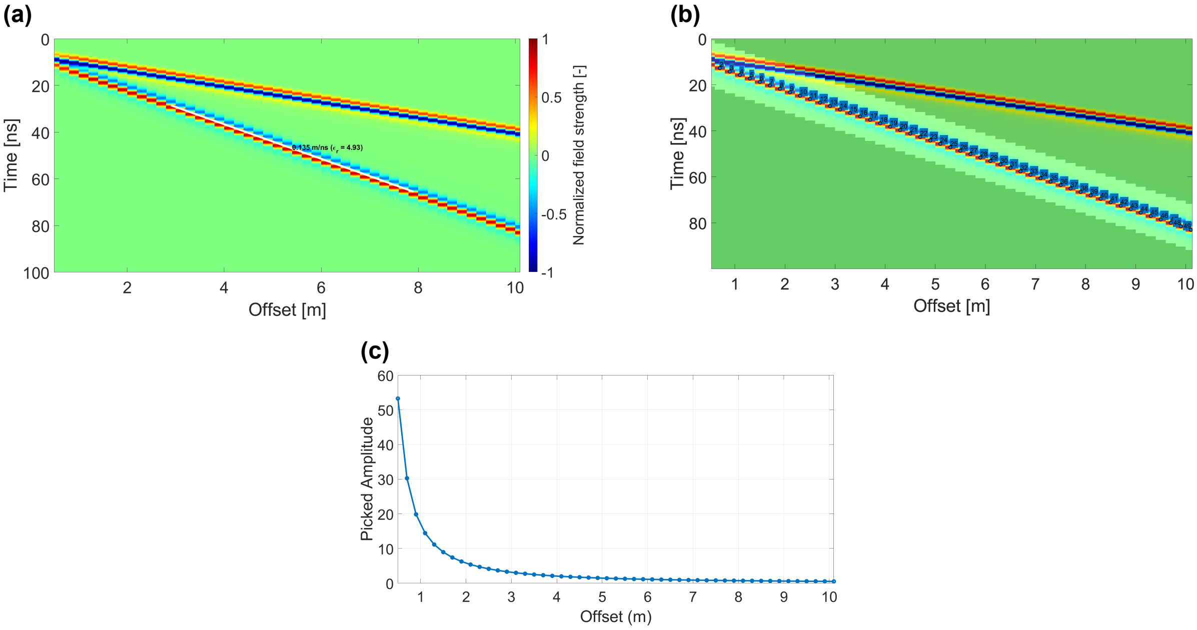

Figure 5.15: Example of the procedure for the time picking algorithm implemented by the author for the homogeneous halfspace ($\epsilon_r = 5$) in Fig. 5.3a. (a) shows the picked velocity line (in white) with $0.135\,\mathrm{m\,ns^{-1}}$ which corresponds to an estimated permittivity of 4.93 according to Eq. (2.9). (b) shows the buffer around the velocity line with 10 ns at each side (bright area) and the picked amplitudes. Each number corresponds to the position in each trace where the amplitudes are picked.(c) shows the picked amplitudes in (b).

to the lack of dispersion, where no energy is trapped in the shallow subsurface. A similar tendency is observed for the weak contrast. Additionally, Snell's law dictates that a majority of the energy gets refracted towards the incident normal, resulting in minimal energy contribution from the ground to the receivers.

h [cm]	Weak contrast			
	Two-layer ($\epsilon_{r,1} > \epsilon_{r,k}$)	Two-layer ($\epsilon_{r,1} < \epsilon_{r,k}$)	Decreasing	Increasing
10	0.224	2.450	0.746	1.690
25	0.237	4.683	0.317	2.641
50	0.643	1.517	0.189	4.807

Table 5.3: Average peak amplitude ratio of DAW and DGW for a weak contrast between an offset of 4.1 and 6.1 m.

h [cm]	Strong contrast			
	Two-layer ($\epsilon_{r,1} > \epsilon_{r,k}$)	Two-layer ($\epsilon_{r,1} < \epsilon_{r,k}$)	Decreasing	Increasing
10	0.021	21.189	0.014	6.158
25	0.049	7.107	0.016	20.030
50	0.061	0.260	0.032	55.427

Table 5.4: Average peak amplitude ratio of DAW and DGW for a strong contrast between an offset of 4.1 and 6.1 m.

5.1.3. Analysis of frequency spectra

Fig. 5.16 shows the center frequencies of DAW and DGW at the offset positions 3.1, 4.1 and 6.1 m for each simulation in Figs. 5.7 to 5.10. Each offset position undergoes a fast Fourier transform (FFT) within a time window containing the corresponding events. When the DGW is not clearly identifiable, a larger time window is selected that includes all significant events from the ground. Consequently, the values should be interpreted qualitatively rather than quantitatively, particularly for the strong contrast where waveguide propagation is observed. The first observation is that the range of the center frequencies for the DAW are more confined than for the DGW. The DAW center frequencies for the strong contrast are generally higher than for the weak contrast. It has already been demonstrated that the center frequency of the DAW is positively correlated with the permittivity of an underlying homogeneous halfspace (see Fig. 5.4). For some scenarios, the frequency of the DGW significantly varies with offset. These scenarios are associated with waveguide propagation and thus difficulties in setting the time window.

In contrast to other scenarios, it is noticeable that the DGW in all scenarios of the increasing gradient (red line) have very low center frequencies, up to less than 100 MHz. Additionally, the center frequencies of the DGW are significantly lower than the respective frequencies of the DAW. This seems to be one characteristic aspect of increasing gradients.

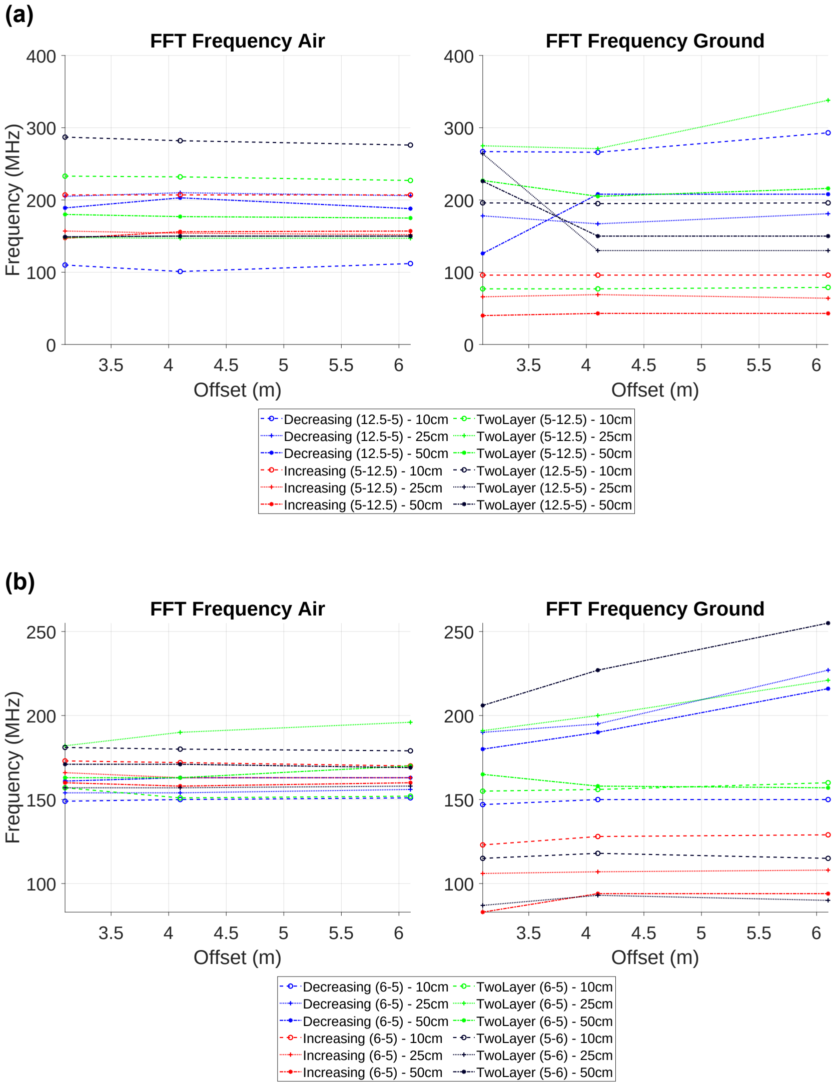

Figure 5.16: Frequency analysis of DAW and DGW for the strong (a) and weak contrast (b). The numbers in the brackets indicate the permittivity contrast $\epsilon_{r,1}$ and $\epsilon_{r,k}$ from top to bottom, followed by the thickness h.

5.1.4. Hilbert gain reveals more multiples and an additional ground wave

Next, the B-scans are inspected with the application of a gain function using the Hilbert transform. This allows the calculation of the envelope of each trace and then divides the trace by its envelope. This procedure is shown for an arbitrary signal in Fig. 5.17, where the respective original trace, its envelope, and newly scaled trace are displayed. This has been done for each B-scan shown in section 5.1.1. All B-scans from Figs. 5.7 to 5.10 are listed in the Appendix A.3. In this section, we will only show B-scans of special interest.

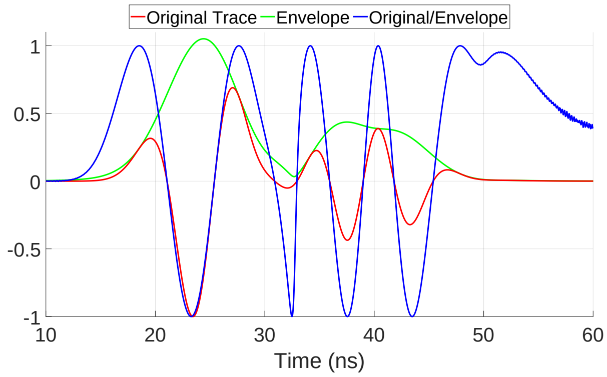

Figure 5.17: Demonstration of Hilbert gain. The original normalized trace (red) is divided by its envelope (green) to get a new scaled trace (blue). Note that towards the end (50 to 60 ns) high values with oscillations occur, although the original trace is close to zero. This is attributed to numerical artifacts provoked when dividing with small floating numbers.

(a) Two-layer case ($\epsilon_{r,1} = 6$ and $\epsilon_{r,k} = 5$).

(b) Decreasing gradient ($\epsilon_{r,1} = 6$ and $\epsilon_{r,k} = 5$).

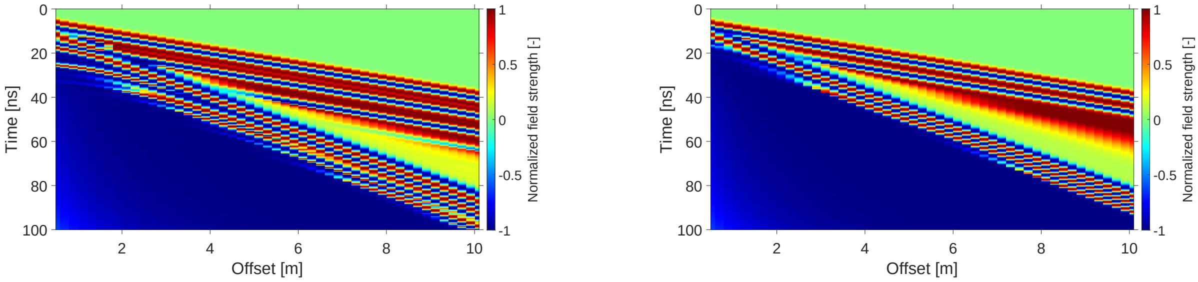

(c) Two-layer case ($\epsilon_{r,1} = 12.5$ and $\epsilon_{r,k} = 5$).

(d) Decreasing gradient ($\epsilon_{r,1} = 12.5$ and $\epsilon_{r,k} = 5$).

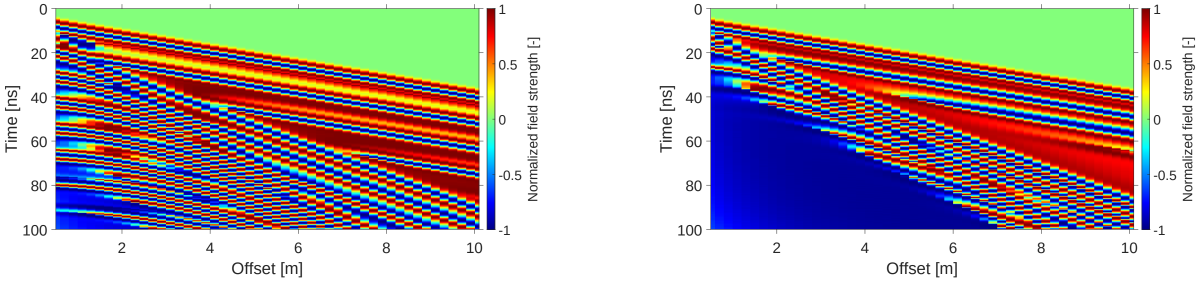

Figure 5.18: Gain function reveals multiples in selected B-scans with a thickness $h = 50$ cm.

First, the gain function reveals additional reflections that are not or only barely visible in the trace-normalized B-scans. In Fig. 5.18, we observe two-layer and decreasing gradient scenarios with weak and strong contrasts for a thickness of $h = 50$ cm. As implied in previous sections, the number of multiples in the gradient case is significantly reduced. The multiples exhibit a hyperbolic curve, as described in section 2.2.5. In the two-layer cases, multiples can be detected up to approximately 90

and $35\,$ns for strong and weak contrasts in the first trace at $0.5\,$m offset. However, in the decreasing gradient, they extend to approximately $50\,$ns for the strong contrast and are not visible for the weak contrast. These observations may be attributed to the numerous reflections and refractions occurring at each layer within the gradient layer's stratification (see Fig. 5.13). These events are likely to interfere with each other and restrict the energy reaching the air-soil interface where the receivers are positioned.

Also, some of the evaluated B-scans show apart from the DGW another linear event whose relatively low velocity certainly does not classify it as DAW or critically refracted airwave. This event is marked for the two-layer case with a weak contrast for $h = 25\,$cm in Fig. 5.19. The estimated velocity of this event is $0.120\,\mathrm{m\,ns^{-1}}$ and the one of the DGW is $0.154\,\mathrm{m\,ns^{-1}}$. The respective trace-normalized B-scan is displayed in Fig. 5.8e. As can be seen, this event is only visible for larger offsets. In the next section, we will further analyze this phenomenon and eventually classify it as a lower halfspace ground wave (LHGW).

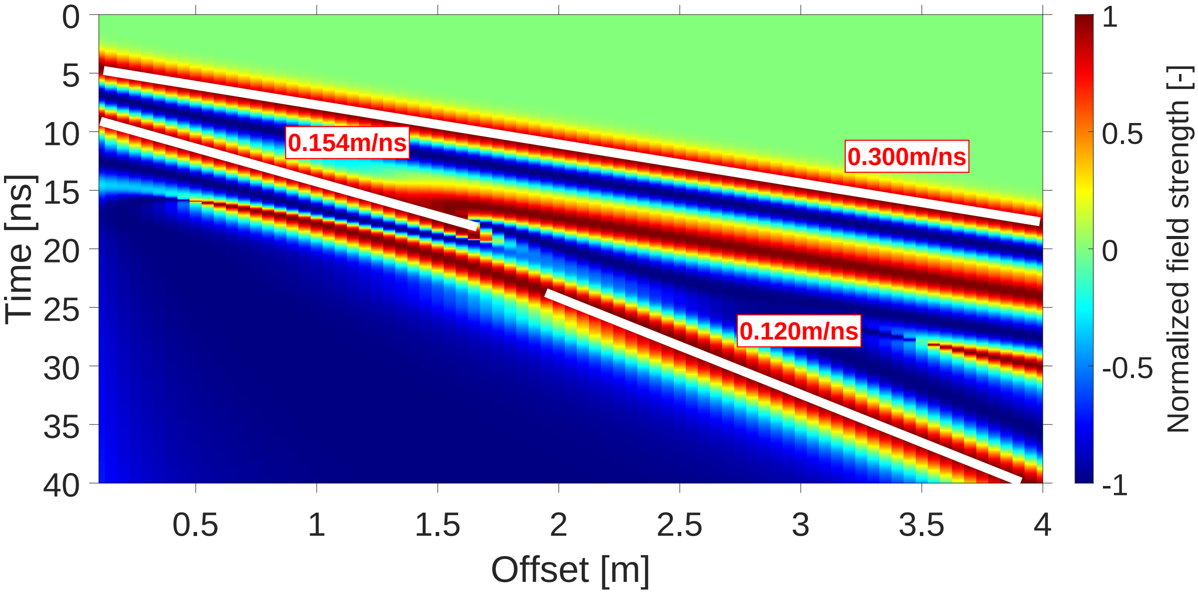

Figure 5.19: B-scan with a gain function for the two-layer case for a weak contrast with $h = 25\,$cm.

5.2. Introduction of a lower halfspace ground wave

The presence of two ground waves, whose travel times linearly increase with offset, was observed by Sperl (1999). He conducted numerical pre-studies for experimental surveys to test GPR systems for use in agricultural sites. A linear rise in permittivity ranging from 5.5 to 26 was simulated, aiming to model the gradual variation in SWC found in natural soils. Like in our model (Fig. 3.4), the gradient starts at the surface, but an additional gradient of increasing conductivity from 6.8 to $12.8\,\mathrm{mS\,m^{-1}}$ was incorporated. The explicit 2D finite difference model REFLEX (Sandmeier) was used for his simulations.

Sperl observed two ground waves with specific velocities: one with a velocity similar to the upper layer and another one with a velocity that matched the lowest layer of the gradient. He named the latter a *second ground wave*. The velocity of the second ground wave remained constant regardless of variations in the gradient thickness, while the velocity of the first ground wave depended on the sensing depth. He empirically determined the sensing depth z_s based on the simulations, which refers to the depth where the permittivity has the greatest influence on the velocity of the first ground wave (see explanations in section 2.2.3). Additionally, he introduced a so-called boundary layer depth z_g, which defines the depth of a discontinuity in the permittivity distribution to generate a second ground wave. Thus, the presence of more than one ground wave that propagates linearly with respect to the offset and time depends on both z_s and z_g, excluding interference phenomena of reflections and refractions.

Theoretically, this also applies to a two-layer medium where $\epsilon_1 < \epsilon_2$ (Sperl, 1999, p. 78). Consequently, the two marked linear events in the B-scan of Fig. 5.19 would correspond to two ground waves discovered by Sperl.

Two-layer case Calculating the respective permittivities from the estimated velocities $0.154\,\mathrm{m\,ns^{-1}}$ and $0.120\,\mathrm{m\,ns^{-1}}$ in Fig. 5.19 yields 3.8 and 6.25, respectively. While 6.25 matches the underlying halfspace (6) relatively well with a deviation of $4.2\,\%$, 3.8 deviates with $24\,\%$ from the permittivity of the upper layer (5).

To understand this discrepancy better, we subtract the B-scan of a homogeneous halfspace ($\epsilon_r = 5$) from the B-scan of the two-layer case ($\epsilon_{r,1} = 5, \epsilon_{r,k} = 6, h = 25\,\mathrm{cm}$). The difference B-scan is shown in Fig. 5.20, where the first revelation is that the DAW is not visible anymore. The arrival time of the positive peak of the DAW in the two-layer case in Fig. 5.19 is at ca. $5\,\mathrm{ns}$, whereas the first arrival time in the difference plot is at ca. $11\,\mathrm{ns}$. Inspecting a trace of the difference plot at $0.5\,\mathrm{m}$ (green line in Fig. 5.21a) reveals that there is only one wavelet present with the shape of the first derivative of the Ricker wavelet. This shape is typical for a reflected signal and leads to the conclusion that both DGW and DAW cancel out for the homogeneous and two-layer case at this offset position. At $5.5\,\mathrm{m}$ offset (blue line in Fig. 5.21a), two wavelets can be seen: (1) the critically refracted airwave at ca. $30\,\mathrm{ns}$ and (2) a ground wave having a shape similar to a negative Ricker at $50\,\mathrm{ns}$. Knowing that the homogeneous halfspace is the subtrahend in the difference plot (it is the negative term), this wavelet is very similar to the DGW for the homogeneous halfspace shown in Fig. 5.3c, when performing a polarity flip. However, the second side lobe is significantly broader than the first side lobe. This happens because the main lobe of the second ground wave is overlying the second side lobe of the DGW, where the respective traces of the homogeneous, two-layer, and difference B-scan are shown in Fig. 5.21c. For now, we assume the second ground wave propagates in the bottom layer with $\epsilon_r = 6$, according to Sperl (1999). It becomes more evident when inspecting another offset position at $9.5\,\mathrm{m}$ (red line in Fig. 5.21a): The two main lobes of the DGW and second ground wave are clearly separable, which indicates that they travel with different velocities. For $5.5\,\mathrm{m}$ and $9.5\,\mathrm{m}$, the decomposition of the traces of the difference B-scan is shown in Figs. 5.21b and 5.21d. Fig. 5.21b also explains the reason for the deviation of $24\,\%$

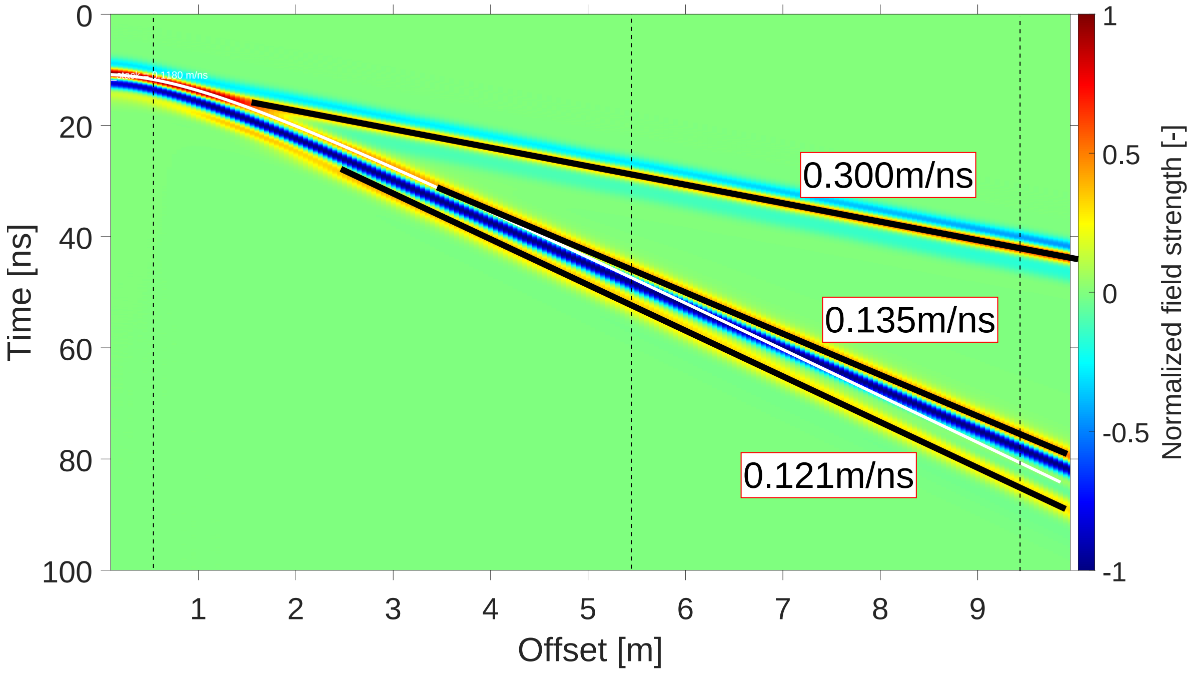

Figure 5.20: Trace normalized difference B-scan: A B-scan of a homogeneous halfspace with $\epsilon_r = 5$ is subtracted from a two-layer case with a weak contrast ($\epsilon_{r,1} > \epsilon_{r,k}, h = 25$ cm). The white line denotes the normal moveout (NMO) curve. The black solid lines denote linear events whose velocity is estimated in the text boxes. Individual traces along the dashed black lines are analyzed in Fig. 5.21.

in the velocity estimation of the DGW in Fig. 5.19. Interference of the reflected signal (green line) with the DGW (red line) creates an amplitude peak at a different time, which disturbs the estimation of the true velocity.

According to the difference B-scan in Fig. 5.20, the DGW travels with (estimated) $0.135\,\mathrm{m\,ns^{-1}}$ and the second ground wave with $0.121\,\mathrm{m\,ns^{-1}}$. This corresponds to a permittivity of 4.94 and 6.15, respectively. Both values are matching the respective layers of the original models very well.

Another phenomenon is that the amplitude of the refracted airwave is larger for an offset of 9.5 m than for 5.5 m in Fig. 5.21a. The reason for this is the trace normalized display with respect to the maximum absolute value. Due to the interference of the DGW and second ground wave, the amplitude of the negative peak increases, which is the reference for trace normalization.

In conclusion, it seems that two ground waves are indeed present in the two-layer case. One DGW with similar properties as for a homogeneous halfspace of $\epsilon_r = 5$ and a second ground wave that travels with the velocity of the underlying layer. One of the arising questions is about the travel path of this wave. To answer it, we will further examine the B-scan for an increasing permittivity gradient in the next section.

Increasing Gradient The application of a gain to the increasing gradient for a strong contrast and $h = 50$ cm in Fig. 5.22 also reveals additional events which are barely visible in the trace-normalized B-scan in Fig. 5.10h. Each event is given a name, estimated velocity, and equivalent permittivity listed in Table 5.5[1]. Note that the name for event #5 is intentionally left blank because it needs to be further analyzed. Events #2 and #5 seem to have equivalent permittivities (5.17 and 12.46) that match very well with the upper and lowest region of the gradient layer (5 and 12.5).

---

[1] Referring to the estimated velocity of event #3 in Table 5.5: A brief introduction to normal moveout is given in the Appendix A.2.

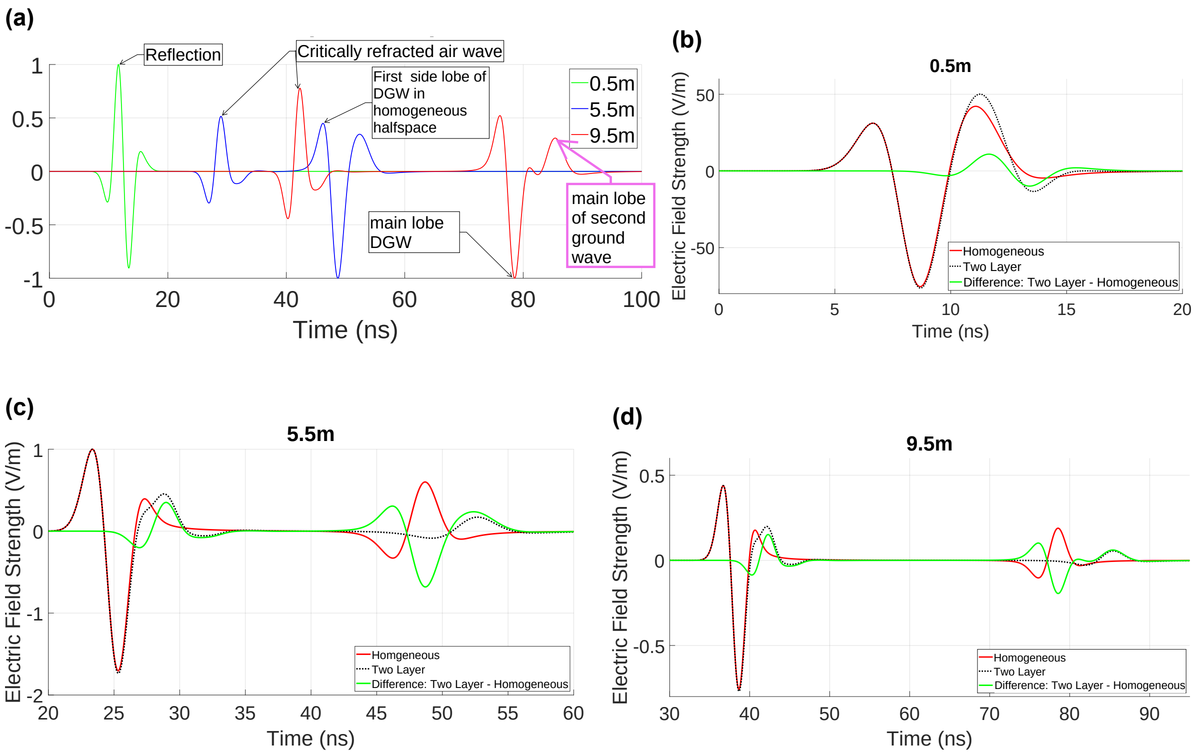

Figure 5.21: Traces that are marked at three offsets positions with dashed black lines in the difference B-scan in Fig. 5.20 in (a). Each trace is normalized with respect to its absolute maximum. (b),(c), and (d) show in detail how the traces are subtracted in the difference B-scan.

According to section 2.2.5, only direct waves have a linear relationship between arrival time and offset. It is not uncommon to see many refracted airwaves resulting from multiples in low-loss media, such as in Fig. 5.18. In these cases, the waves propagate with the velocity of free space. One critically refracted air wave is also visible in Fig. 5.22 for event #4 that starts at approximately 3.5 m offset at 35 ns. However, event #5 has a significantly lower velocity and therefore must have spread through the soil.

Label	Name	Velocity [m/ns]	Equivalent permittivity	Relation betw. time and offset
#1	DAW	0.300	1.00	linear
#2	DGW	0.132	5.17	linear
#3	Reflection	0.096*	9.77	hyperbolic
#4	Refracted airwave	0.300	1.00	linear
#5	?	0.085	12.46	linear

Table 5.5: Events labeled in Fig. 5.22. The * denotes the estimated NMO velocity.

To better understand the wave propagation, we look at selected snapshots in Fig. 5.23. We will pay special attention to the events propagating in the ground (#2, #3, and #5). While the DGW (#2) is nearly propagating at the air-soil interface in the beginning, it starts propagating downwards at 23.4 ns. Also, the reflected signal (#3) starts to propagate downward with increasing time. As implied in Fig. 5.13, waves are continuously refracted towards the normal within the increasing gradient layer.

When #3 is not propagating in the gradient layer anymore, event #5 starts to appear at 43 ns. As seen in the B-scan in Fig. 5.22, #5 continuously propagates along the interface of the gradient layer

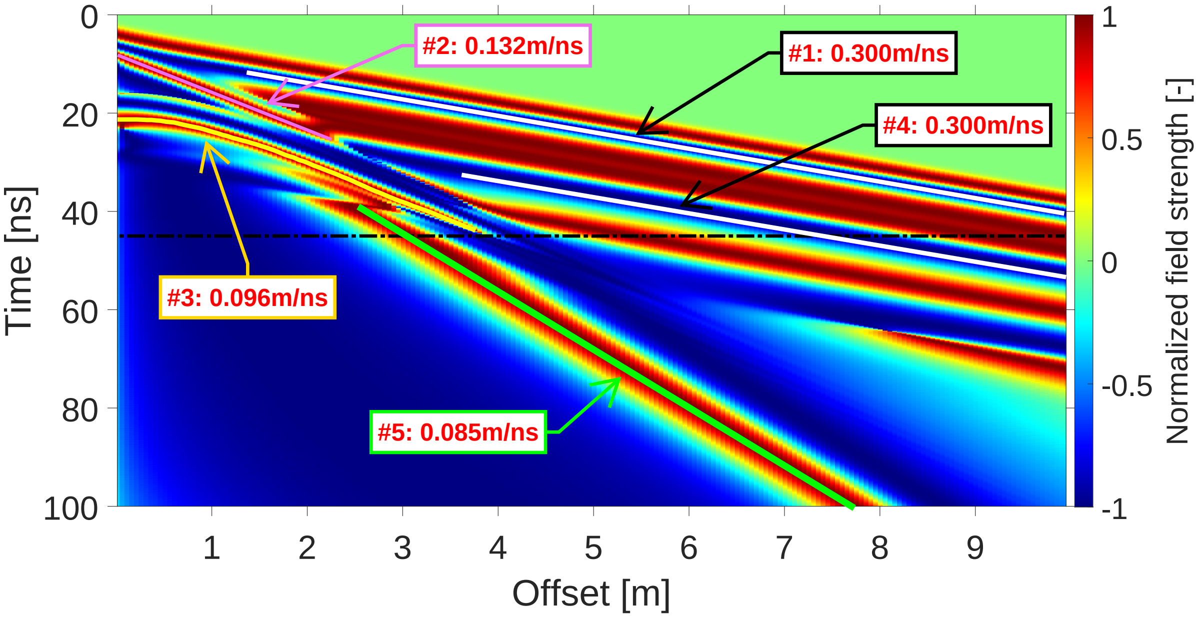

Figure 5.22: B-scan for an increasing gradient with a strong contrast over $h = 50\,\mathrm{cm}$. The dashed black line denotes the end of the time window for which snapshots are shown in Fig. 5.23.

and the homogeneous halfspace. Regarding Sperl's findings, we prefer to be more specific and name the event #5 *lower halfspace ground wave (LHGW)* instead of a second ground wave. Similarly, the second ground wave observed for the two-layer is also a *lower halfspace ground wave (LHGW)*. In contrast to the DGW, which travels directly from the source to the receiver, the LHGW is a body wave traveling below the gradient and generating an evanescent wave through the gradient that can be measured above the air-soil interface. Note that the DGW also generates an evanescent wave that travels toward the air. The difference lies in the travel paths of the evanescent waves: While the one from the DGW arises close to the air-soil interface, the one from the LHGW travels through the gradient layer which results in a higher decay. As the amplitude and frequency analysis from the last chapters were performed for larger offsets, it is likely that also the LHGW were evaluated when the amplitude ratio was significantly high and the f_c of the ground wave very low.

The evanescent wave is fed by a spherical wave and is the result of a boundary condition. It propagates with the body wave but has a different geometrical spreading (as explained in section 2.2.1). If the energy of the body wave is refracted or reflected, the evanescent wave will disappear. It may not be confused with an interface wave, such as occurring in seismic (Rayleigh or Love waves). If the spherical wave does not propagate anymore in the layer from which the evanescent wave is radiated, the evanescent wave will disappear. This scenario is more likely to happen in increasing gradient structures, as energy is continuously refracted down towards the incident normal. In contrast, decreasing gradient structures are prone to dispersion because the energy is continuously refracted away from the incident normal.

In the two-layer case in Fig. 5.19 the upper layer seemed to be sufficiently small to refract most energy of the reflected signal downwards for increasing offsets. This led to the appearance of the lower halfspace ground wave (LHGW).

Furthermore, Sperl (1999) reported the observation of an event similar to #3 and named it a *curved ground wave*. He attributed this curvature to geometrical dispersion and concluded that the spectrum emitted by the source experiences frequency-dependent damping. As his model incorporates an elec-

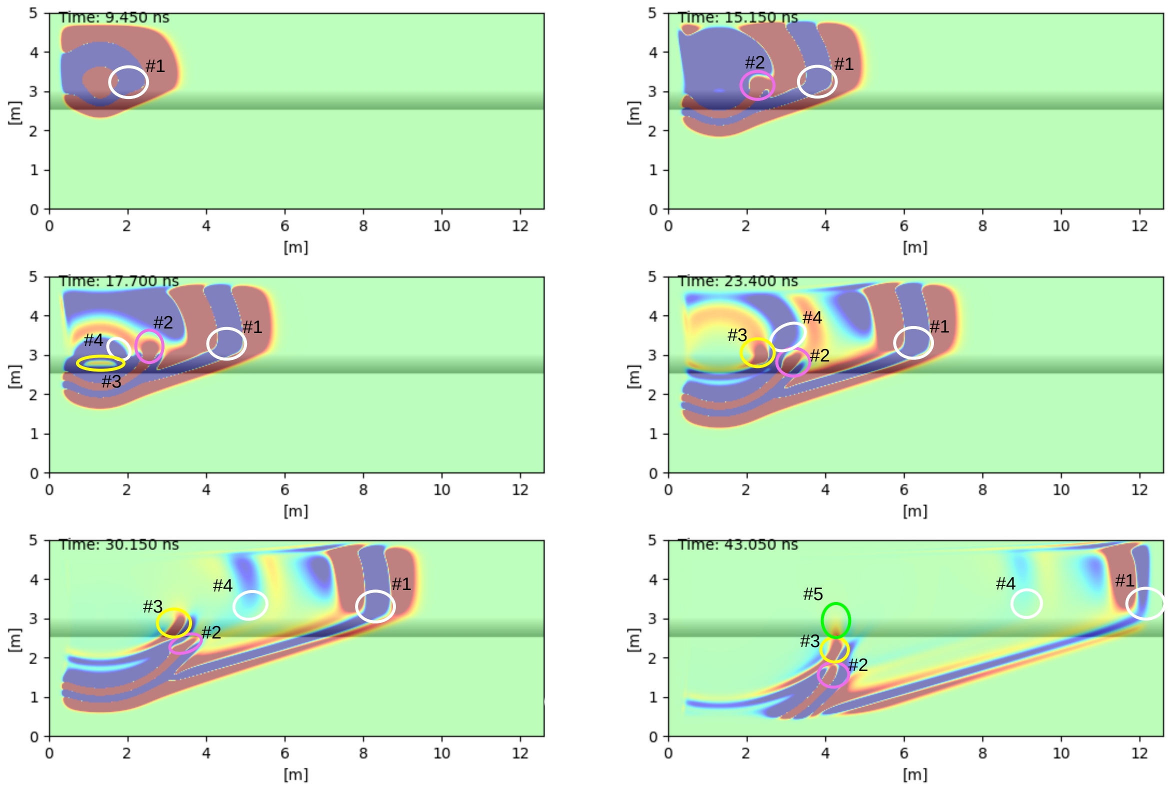

Figure 5.23: Snapshots for an increasing gradient with a strong contrast and $h = 50$ cm. The gray region corresponds to the gradient layer. The region below it is the homogeneous layer, and the region above is free space. The numbers correspond to the events in Table 5.5. The color of the circles corresponds with the colored lines in the B-scan in Fig. 5.22.

trical conductivity gradient, it would cause higher frequency components to be absorbed more in the upper layers, while low frequency components can propagate to greater depths (see Eq. (2.12a)). As the conductivity increases with depth, the amplitudes of the phase velocities are gradually dampened, resulting in this curved ground wave. The presence of a LHGW can be attributed to the increased thickness of the homogeneous layer, allowing for higher energy flow through it and better phase appearance in the radargram. From our findings, we assume that the so-called curved ground wave might be a reflection event (#3).

To further verify this hypothesis, we performed additional simulations for an increasing gradient with a strong contrast and $h = 50$ cm shown in Fig. 5.24. However, the permittivity distribution of the gradient is not as smooth anymore, as depicted in the first row of Fig. 5.24. From Figs. 5.24a to 5.24c, the permittivity gradient discretization is progressively increased to approach a smooth gradient. The according B-scans with gain are shown in the second row. The individual reflections are clearly visible in the black box in Fig. 5.24d. Referring to the depth resolution criterion in Eq. (2.13), the maximum temporal resolution for a medium of $\epsilon_r = 5$ and a center frequency of 200 MHz is ca. 16.8 cm while the one for a medium of $\epsilon = 12.5$ is 10.6 cm. This means that a higher permittivity allows for resolving thinner layers. In Fig. 5.24d, each layer thickness in the gradient is 25 cm and consequently resolvable. This is not anymore true for an increasing number of layers, especially for the upper layers with lower permittivity (Figs. 5.24e and 5.24f). Here the individual reflections merge for one pronounced reflection, while the lower layers with a higher permittivity are still resolvable. The thinner the gradient layers, the less resolvable they become. Also, the interference of up and down going reflections becomes more complex the thinner each gradient layer gets, as depicted in Fig. 5.13. Note that the LHGW becomes

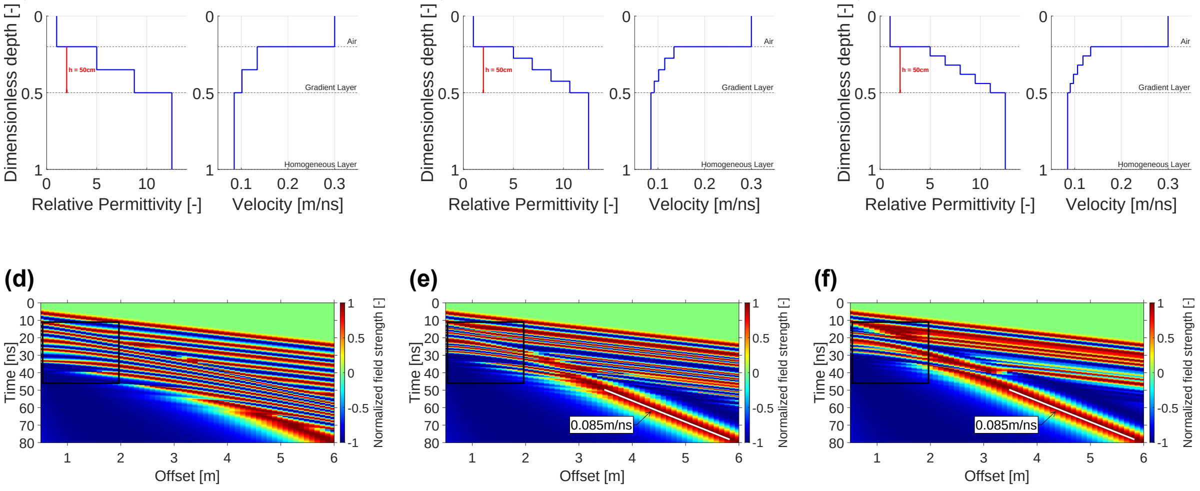

(a) $k = 2$ layers ($\Delta h = 25$ cm) in gradient with $\epsilon_{r,k} = [5, 8.75]$.

(b) $k = 4$ layers ($\Delta h = 12.5$ cm) in gradient with $\epsilon_{r,k} = [5, 6.875, 8.75, 10.625]$.

(c) $k = 5$ layers ($\Delta h = 10$ cm) in gradient with $\epsilon_{r,k} = [5, 6.5, 8, 9.5, 11]$.

Figure 5.24: B-scans for an increasing permittivity gradient with a strong contrast ($\epsilon_{r,1} = 5$ and $\epsilon_{r,k+1} = 12.5$) and $h = 50$ cm. The amount of layers k within the gradient is progressively increased as shown in the first row. The bottom row shows the respective B-scan of the distribution plot above.

better visible for a smoother permittivity distribution in Figs. 5.24e and 5.24f where it is marked with the white velocity line $0.085\,\mathrm{m\,ns^{-1}}$ which corresponds to a permittivity of 12.5. In summary, we have shown that the curved ground wave from Sperl might rather be a result of interfering reflections.

Next, we will try to estimate an equivalent location from which #3 is reflected. As this is not trivial to determine analytically due to the interference of refractions and reflections, we try a rather rustic approach for a first-order estimation. We calculate the theoretical two-way travel time for a normal incidence ray and compare it to the inflection point of #3. From this, we can map an equivalent depth from which the reflection arises. In Fig. 5.22, the inflection point of the first zero crossing is at ~ 16.3 ns. Knowing that the reflection has the shape of the first derivative of the Ricker, we choose the first cycle amplitude of the DAW as the reference point for time zero at 4.8 ns. This yields in a difference of 11.5 ns whose equivalent depth is 56 cm, according to Fig. 5.26. Knowing that the interface of the gradient with the homogeneous layer is at a depth of 50 cm, we assume that the main energy of reflection comes

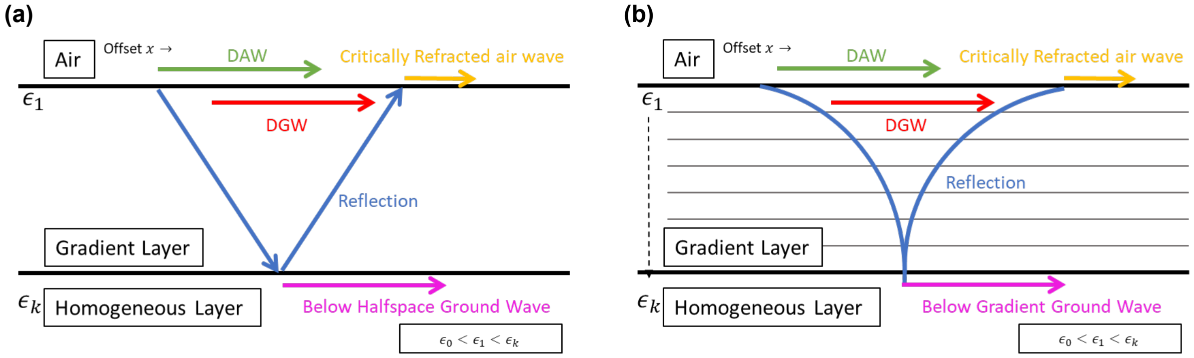
(a)
Air
Offset x →
DAW
Critically Refracted air wave
ϵ_1
DGW
Reflection
Gradient Layer
ϵ_k
Homogeneous Layer
Below Halfspace Ground Wave
$\epsilon_0 < \epsilon_1 < \epsilon_k$
(b)
Air
Offset x →
DAW
Critically Refracted air wave
ϵ_1
DGW
Reflection
Gradient Layer
ϵ_k
Homogeneous Layer
Below Gradient Ground Wave
$\epsilon_0 < \epsilon_1 < \epsilon_k$

Figure 5.25: Schematic contributions with ray-paths if a LHGW is present for a two-layer case (a) and an increasing permittivity gradient (b). For larger offsets, only the LHGW remain visible in the B-scan.

LHGW (Two-layer case in Fig. 5.19)					
Offset (m)	Measured Peak t_m	Time Zero t_0	Difference $t_m - t_0$	Calculated Arrival Time	Deviation (%)
3	32.63	6.65	**25.98**	**26.52**	2.04
5	48.85	6.65	**42.20**	**42.85**	1.52
7	65.47	6.65	**58.82**	**59.18**	0.61
LHGW (Increasing gradient in Fig. 5.22)					
3	44.58	6.65	**37.93**	**40.39**	6.09
5	67.76	6.65	**61.11**	**63.96**	4.46
7	91.62	6.65	**84.97**	**87.53**	2.92

Table 5.6: Measured and calculated arrival times of the LHGW. All times units are given in ns. The measured peak t_m refers to the arrival time of the positive peak of the respective ground waves. Time zero t_0 is subtracted from t_m for a better comparison of the propagation time. The reference point for t_0 is the negative peak of the DAW at zero offset due to the polarity shift of DAW and ground wave.

from the bottom part of the gradient. One reason to set the equivalent depth to this region could be the absence of interference between the reflection from the last layer and any later arriving reflections. This fact might result in a better identification of the arrival time of the last reflection. Nevertheless, interferences generally make it difficult to accurately determine the equivalent depth.

We assume that the LHGW has a propagation path as indicated in Figs. 5.25a and 5.25b for the two-layer case and increasing gradient. To verify this assumption, certain arrival times of both ground waves in the B-scans are evaluated. For simplicity, we assume a normal incidence throughout the gradient layer and a horizontal propagation from the start of the interface between the gradient and homogeneous layer. The approach is evaluated in Table 5.6, yielding satisfactory results for both scenarios. For the evaluated offset positions, the arrival time of the LHGW for the two-layer case can be determined with accuracies between 2.04 and $0.61\,\%$, whereas the LHGW for the increasing gradient has deviations between 6.09 and $2.92\,\%$. This might be attributed to the complex interference of refractions and reflection within the gradient layer.

In the following, the distributions of the maximum amplitudes along depth of the respective ground waves for the two scenarios in Table 5.6 are evaluated. In addition, we include the DGW for a homogeneous halfspace in Fig. 5.27d for comparison. The evaluation is achieved by placing the receivers vertically at a fixed offset position. In Figs. 5.27a to 5.27c it is evident that the rate of the amplitude decay changes at the interface where the respective DGW/LHGW are propagating (denoted with red circles). From the red circles towards the air, the amplitudes exhibit an exponential decay which is characteristic of

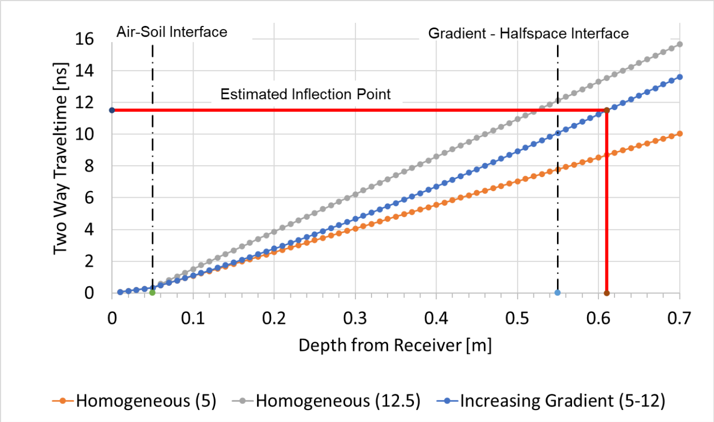

Figure 5.26: Calculated two-way travel time vs. depth for the increasing gradient model in Fig. 5.22. For comparison, the travel time for two homogeneous halfspace for permittivities (in the brackets) 5 and 12.5 are given. The estimated inflection time of $11.5\,\text{ns}$ is marked with a red line. The air-soil interface starts $5\,\text{cm}$ below the receiver, thus the equivalent depth is $61\,\text{cm} - 5\,\text{cm} = 56\,\text{cm}$.

evanescent waves. This solidifies
our assumption about the nature of the LHGW. Toward the homogeneous layer, the amplitude seems to linearly increase. In reality, the radiation characteristics for an electric dipole in TE mode is non-linear and increases with depth (Annan, 2009, Fig. 1.21). Probably, the radiation characteristics of the evaluated depth section can be linearly approximated.

Additionally, we evaluate the distribution of the center frequencies f_c of the ground waves along depth in Figs. 5.27d to 5.27f. For the homogeneous halfspace in Fig. 5.27d, we observe different trends for f_c close to the air-soil interface. Towards the halfspace, f_c stays nearly constant with a slightly increasing trend, while it significantly drops when reaching the air layer. Note that a spherical body wave travels below the interface and the DGW along the interface. Both waves exhibit a different geometrical spreading (see section 2.2.6 and 5.1). Additionally, the analytical solution for a body wave traveling in a homogeneous halfspace has an additional differentiation with respect to time (Klotzsche, 2013, Eq. (2.4)) compared to the DGW in Eq. (2.19). This can result in the body wave having a higher frequency than the DGW due to the wavelet change. The f_c drop in air could imply that the evanescent wave radiated into the air has a frequency-dependent damping. For the LHGW in Figs. 5.27e and 5.27f the f_c has no abrupt changes in trends at the air-soil interface. This could indicate that the evanescent wave is radiating from a deeper boundary and is in agreement with the results of travel time and snapshot analysis.

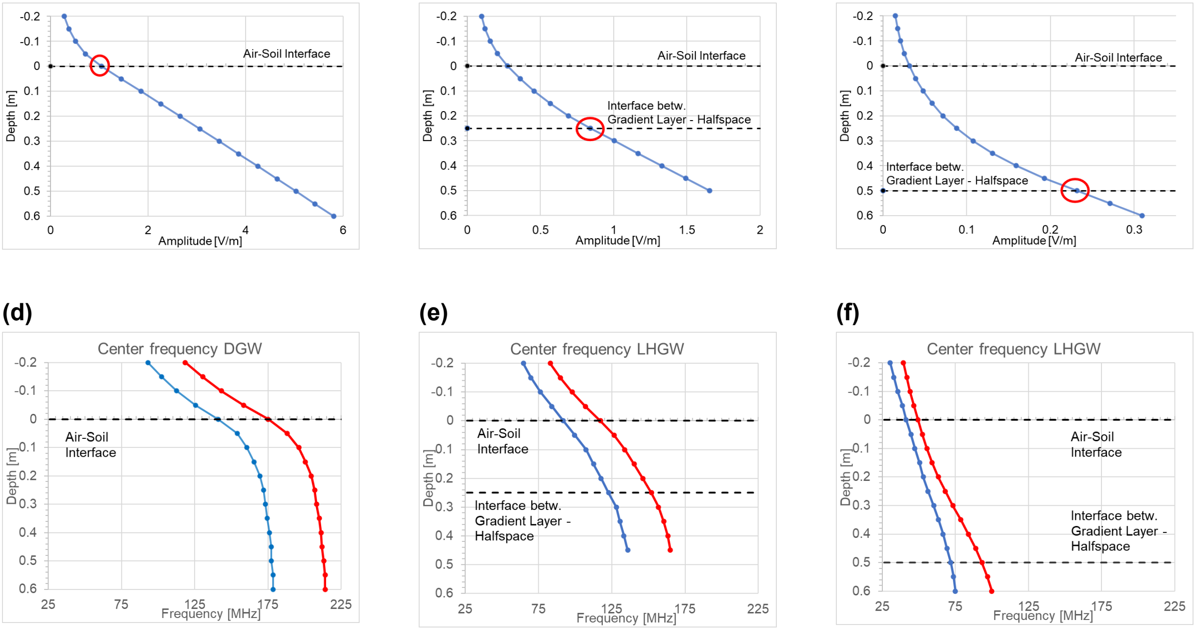
(a) DGW for a homogeneous halfspace ($\epsilon_r = 5$) at 5 m offset in Fig. 5.1a.

(b) LHGW for the two-layer case in Fig. 5.19 at 5 m offset (weak contrast).

(c) LHGW for the increasing gradient in Fig. 5.22 at 4 m offset (strong contrast).

Figure 5.27: (a-c) show the distribution of the positive maximum peak along depth for the ground waves in different scenarios. The respective center frequencies along depth are shown below in (d-f). The blue line corresponds to the FFT of a manually placed time window and the red line to an effective center frequency, where half of the signal wavelength has been manually picked in the two zero-crossing of the positive peak of the ground wave. Apparently, the effective center frequency is a good approximation for the FFT evaluation.

In addition, the presence of both waveguide propagation and a LHGW is visible for a two layer case with a strong contrast and $h = 25$ cm (B-scan with gain in Fig. A.3e). Snapshots are shown in Fig. 5.28: A part of the energy propagates within the upper layer which is classified as a leaky waveguide in section 5.1.1. Additionally, a LHGW can be seen propagating after the wavetrain with the velocity of the homogeneous halfspace.

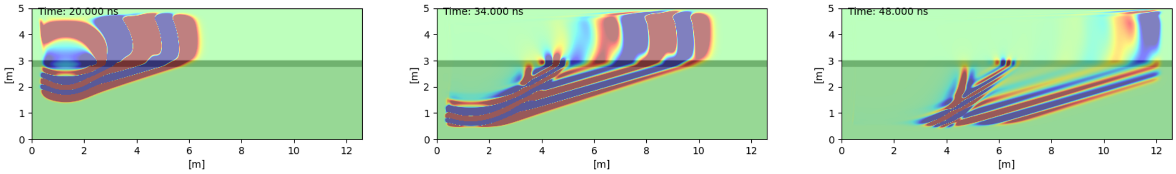

Figure 5.28: Snapshots for a two-layer case with a strong contrast ($\epsilon_{r,1} < \epsilon_{r,k}$) and $h = 25$ cm at 20 ns, 34 ns and 40 ns.

The coexistence of a DGW and LHGW can also be seen in increasing permittivity gradients with a small contrast in Fig. 5.29. Whereas the DGW is barely visible for a low gradient thickness (Fig. 5.29a), the DGW and LHGW become better distinguishable for greater ones in Figs. 5.29b and 5.29c. Note that the velocity estimation of the DGW in Fig. 5.29b is too high and yields a too low permittivity of 3.23 (the true value is in the order of 5). We can explain this analogously as we did with the difference plot for the two-layer case for the LHGW. The upcoming reflection is likely to interfere with the DGW. For even higher thicknesses, such as in Fig. 5.29c, the estimated velocities match very well with the respective layer.

(a) $h = 10\,\text{cm}$.

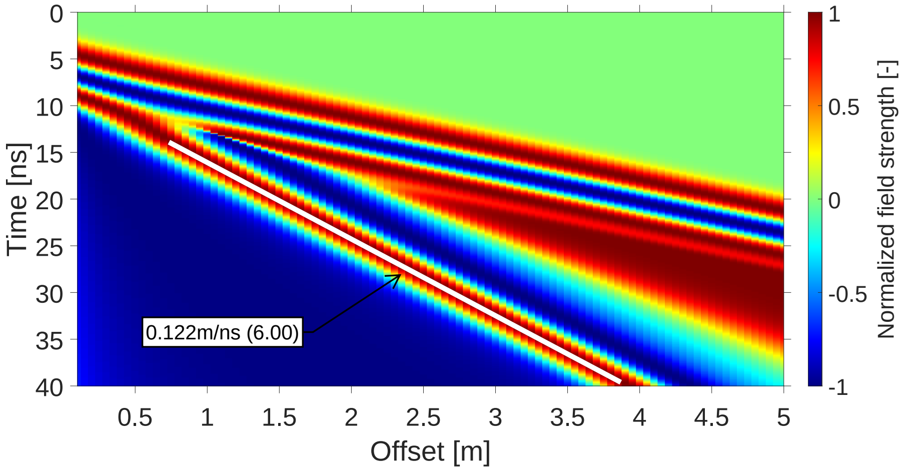

(b) $h = 25\,\text{cm}$.

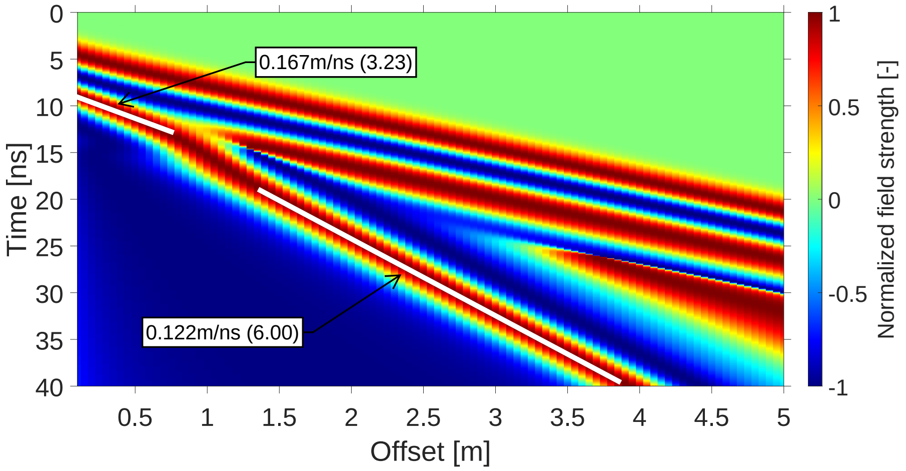

(c) $h = 50\,\text{cm}$.

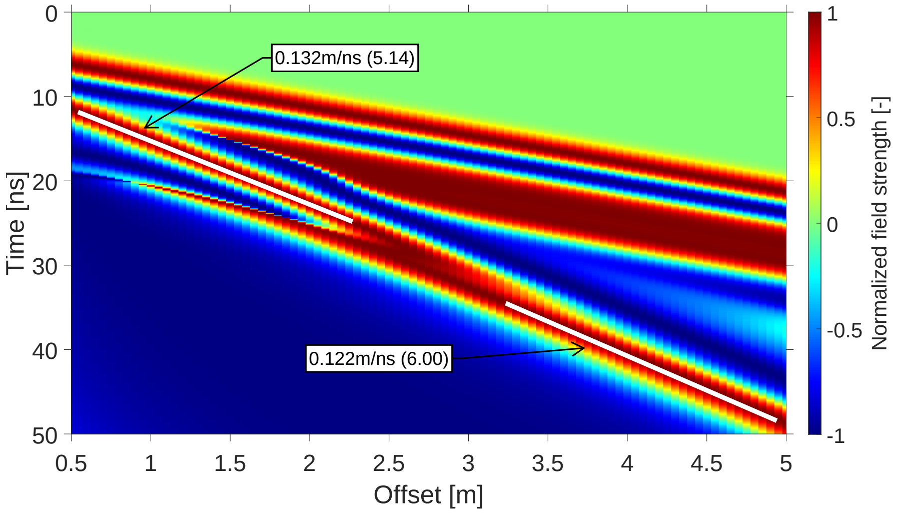

Figure 5.29: B-scans with gain for increasing permittivity gradient with a weak contrast ($\epsilon_{r,1} = 5, \epsilon_{r,k} = 6$). The marked velocities correspond either to DGW or LHGW. The number in the brackets is the equivalent permittivity.

5.3. Validation with a 3D simulation and finite-length antenna

A 3D simulation for an increasing gradient with a strong contrast and $h = 50$ cm has been conducted with an RLFLA in a broadside (TE mode) configuration. The respective 2D B-scan is shown in Fig. 5.22. In contrast to the lossless soil in the 2D simulations, the conductivity of the soil is set to 1 mS m^{-1}. The RLFLA is excited with a 92 MHz first derivative of a Gaussian pulse. For better comparison with the plots from 2D simulations, the inverted data (multiplication with -1) is shown in Fig. 5.30. Like in the 2D simulations, we can clearly distinguish a DGW and LHGW with estimated velocities of 0.138 and 0.085 m ns^{-1}, respectively. This yields equivalent permittivities of 4.73 and 12.6 that match the upper and lowest layer.

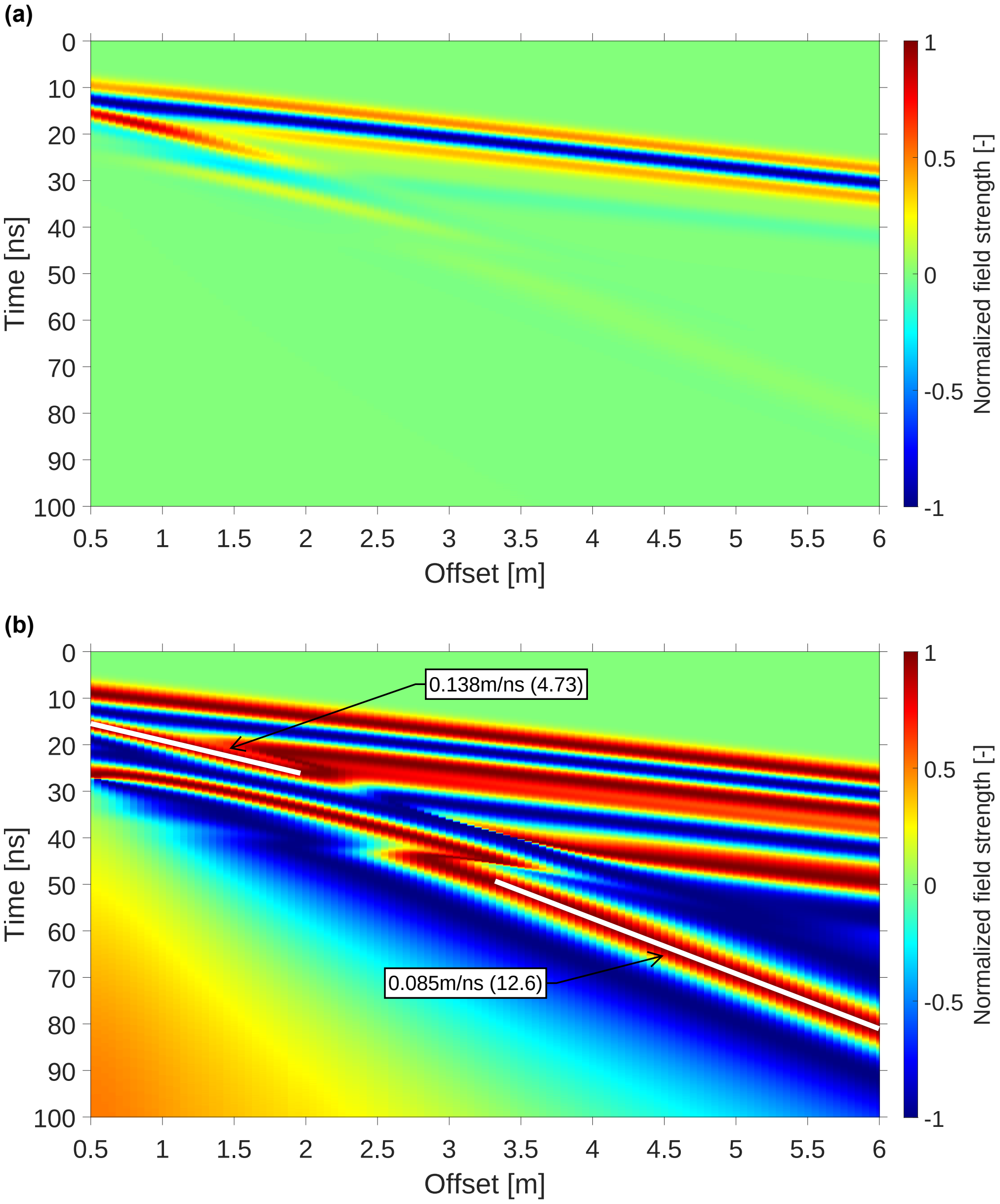

Figure 5.30: 3D simulation for an increasing gradient with a strong contrast and a RLFLA as source. (a) Trace normalized B-scan. (b) B-scan with gain. The marked velocities in (b) correspond either to DGW or LHGW. The number in brackets is the equivalent permittivity.

5.4. Summary: Observed wavefield phenomena for different permittivity distributions

In the following, we provide a brief summary of the main findings from analyzing the four different permittivity distributions introduced in section 3.5. Note that we limit this summary only to clearly visible phenomena, thus not the same aspects are compared and discussed for each case.

Homogeneous halfspace

- In the B-scan, only the DAW and DGW are visible.
- The DAW and DGW are polarity flipped with respect to each other.
- The center frequency of the DAW is higher than the one of the DGW.
- The energy density of the DAW is greater than the DGW. The higher the permittivity of the soil, the higher its amplitude ratio.

Two-layer case

- In addition to the DAW and DGW, multiple reflection hyperbolas from the two-layer interface and critically refracted air waves can be present in the B-scan.
- For certain scenarios, a lower halfspace ground wave (LHGW) is observed to be present apart from the DGW. The LHGW propagates along the interface of lower halfspace to the upper halfspace.
- The measured part of the LHGW is an evanescent wave starting at the interface of the upper with the lower layer, whose center frequency strongly decays towards the air-soil interface. In addition, the LHGW is likely to be measured only for thin upper layers. If the thickness is too large, the exponential damping of evanescent waves results in an amplitude too low to be measured.
- Depending on the contrast and layer thickness, the DGW/LHGW can interfere with upcoming reflections, which makes their determination difficult. Nevertheless, the LHGW could be seen in a B-scan where the upper layer is a leaky waveguide.
- The upper layer can act in certain cases as a waveguide. For a low-velocity upper layer, a low-velocity waveguide is present, such that beyond the critical angle, total reflections occur at the lower and upper interfaces. For a very low-velocity halfspace, a leaky waveguide can be present, resulting in a large reflection coefficient at the lower interface and total reflection at the upper interface (see van der Kruk et al., 2009 for more details). The presence of waveguides can interfere with the DGW.

Decreasing gradients

- For a sufficient high permittivity contrast, waveguide propagation according to van der Kruk et al. (2009) is visible.
- The dispersive behavior in a decreasing gradient is more confined in time than in a two-layer waveguide with the same thickness and the maximum permittivity of the gradient layer.
- There are significantly fewer refracted air waves and multiples compared to two-layer cases with the same thickness and and the maximum permittivity of the gradient layer.

Increasing gradients

- A significantly higher air to ground wave ratio than any other evaluated permittivity model was observed.
- The evaluated gradients did not act as waveguides.
- Interferences of multiple reflections from the infinitesimal layers within the gradient occur. Careful analysis has shown that the lower interface of the gradient is visible by a constructively interfering reflection event.
- A characteristic feature seems to be the lower halfspace ground wave (LHGW) that propagates at the interface between the gradient and the homogeneous layer, analogously to LHGW in the two-layer case. The LHGW and DGW can coexist in one B-scan.
- The measured LHGW is an evanescent wave directed towards the surface. For the analyzed scenarios, the center frequency of the LHGW is significantly lower than the one of the DAW.

6

Conclusion and Outlook

Borehole model simulations A 3D model in the finite difference time-domain (FDTD) solver gprMax was built to simulate crosshole GPR. Furthermore, a resistor loaded finite-length antenna (RLFLA) model was developed to thoroughly study the finite-length antenna effects in boreholes with a realistic approach and compare it to a point source. As the finite-length antenna is excited with a voltage source, its excitation wavelet was chosen to be an integration of the excitation wavelet of the point source. This resulted in the measured wavelets having similar shapes and being better comparable. The comparison between the radiation characteristics of a point source and RLFLA in crosshole GPR applications revealed only minor differences between the two. Unlike previous studies, where significant changes in the received wavelet for unloaded finite-length antennas were observed depending on the vertical offset, our resistive loading probably did not contribute a significant amount to the final shape of the wavelet. Both the received wavelets for point and finite-length sources exhibited similar behavior in simulations and when placed in free space or water-filled boreholes with small radii, regardless of the vertical offset ranging from 0 and $60°$. The borehole radius was identified as a critical factor influencing the received signal, as it can function as a cylindrical waveguide for certain dimensions. This leads to long oscillations in the received signal due to the interferences of trapped waves within the waveguide. Due to the high sensitivity to the borehole radius, it might still be worth including a finite-length antenna in the model to capture realistic wavefield interaction with the borehole in the forward model. In contrast to the RLFLA, the point source is a soft source, meaning that it is transparent and does not interact with any incident wavefields. Considering that multiple reflections can occur within the borehole, including a finite-length antenna could caption realistic wavefield interactions better.

It is essential to note that this study only examined the phenomena for one RLFLA model. Different trends may emerge for other crosshole antenna models or when dealing with straight ray angles greater than $60°$. Further research is needed to explore these possibilities.

At the end of this project, a notable announcement was made regarding the new release of gprMax. Its latest version incorporates a sub-gridding tool, which enables users to define varying spatial resolutions within different areas of the main grid. This should allow for even finer and more realistic modeling of the borehole and the RLFLA while having a different mesh size for the rest of the domain. In our simulations, we used a uniform spatial discretization of $1\,\mathrm{cm}$. For a 3D model containing domain sizes bigger than $5\,\mathrm{m}$, this resulted in high computational demand. If the sub-gridding tool was used, even finer modeling of the antenna might be possible while keeping the computational cost reasonably low.

Gradient model simulations For surface GPR, we built a 2D model in gprMax that can obtain different permittivity distributions accounting for a homogeneous halfspace, a two-layer case, and decreasing or increasing surface permittivity gradients. We tried to analyze each permittivity distribution for its characteristics. The results obtained from the gradient models reveal that a gradual transition from one medium to another exhibits distinct characteristics compared to a simple homogeneous or two-layer case. Many of the decreasing gradients that were studied exhibited similar phenomena observed in low-velocity waveguides for two-layer cases. Moreover, we could observe phenomena that were lastly investigated more than two decades ago in the context of GPR (to the best of our knowledge). We could continue on the work from Sperl (1999) and classify the former second groundwave as a lower halfspace ground wave (LHGW) for increasing permittivity gradients. For certain permittivity distributions, both the direct ground wave (DGW) and LHGW coexisted in the same B-scan. The DGW only was visible for lower offsets while the LHGW emerged for larger offsets. Whereas the DGW travels directly from the source to the receiver, the LHGW travels below the gradient. Both waves generate evanescent waves that propagate toward the air where they can be measured. Due to the larger travel path for the evanescent wave arising from the LHGW its amplitude has decayed significantly when measured above the air-soil interface. For two-layer cases where the upper layer is sufficiently thin, we also observed a lower halfspace ground wave (LHGW). Furthermore, the presence of a curved groundwave was reported to be a result of geometrical dispersion due to varying permittivity and electrical conductivity along the depth. We could demonstrate that the former named curved groundwave is likely to be the result of interfering reflections.

Although most of our simulations were conducted in 2D, similar phenomena are expected in a 3D domain because all materials were invariant in the horizontal direction. Nevertheless, these phenomena should be further investigated in 3D, mainly because of a more realistic geometrical spreading of the waves. Furthermore, this study assumed a uniform electrical conductivity. Assessing the wave fields with the corresponding conductivity gradients could lead to more realistic results. The sub-gridding tool introduced in the last paragraph of ”Borehole model simulations” could be applied for the gradient layer to be smoother and have an even finer discretization than 1 cm. As of now, the presence of both the DGW and LHGW has not been explicitly measured simultaneously in a B-scan. Experimental verification of their existence would be an important step toward better understanding complex wave phenomena within gradients. Furthermore, the numerically verified existence of the LHGW could indicate that some experimental setups to determine the sensing depth of the DGW did actually measure the LHGW which propagated along the lower halfspace.

Conventional full waveform inversion (FWI) might encounter challenges in reconstructing some of these discussed models due to the complex wavefield phenomena occurring in gradients. For example, the LHGW probably could not have been recovered by conventional inversion algorithms. The next steps could involve incorporating parameters that account for surface permittivity gradients into the starting models of FWI, such as introducing a gradient height h and a starting value for permittivity $\epsilon_{r,1}$. It might be possible that permittivity gradients are the reason why some inversion algorithms encounter difficulties in minimizing the cost function of the measured data. If any characteristic feature for gradients is observed in these datasets, it might be worth accounting for them in the starting model and checking if the goodness of fit increases. Regardless, it appears that the old saying *nature non facit saltus* is valid to be considered in the FWI workflow.

Bibliography

Annan, A. P. (2005). 11. Ground-Penetrating Radar. In D. K. Butler (Ed.), *Near-surface geophysics* (pp. 357–438). Society of Exploration Geophysicists. https://doi.org/10.1190/1.9781560801719.ch11

Annan, A. P. (2009). Chapter 1- Electromagnetic Principles of Ground Penetrating Radar. In *Ground Penetrating Radar Theory and Applications* (pp. 1–40). Elsevier. https://doi.org/10.1016/B978-0-444-53348-7.00001-6

Arcone, S. A. (1995). Numerical studies of the radiation patterns of resistively loaded dipoles. *Journal of Applied Geophysics*, *33*(1-3), 39–52. https://doi.org/10.1016/0926-9851(95)90028-4

Basu, P. K., & Dhasmana, H. (2023). *Electromagnetic Theory* (1st ed. 2023). Springer International Publishing; Imprint Springer. https://doi.org/10.1007/978-3-031-12318-4

Bell, J. L. (2005). *Continuity and Infinitesimals*. Retrieved July 9, 2023, from https://plato.stanford.edu/entries/continuity/

Benedetto, A., & Pajewski, L. (Eds.). (2015). *Civil Engineering Applications of Ground Penetrating Radar*. Springer International Publishing. https://doi.org/10.1007/978-3-319-04813-0

Bonan, G. B. (Ed.). (2019). Soil Temperature. In *Climate change and terrestrial ecosystem modeling* (pp. 64–79). Cambridge University Press. https://doi.org/10.1017/9781107339217.006

Buechler, D. N., Roper, D. H., Durney, C. H., & Christensen, D. A. (1995). Modeling sources in the FDTD formulation and their use in quantifying source and boundary condition errors. *IEEE Transactions on Microwave Theory and Techniques*, *43*(4), 810–814. https://doi.org/10.1109/22.375228

Busch, S. (2014). *Full-waveform inversion of surface ground penetrating radar data and coupled hydrogeophysical inversion for soil hydraulic property estimation: Zugl.: Aachen, Techn. Hochsch., Diss., 2013* (Vol. Bd. 202). Forschungszentrum Jülich.

Busch, S., van der Kruk, J., Bikowski, J., & Vereecken, H. (2012). Quantitative conductivity and permittivity estimation using full-waveform inversion of on-ground GPR data. *GEOPHYSICS*, *77*(6), H79–H91. https://doi.org/10.1190/geo2012-0045.1

Busch, S., van der Kruk, J., & Vereecken, H. (2014). Improved Characterization of Fine-Texture Soils Using On-Ground GPR Full-Waveform Inversion. *IEEE Transactions on Geoscience and Remote Sensing*, *52*(7), 3947–3958. https://doi.org/10.1109/TGRS.2013.2278297

Cassidy, N. J. (2009). Chapter 2 - Electrical and Magnetic Properties of Rocks, Soils and Fluids. In *Ground Penetrating Radar Theory and Applications* (pp. 41–72). Elsevier. https://doi.org/10.1016/B978-0-444-53348-7.00002-8

Chinh Mai, T. (2022). Simulation study on the influence of a dielectric constant gradient in the concrete on the direct wave of GPR measurements. *Journal of Materials and Engineering Structures*, *2022*(9), 621–627. https://doi.org/127X

Costen, F., Berenger, J.-P., & Brown, A. K. (2009). Comparison of FDTD Hard Source With FDTD Soft Source and Accuracy Assessment in Debye Media. *IEEE Transactions on Antennas and Propagation*, *57*(7), 2014–2022. https://doi.org/10.1109/TAP.2009.2021882

Dagenbach, A. (2012). *Untersuchung der hydraulischen Bodeneigenschaften durch GPR: Analyse der Kapillarsaumreflexion durch numerische Simulationen* (Doctoral dissertation). Heidelberg University Library. https://doi.org/10.11588/heidok.00013527

Denham, W. W. (1982). Two millennia of natura non facit saltum is enough. *Department of Anthropology, Dartmouth College*, *Version 1/22/2014*.

Du, S. (1996). *Determination of water content in the subsurface with the ground wave of ground penetrating radar: Zugl.: München, Univ., Diss., 1996*. Utz Verl. Wiss.

Ernst, J. R. (2007). *2-D finite-difference time-domain full-waveform inversion of crosshole georadar data* (Doctoral dissertation). ETH Zurich. https://doi.org/10.3929/ETHZ-A-005465651

Galagedara, L. W., Redman, J. D., Parkin, G. W., Annan, A. P., & Endres, A. L. (2005). Numerical Modeling of GPR to Determine the Direct Ground Wave Sampling Depth. *Vadose Zone Journal*, *4*(4), 1096–1106. https://doi.org/10.2136/vzj2004.0143

Giannopoulos, A. (2005). Modelling ground penetrating radar by GprMax. *Construction and Building Materials*, *19*(10), 755–762. https://doi.org/10.1016/j.conbuildmat.2005.06.007

Giannopoulos, A. (2012). Unsplit Implementation of Higher Order PMLs. *IEEE Transactions on Antennas and Propagation*, *60*(3), 1479–1485. https://doi.org/10.1109/TAP.2011.2180344

Gosselin, J. M., Dosso, S. E., Askan, A., Wathelet, M., Savvaidis, A., & Cassidy, J. F. (2022). A review of inverse methods in seismic site characterization. *Journal of Seismology*, *26*(4), 781–821. https://doi.org/10.1007/s10950-021-10047-8

Grote, K., Hubbard, S., & Rubin, Y. (2003). Field-scale estimation of volumetric water content using ground-penetrating radar ground wave techniques. *Water Resources Research*, *39*(11). https://doi.org/10.1029/2003WR002045

Grote, K., Crist, T., & Nickel, C. (2010). Experimental estimation of the GPR groundwave sampling depth. *Water Resources Research*, *46*(10). https://doi.org/10.1029/2009WR008403

Gulevich, O., Volkomirskaya, L., Mingalev, I., Varenkov, V., Suvorova, Z., Akhmetov, O., Mingalev, O., & Reznikov, A. (2022). Results of numerical modelling of the problem of video pulse ground penetrating radar research in freshwater bodies. *Russian Journal of Earth Sciences*, 1–6. https://doi.org/10.2205/2022ES000808

Hanafy, S., & al Hagrey, S. A. (2006). Ground-penetrating radar tomography for soil-moisture heterogeneity. *GEOPHYSICS*, *71*(1), K9–K18. https://doi.org/10.1190/1.2159052

Hugenschmidt, J., & Loser, R. (2008). Detection of chlorides and moisture in concrete structures with ground penetrating radar. *Materials and Structures*, *41*(4), 785–792. https://doi.org/10.1617/s11527-007-9282-5

Huggett, R. (1999a). Catastrophism. In *Environmental Geology* (p. 74). Kluwer Academic Publishers. https://doi.org/10.1007/1-4020-4494-1_51

Huggett, R. (1999b). Gradualism. In *Environmental Geology* (pp. 298–299). Kluwer Academic Publishers. https://doi.org/10.1007/1-4020-4494-1_160

Huisman, J. A., Hubbard, S. S., Redman, J., & Annan, A. P. (2003). Measuring Soil Water Content with Ground Penetrating Radar.

Igel, H. (2017). *Computational seismology: A practical introduction* (First edition). Oxford University Press.

Irving, J. D., & Knight, R. J. (2005). Effect of antennas on velocity estimates obtained from crosshole GPR data. *GEOPHYSICS*, *70*(5), K39–K42. https://doi.org/10.1190/1.2049349

Irving, J. D., & Knight, R. J. (2006). Numerical simulation of antenna transmission and reception for crosshole ground-penetrating radar. *GEOPHYSICS*, *71*(2), K37–K45. https://doi.org/10.1190/1.2187768

Jackson, J. D., & Müller, K. (Eds.). (2020). KAPITEL 7. EBENE ELEKTROMAGNETISCHE WELLEN UND WELLENAUSBREITUNG. In *Klassische Elektrodynamik* (pp. 315–394). De Gruyter. https://doi.org/10.1515/9783112322291-013

Kalogeropoulos, A., van der Kruk, J., Hugenschmidt, J., Busch, S., & Merz, K. (2011). Chlorides and moisture assessment in concrete by GPR full waveform inversion. *Near Surface Geophysics*, *9*(3), 277–286. https://doi.org/10.3997/1873-0604.2010064

Kamberaj, H. (2022). *Electromagnetism: With Solved Problems* (1st ed. 2022). Springer International Publishing; Imprint Springer. https://doi.org/10.1007/978-3-030-96780-2

Kearey, P., Brooks, M., & Hill, I. (2013). *An Introduction to Geophysical Exploration* (3., Auflage). John Wiley & Sons.

Klenk, P., Jaumann, S., & Roth, K. (2015). *Monitoring infiltration processes with high-resolution surface-based Ground-Penetrating Radar*. https://doi.org/10.5194/hessd-12-12215-2015

Klotzsche, A. (2013). *Full-waveform inversion of crosshole GPR data for hydrogeological applications: Zugl.: Aachen, Techn. Hochsch., Diss., 2013* (Vol. 193). Forschungszentrum Jülich. http://hdl.handle.net/2128/5641

Klotzsche, A., van der Kruk, J., Angelo Meles, G., Doetsch, J., Maurer, H., & Linde, N. (2010). Full-waveform inversion of cross-hole ground-penetrating radar data to characterize a gravel aquifer close to the Thur River, Switzerland. *Near Surface Geophysics*, *8*(6), 635–649. https://doi.org/10.3997/1873-0604.2010054

Lampe, B. (2003). *Finite-difference time-domain modeling of ground-penetrating radar antenna systems* (Doctoral dissertation). ETH Zurich. https://doi.org/10.3929/ETHZ-A-004619791

Liner, C. L. (2016). *Elements of 3D seismology* (Third edition, Vol. No. 19). Society of Exploration Geophysicists. https://doi.org/10.1190/1.9781560803386

Liu, S., & Sato, M. (2005). Transient radiation from an unloaded, finite dipole antenna in a borehole: Experimental and numerical results. *GEOPHYSICS*, *70*(6), K43–K51. https://doi.org/10.1190/1.2106048

Liu, X., Chen, J., Cui, X., Liu, Q., Cao, X., & Chen, X. (2019). Measurement of soil water content using ground-penetrating radar: a review of current methods. *International Journal of Digital Earth*, *12*(1), 95–118. https://doi.org/10.1080/17538947.2017.1412520

Mangel, A. R., Moysey, S. M., & Kruk, J. (2017). Resolving Infiltration-Induced Water Content Profiles by Inversion of Dispersive Ground-Penetrating Radar Data. *Vadose Zone Journal*, *16*(10), 1–11. https://doi.org/10.2136/vzj2017.02.0037

Mangel, A. R., Moysey, S. M., & van der Kruk, J. (2015). Resolving precipitation induced water content profiles by inversion of dispersive GPR data: A numerical study. *Journal of Hydrology*, *525*, 496–505. https://doi.org/10.1016/j.jhydrol.2015.04.011

Martel, C. (2002). *Modelling and Design of Antennas For Ground-Penetrating Radar Systems*. University of Surrey; Guildford.

Meles, G. A. (2011). *New developments in full waveform inversion of GPR data* (Doctoral dissertation). ETH Zurich. https://doi.org/10.3929/ETHZ-A-006878075

Meles, G. A., van der Kruk, J., Greenhalgh, S. A., Ernst, J. R., Maurer, H., & Green, A. G. (2010). A New Vector Waveform Inversion Algorithm for Simultaneous Updating of Conductivity and Permittivity Parameters From Combination Crosshole/Borehole-to-Surface GPR Data. *IEEE Transactions on Geoscience and Remote Sensing*, *48*(9), 3391–3407. https://doi.org/10.1109/TGRS.2010.2046670

Mozaffari, A., Klotzsche, A., Zhou, Z., Vereecken, H., & van der Kruk, J. (2022). 3-D Electromagnetic Modeling Explains Apparent-Velocity Increase in Crosshole GPR Data-Borehole Fluid Effect Correction Method Enables to Incorporating High-Angle Traveltime Data. *IEEE Transactions on Geoscience and Remote Sensing*, *60*, 1–10. https://doi.org/10.1109/TGRS.2021.3107451

Neal, A. (2004). Ground-penetrating radar and its use in sedimentology: principles, problems and progress. *Earth-Science Reviews*, *66*(3-4), 261–330. https://doi.org/10.1016/j.earscirev.2004.01.004

Ojha, C. S. P., Berndtsson, R., & Bhunya, P. (2008). *Engineering hydrology*. Oxford University Press.

Olhoeft, G. R. (Ed.). (1998). *Electrical, magnetic and geometric properties that determine ground penetrating radar performance*. The University of Kansas, Lawrence, KS, USA.

Pled, F., & Desceliers, C. (2022). Review and Recent Developments on the Perfectly Matched Layer (PML) Method for the Numerical Modeling and Simulation of Elastic Wave Propagation in Unbounded Domains. *Archives of Computational Methods in Engineering*, *29*(1), 471–518. https://doi.org/10.1007/s11831-021-09581-y

Prokopovich, I., Popov, A., Pajewski, L., & Marciniak, M. (2018). Application of Coupled-Wave Wentzel-Kramers-Brillouin Approximation to Ground Penetrating Radar. *Remote Sensing*, *10*(2), 22. https://doi.org/10.3390/rs10010022

Robertsson, J. O. A., & Blanch, J. O. (2020). Numerical Methods, Finite Difference. In H. K. Gupta (Ed.), *Encyclopedia of Solid Earth Geophysics* (pp. 1–9). Springer International Publishing. https://doi.org/10.1007/978-3-030-10475-7_135-1

Robinson, M. (2017). *Hydrology: Principles and Processes*. IWA Publishing. http://site.ebrary.com/lib/alltitles/docDetail.action?docID=11369383

Rubin, Y., & Hubbard, S. S. (2005). *Hydrogeophysics* (Vol. 50). Springer.

Ruffet, C., Darot, M., & Guguen, Y. (1995). Surface conductivity in rocks: a review. *Surveys in Geophysics*, *16*(1), 83–105. https://doi.org/10.1007/BF00682714

Sperl, C. (1999). *Erfassung der raum-zeitlichen Variation des Bodenwassergehaltes in einem Agrarökosystem mit dem Ground-penetrating-Radar: Zugl.: München, Techn. Univ., Diss., 1999* (Als Ms. gedr, Vol. 37). Shaker.

Steelman, C. M., & Endres, A. L. (2010). An examination of direct ground wave soil moisture monitoring over an annual cycle of soil conditions. *Water Resources Research*, *46*(11). https://doi.org/10.1029/2009WR008815

Taflove, A., & Hagness, S. C. (2010). *Computational electrodynamics: The finite-difference time-domain method* (3rd ed., [Nachdr.]). Artech House.

Taflove, A., Hagness, S. C., & Piket-May, M. (2005). Computational Electromagnetics: The Finite-Difference Time-Domain Method. In *The Electrical Engineering Handbook* (pp. 629–670). Elsevier. https://doi.org/10.1016/B978-012170960-0/50046-3

Tronicke, J., & Holliger, K. (2004). Effects of gas- and water-filled boreholes on the amplitudes of crosshole georadar data as inferred from experimental evidence. *GEOPHYSICS*, *69*(5), 1255–1260. https://doi.org/10.1190/1.1801942

van der Kruk, J. (2001). *Three-dimensional imaging of multi-component ground penetrating radar data: Zugl.: Zürich, Diss. Techn. Univ. Delft, 2001*. Technische Universiteit Delft. https://doi.org/10.3929/ethz-a-004168281

van der Kruk, J., Arcone, S. A., & Liu, L. (2007). Fundamental and Higher Mode Inversion of Dispersed GPR Waves Propagating in an Ice Layer. *IEEE Transactions on Geoscience and Remote Sensing*, *45*(8), 2483–2491. https://doi.org/10.1109/TGRS.2007.900685

van der Kruk, J., Jacob, R. W., & Vereecken, H. (2010). Properties of precipitation-induced multilayer surface waveguides derived from inversion of dispersive TE and TM GPR data. *GEOPHYSICS*, *75*(4), WA263–WA273. https://doi.org/10.1190/1.3467444

van der Kruk, J., Liu, T., Mozaffari, A., Gueting, N., Klotzsche, A., Vereecken, H., Warren, C., & Giannopoulos, A. (2018). GPR full-waveform inversion, recent developments, and future opportunities. *2018 17th International Conference on Ground Penetrating Radar (GPR)*, 1–6. https://doi.org/10.1109/ICGPR.2018.8441667

van der Kruk, J., & Slob, E. C. (2002). Effective source wavelet determination. In S. Koppenjan & H. Lee (Eds.), *Ninth International Conference on Ground Penetrating Radar* (pp. 144–149). SPIE. https://doi.org/10.1117/12.462231

van der Kruk, J., Streich, R., & Green, A. G. (2006). Properties of surface waveguides derived from separate and joint inversion of dispersive TE and TM GPR data. *GEOPHYSICS*, *71*(1), K19–K29. https://doi.org/10.1190/1.2168011

van der Kruk, J., Vereecken, H., & Jacob, R. W. (2009). Identifying dispersive GPR signals and inverting for surface wave-guide properties. *The Leading Edge*, *28*(10), 1234–1239. https://doi.org/10.1190/1.3249780

Visser, H. J. (2012). *Antenna Theory and Applications* (1st ed.). John Wiley & Sons Incorporated. https://ebookcentral.proquest.com/lib/kxp/detail.action?docID=844065

Warren, C., & Giannopoulos, A. (2022). *gprMax User Guide: Release 3.1.6*. Retrieved January 11, 2023, from https://docs.gprmax.com/en/latest/index.html

Warren, C. (2009). *Numerical modelling of high-frequency ground-penetrating radar antennas* (Doctoral dissertation). The University of Edinburgh. https://era.ed.ac.uk/handle/1842/4074

Warren, C. (2021). GprMax - Open Source Software to Simulate Electromagnetic Wave Propagation for Ground Penetrating Radar. *Engineering and Mining Geophysics 2021*, 1–2. https://doi.org/10.3997/2214-4609.202152258

Wu, T., & King, R. (1965). The cylindrical antenna with nonreflecting resistive loading. *IEEE Transactions on Antennas and Propagation*, *13*(3), 369–373. https://doi.org/10.1109/TAP.1965.1138429

Yee, K. (1966). Numerical solution of initial boundary value problems involving maxwell's equations in isotropic media. *IEEE Transactions on Antennas and Propagation*, *14*(3), 302–307. https://doi.org/10.1109/TAP.1966.1138693

Yilmaz, Ö. (Ed.). (2001). *Seismic Data Analysis*. Society of Exploration Geophysicists. https://doi.org/10.1190/1.9781560801580

Zadhoush, H., & Giannopoulos, A. (2022). Optimizing GPR time-zero adjustment and two-way travel time wavelet measurements using a realistic three-dimensional numerical model. *Near Surface Geophysics*, *20*(2), 208–226. https://doi.org/10.1002/nsg.12193

Zhang, M., Feng, X., Bano, M., Xing, H., Wang, T., Liang, W., Zhou, H., Dong, Z., An, Y., & Zhang, Y. (2022). Review of Ground Penetrating Radar Applications for Water Dynamics Studies in Unsaturated Zone. *Remote Sensing*, *14*(23), 5993. https://doi.org/10.3390/rs14235993

List of Figures

2.1 GPR resolution can be divided into two parts: range resolution and lateral or angular resolution (Annan, 2005). 9
2.2 Typical surface (upper row) and crosshole (bottom row) GPR survey modes (adapted from Zhang et al., 2022). Tx denotes the transmitter and Rx the receiver. 10
2.3 Demonstration of Snell's law (adapted from Kearey et al., 2013). 11
2.4 GPR wavefront spreading. 12
2.5 Typical ray paths (a) and corresponding B-scan (b), adapted from Annan (2005). 13
2.6 Predicted sampling depths z_s of DGW for 250 MHz antennas vary among different models (Grote et al., 2010). 13

3.1 Single FDTD Yee cell. 20
3.2 Cross-section of the RLFLA model in gprMax. All units are given in cm. 22
3.3 Cross-section of the borehole model in gprMax (TM mode). 23
3.4 Cross-section of gradient model in gprMax 24
3.5 Schematic permittivity and velocity distribution of the gradient model shown in Fig. 3.4 with a dimensionless depth. The height h of the gradient layer is denoted with a red line. 24
3.6 Flowchart for creating and processing the model shown in Fig. 3.4. 25
3.7 Ricker wavelet with 200 MHz center frequency. 25
3.8 B-Scans for a homogeneous halfspace in 2D for $\epsilon_{r,1} = 5$ and a Hertzian dipole excited with a 200 MHz Ricker wavelet and a mesh size of 1 cm. 26

4.1 Demonstration of algorithm for first break picking. 28
4.2 Simulations in free space for $\Delta x = 5$ m. 28
4.3 Snapshots for a RLFLA placed in free space. 29
4.4 Simulations in water-filled boreholes for $\Delta x = 5$ m. 29
4.5 Snapshots for a RLFLA placed in a water-filled borehole with $r_b = 5$ cm. 30
4.6 Snapshots for a RLFLA placed in a water-filled borehole with $r_b = 10$ cm. 31

5.1 B-scans for homogeneous halfspaces. Each trace in the B-scan is normalized with respect to its absolute maximum. 34
5.2 Snapshots for a homogeneous halfspace with $\epsilon_r = 5$ at 12 ns, 20 ns and 30 ns. 34
5.3 A-Scan for an offset $dx_{25} = 5.3$ m of Fig. 5.1a (homogeneous halfspace with $\epsilon_r = 5$) in (a), and time windows for the DAW and DGW in (b) and (c). 35
5.4 Center frequencies f_c of the DAW and DGW for increasing permittivity in a homogeneous halfspace. 35
5.5 Ratio of the peak amplitude of the DAW and DGW for increasing permittivity in a homogeneous halfspace. 36
5.6 Snapshots for the two-layer case in Fig. 5.7h (strong contrast $\epsilon_{r,1} > \epsilon_{r,k}$ for $h = 50$ cm) at 28 ns, 44 ns and 60 ns. The upper soil layer (dark region) acts as a waveguide. . . . 36
5.7 Trace-normalized B-scans of 2D simulations for the two-layer case with a strong contrast. 39
5.8 Trace-normalized B-scans of 2D simulations for the two-layer case with a weak contrast. 40
5.9 Trace-normalized B-scans of 2D simulations for decreasing permittivity gradients. . . . 41

5.10 Trace-normalized B-scans of 2D simulations for increasing permittivity gradients. 42
5.11 Snapshots for the decreasing gradient in Fig. 5.9h (strong contrast for $h = 50$ cm) at 28 ns, 44 ns and 60 ns. The gradient layer (dark region) acts as a waveguide. 43
5.12 (a): Traces at 4.3 m offset from the B-scans of a two-layer case (Fig. 5.7h) and decreasing gradient (Fig. 5.10h) of a strong contrast for $h = 50$ cm. (b): Time window from 15 to 35 ns for the decreasing gradient. 44
5.13 Wavefield interaction in an increasing permittivity gradient 45
5.14 Snapshots for the increasing gradient in Fig. 5.10h (strong contrast for $h = 50$ cm) at 22 ns, 28 ns and 40 ns. 45
5.15 Demonstration of the amplitude picking algorithm developed by the author. 46
5.16 Frequency analysis of DAW and DGW for the strong (a) and weak contrast (b). 47
5.17 Demonstration of Hilbert gain. 48
5.18 Gain function reveals multiples in selected B-scans with a thickness $h = 50$ cm. 48
5.19 B-scan with a gain function for the two-layer case for a weak contrast with $h = 25$ cm. . 49
5.20 Trace normalized difference B-scan 51
5.21 Traces that are marked at three offsets positions with dashed black lines in the difference B-scan in Fig. 5.20. 52
5.22 B-scan for an increasing gradient with a strong contrast over $h = 50$ cm. The dashed black line denotes the end of the time window for which snapshots are shown in Fig. 5.23. 53
5.23 Snapshots for an increasing gradient with a strong contrast and $h = 50$ cm. 54
5.24 B-scans for an increasing permittivity gradient with a strong contrast ($\epsilon_{r,1} = 5$ and $\epsilon_{r,k+1} = 12.5$) and $h = 50$ cm. The amount of layers k within the gradient is progressively increased as shown in the first row. 55
5.25 Schematic contributions with ray-paths if a LHGW is present for a two-layer case (a) and an increasing permittivity gradient (b). 55
5.26 Calculated two-way travel time vs. depth for the model in Fig. 5.22 56
5.27 Amplitudes and center frequencies along depth for the ground waves in different scenarios. 57
5.28 Snapshots for a two-layer case with a strong contrast ($\epsilon_{r,1} < \epsilon_{r,k}$) and $h = 25$ cm at 20 ns, 34 ns and 40 ns. 58
5.29 B-scans with gain for increasing permittivity gradient with a weak contrast ($\epsilon_{r,1} = 5, \epsilon_{r,k} = 6$) 59
5.30 3D simulation for an increasing gradient with a strong contrast and $h = 50$ cm and a RLFLA as source. 60

A.1 Snapshots of hard and soft sources (Meles, 2011). A3
A.2 The NMO geometry for a single horizontal reflector, with its travel time described by a hyperbola according to Eq. (A.5) (Yilmaz, 2001). A3
A.3 B-scans of 2D simulations with gain for the two layer case with a strong contrast. A5
A.4 B-scans of 2D simulations with gain for the two layer case with a weak contrast. A6
A.5 B-scans of 2D simulations with gain for a decreasing permittivity gradient. A7
A.6 B-scans of 2D simulations with gain for an increasing permittivity gradient. A8

List of Tables

2.1 Typical values of relative permittivity (real component) and static conductivity for common subsurface materials at an antenna frequency of 100 MHz (after Cassidy, 2009). 7

5.1 Cut-off frequencies $f_{cut,0}$ in MHz according to Eq. (5.1) for different heights and permittivities. 37
5.2 Time window of the last trace, at 10.1 m offset, where shingling reflections are present in the two-layer and decreasing gradient case. The respective times are manually picked by the author. 43
5.3 Average peak amplitude ratio of DAW and DGW for a weak contrast. 46
5.4 Average peak amplitude ratio of DAW and DGW for a strong contrast. 46
5.5 Events labeled in Fig. 5.22. The * denotes the estimated NMO velocity. 52
5.6 Measured and calculated arrival times of the LHGW. 56

A

Appendix

A.1. Soft and hard sources

In numerical modeling, sources can be classified as hard or soft sources. When it comes to hard sources, a prescribed electric field or voltage is applied at the source location i_{tx} and j_{tx}, varying with respect to time t. For a 2D case, it is

$$E_p\big|^{n}_{i_{tx},j_{tx}} = E_s(t_n), \tag{A.1}$$

where

$p =$ polarisation, either x,y,z.

The hard source model is equivalent to the ideal voltage source with zero impedance and for this reason it acts like an PEC, causing reflections of any wave arrived to the source location. For example, hard sources may cause reflections and nonphysical scattering of waves propagating back to the source location (Buechler et al., 1995). This corresponds to an EM problem in which the electric field at some point is known, and we wish to find the values of the radiated field at other points.

A soft source corresponds to an impressed electric current (Taflove & Hagness, 2010):

$$\begin{aligned} E_z\big|^{n+1/2}_{i-1/2,j+1} = C_a(m) E_z\big|^{n-1/2}_{i-1/2,j+1} + \\ + C_b(m) \cdot \left(H_y\big|^{n}_{i-1,j+1} - H_y\big|^{n}_{i,j+1} - J_{ext_z}\big|^{n}_{i-1/2,j+1} \Delta s \right), \end{aligned} \tag{A.2}$$

where $Ca(m)$ and $Cb(m)$ are updating coefficients, which are functions of ϵ, σ and Δt. Here Δs denotes the grid spatial interval.

The primary benefit of using a soft source is its transparency to incoming waves, which enables various incident fields to interact (Taflove & Hagness, 2010). The implementation of soft sources can pose challenges in terms of correctly positioning them within a Yee cell and may give rise to non-propagating modes that are artificially generated. These modes can cause transient or persistent E and H fields in the near-field near the source, which can result in errors of up to 20% of the corresponding analytical solution. It is important to emphasize that if the goal is to obtain the response to a particular electric current density J, then only soft sources can be used. Whereas the physical meaning of J is well understood from Maxwell's equation, there is no analytical solution or explicit expression available for hard sources (Meles, 2011).

The response to the current excitation in the radiation pattern for an infinitesimal dipole is mainly a negative differentiation, as shown by Arcone (1995), in which the wavenumber factor in the solution acts as a differential operator. The period of response corresponds to the duration of the excitation. If a voltage excitation is used, the respective electric field will be proportional to the second derivative of the pulse.

Implementation in gprMax To model hard sources in gprMax, one can utilize the `#voltage_source` command and set the internal resistance to zero. This configuration specifies exactly the value of the electric field component (Warren & Giannopoulos, 2022). After the waveform has reached a zero amplitude it behaves as a small PEC structure meaning $E = 0$. This can cause any incident waves to be reflected. Including resistance may reduce the late tie resonance in the transmitted signal and make the source more transparent to any incident waves (Warren, 2009).

Soft sources can be implemented in gprMax by using the `#hertzian_dipole` command, in which a current density $\hat{J}_{ex}$ term in Maxwell's equations at an electric field location is specified (Warren & Giannopoulos, 2022). The Hertzian dipole, also called the ideal dipole, has a very short length ($D << \lambda$) and a current uniformly distributed along its length. The current has a constant spatial extent, meaning that it does not vary with distance along the dipole. The time dependence of the current on this dipole can be specified with the excitation waveform. While achieving a discontinuous current distribution can be challenging in practical implementation, a Hertzian dipole proves to be extremely valuable for analyzing larger wire antennas. By subdividing them into shorter sections with uniform currents, such as ideal dipoles, we can utilize superposition to determine the fields of a long wire antenna (Visser, 2012). According to Buechler et al. (1995), the following relation for infinitesimal current source models holds:

$$\bar{J}_{ex} = \frac{\bar{I}\Delta l}{\Delta x \Delta y \Delta z}, \tag{A.3}$$

where

$\bar{I}$ = infinitesimal current element.

Eq. (A.3) shows that gprMax sets the length of the Hertzian dipole Δl to the length of the cell in the polarization direction of the dipole, and creates a dipole moment, $\bar{I} \cdot \Delta l$). So, by only changing the spatial resolution of the model, a different source (dipole moment) is specified that leads to differently scaled results (Warren, 2009). Also, it can be expected that this representation will be limited in accuracy near the source, and that validity starts at distances of about six cells or more from the source, independent of cell size (assuming $\Delta l < \frac{\lambda}{10}$) (Buechler et al., 1995).

Relationship between soft and hard sources The first order approximation relationship of the soft and hard source can be defined as a time integration, provided there are no other incident electric fields (Costen et al., 2009):

$$E_S(t') = -\frac{1}{3\epsilon_0 \Delta x \Delta z} \int_{-\infty}^{t} I_S\,(t')\,dt' \tag{A.4}$$

In case of other incident fields radiated from other sources, this relation does not hold because the incident field is prescribed to be zero at the hard source location, according to Eq. (A.1). In case of other incident fields, the hard source acts as a soft source plus a PEC condition. Meles (2011) visually demonstrated that using the hard source field can be found by time-differentiating the soft source field if the same source wavelet is used; see Fig. A.1.

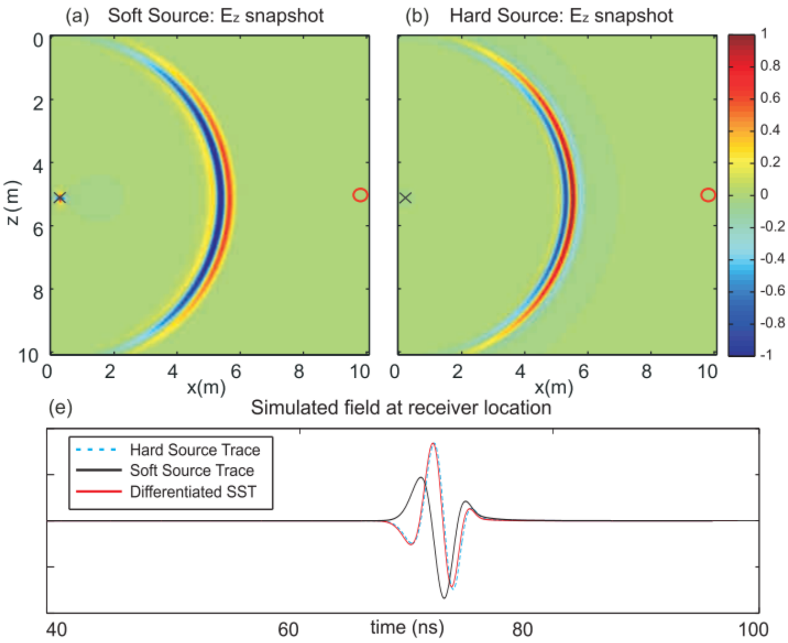

Figure A.1: Snapshots of the vertical component of the electric field corresponding to the same differentiated Gaussian pulse implemented as a soft (a) and a hard (b) source in a homogeneous model. e) Shows that the time differentiation of the soft source trace approximates the hard source trace (Meles, 2011).

A.2. NMO for a flat reflector

For a single constant-velocity horizontal layer, the reflection travel time curve as a function of offset takes the shape of a hyperbola, as explained in section 2.2.5. The time difference between the travel time at a given offset and the travel time at zero offset is known as normal moveout (NMO). The velocity required to correct for NMO is referred to as the *normal moveout velocity*. The equation describing the hyperbolic travel time is linear in the t^2 - x^2 plane (Yilmaz, 2001, p.273).

At a specific midpoint location M in Fig. A.2, the objective is to calculate the reflection travel time t along the ray path from the shot position S to the depth point D, and then back to the receiver position G. By utilizing the Pythagorean theorem, the travel time equation as a function of offset can be expressed as follows (Yilmaz, 2001, p.274):

$$t^2 = t_0^2 + \frac{x^2}{v^2}, \qquad \text{(A.5)}$$

where

x = offset between the source and receiver positions,
t_0 = two-way travel time along the vertical path MD.

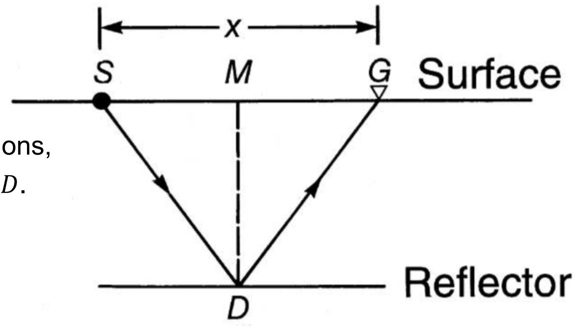

Figure A.2: The NMO geometry for a single horizontal reflector, with its travel time described by a hyperbola according to Eq. (A.5) (Yilmaz, 2001).

If the underlying medium consists of N multiple horizontal layers, like in the gradient layer, the NMO equation is (Yilmaz, 2001, p.280):

$$t^2 = t_0^2 + \frac{x^2}{v_{rms}^2}, \qquad \text{(A.6)}$$

for

$$v_{rms}^2 = \frac{1}{t_0} \sum_{i=1}^{N} v_i^2 \Delta\tau_i, \qquad \text{(A.7)}$$

where

v_i = interval velocity of layer i,
$\Delta\tau_i$ = vertical two-way time through the ith layer.

A.3. B-scans with gain filter

`to be continued on next page`

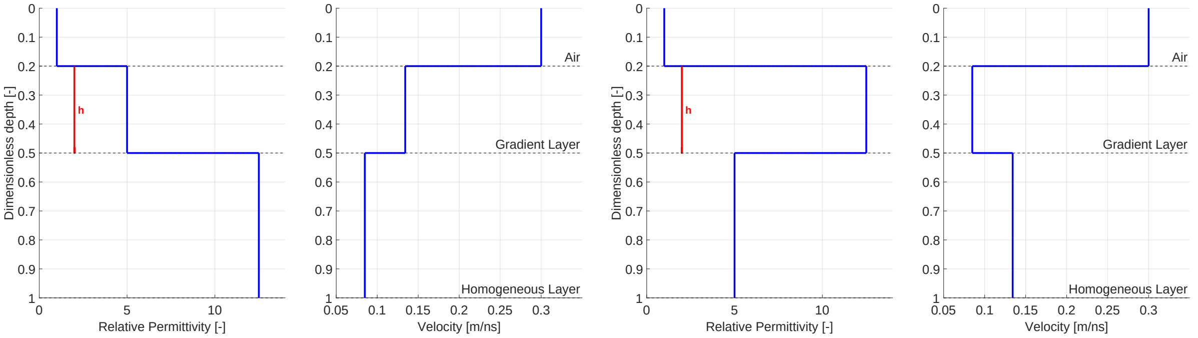

(a) Two-layer case ($\epsilon_{r,1} = 5$ and $\epsilon_{r,k} = 12.5$).

(b) Two-layer case ($\epsilon_{r,1} = 12.5$ and $\epsilon_{r,k} = 5$).

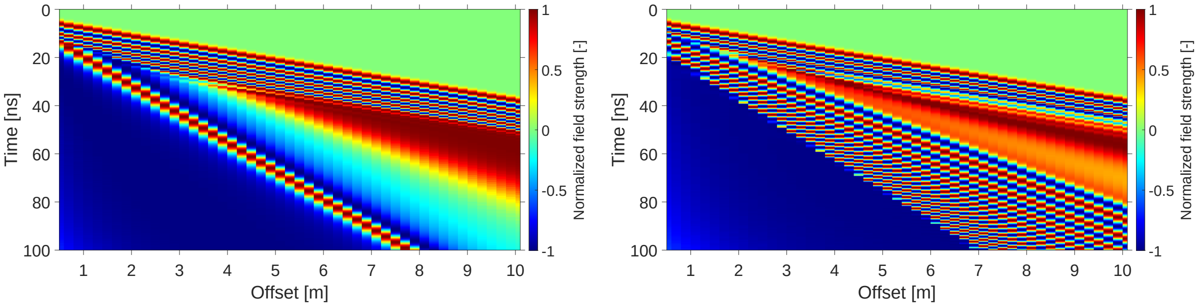

(c) $h = 10\,\text{cm}$.

(d) $h = 10\,\text{cm}$.

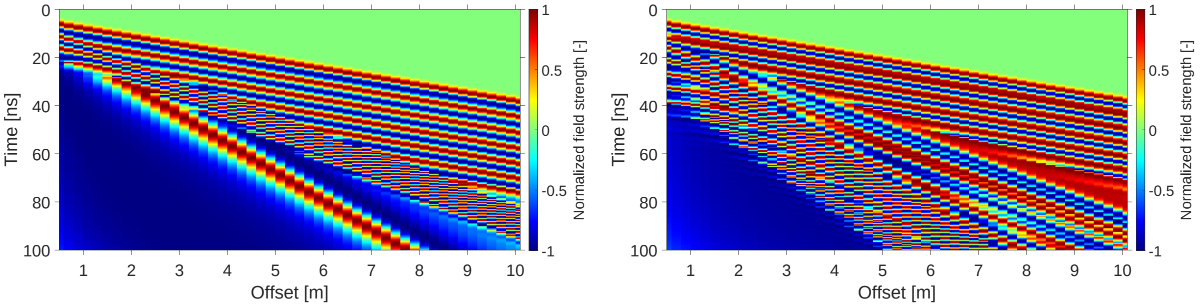

(e) $h = 25\,\text{cm}$.

(f) $h = 25\,\text{cm}$.

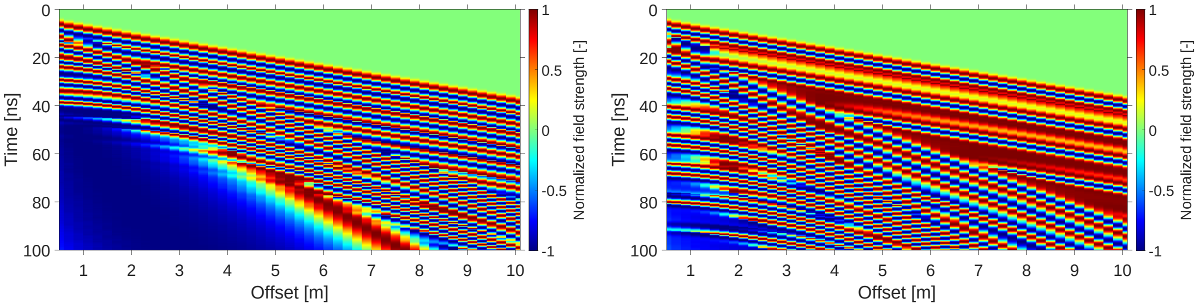

(g) $h = 50\,\text{cm}$.

(h) $h = 50\,\text{cm}$.

Figure A.3: Simulated B-scans for the two-layer case. The left column shows scenarios according to (a), where the thickness h of the gradient layer is increased from $10\,\text{cm}$, $25\,\text{cm}$ to $50\,\text{cm}$. The right column is analogous for the scenario in (b). The Hertzian Dipole is excited with a $200\,\text{MHz}$ Ricker wavelet.

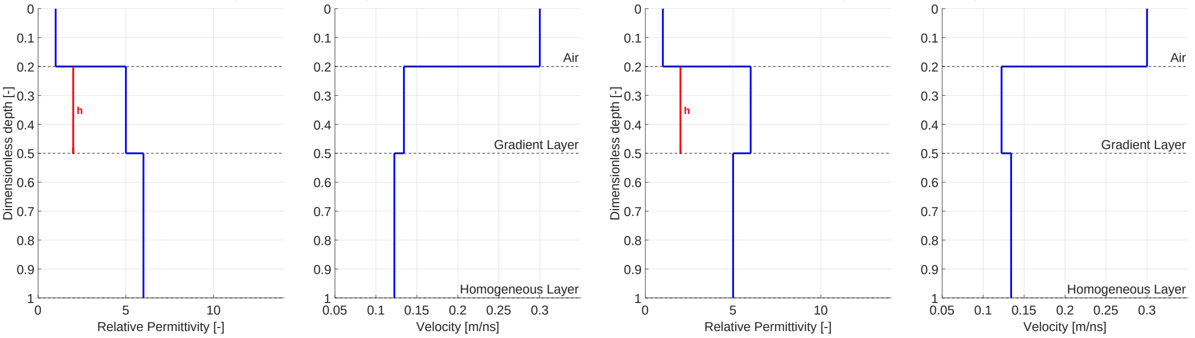
(a) Two-layer case ($\epsilon_{r,1} = 5$ and $\epsilon_{r,k} = 6$).

(b) Two-layer case ($\epsilon_{r,1} = 6$ and $\epsilon_{r,k} = 5$).

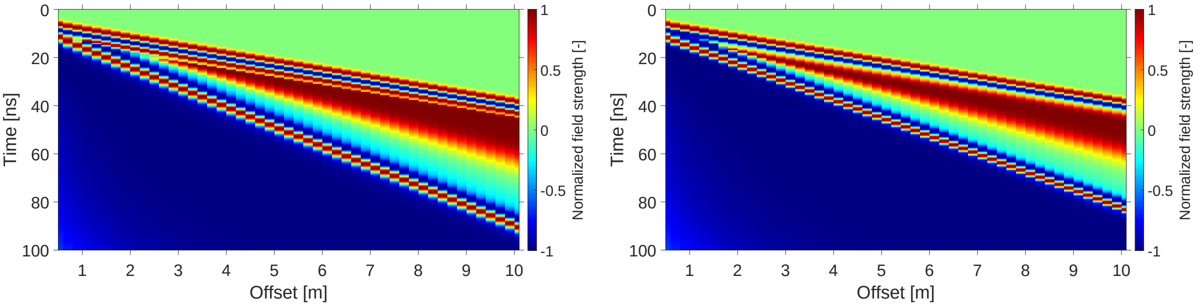
(c) $h = 10\,\mathrm{cm}$.

(d) $h = 10\,\mathrm{cm}$.

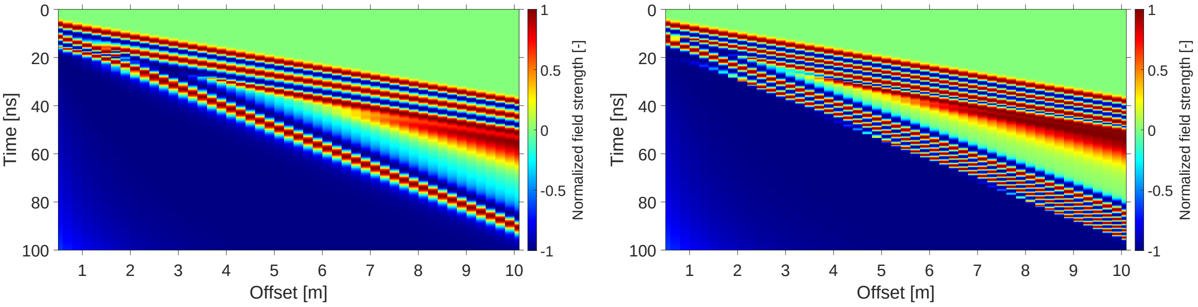
(e) $h = 25\,\mathrm{cm}$.

(f) $h = 25\,\mathrm{cm}$.

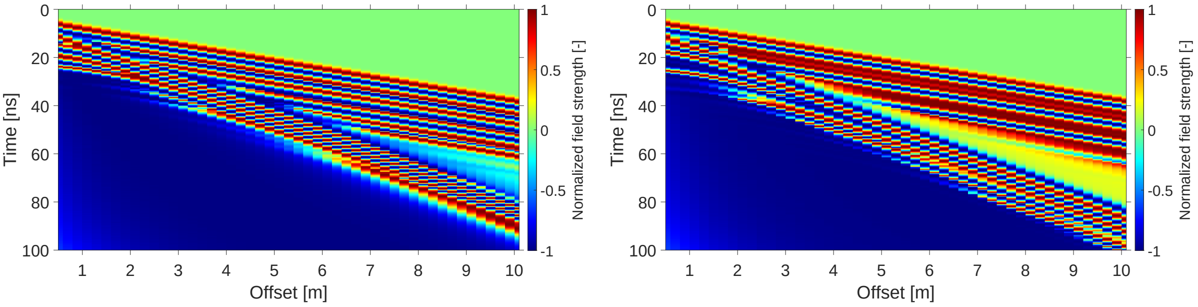
(g) $h = 50\,\mathrm{cm}$.

(h) $h = 50\,\mathrm{cm}$.

Figure A.4: Simulated B-scans for the two-layer case. The left column shows scenarios according to (a), where the thickness h of the gradient layer is increased from $10\,\mathrm{cm}$, $25\,\mathrm{cm}$ to $50\,\mathrm{cm}$. The right column is analogous for the scenario in (b). The Hertzian Dipole is excited with a $200\,\mathrm{MHz}$ Ricker wavelet.

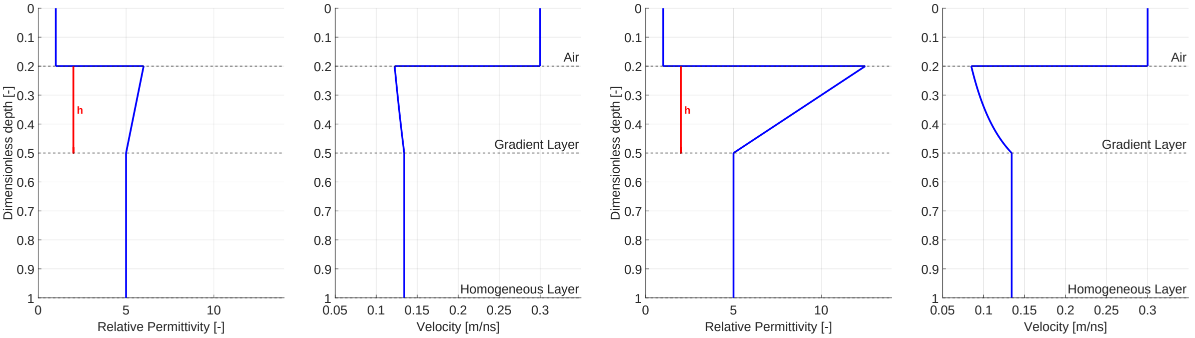

(a) Decreasing gradient ($\epsilon_{r,1} = 6$ and $\epsilon_{r,k} = 5$).

(b) Decreasing gradient ($\epsilon_{r,1} = 12.5$ and $\epsilon_{r,k} = 5$).

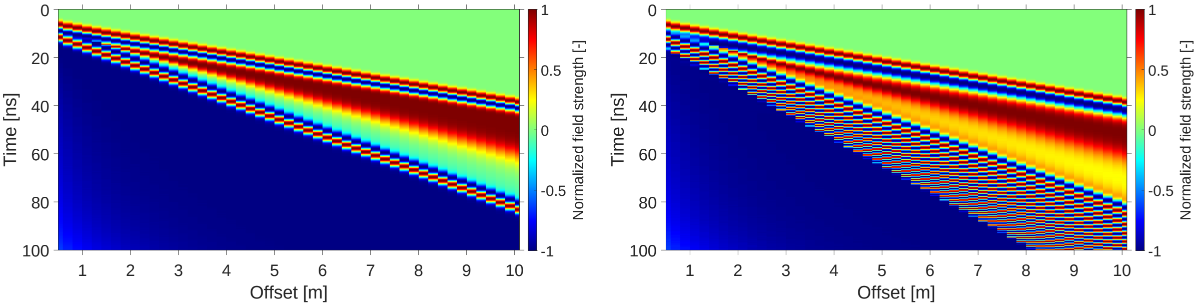

(c) $h = 10\,\mathrm{cm}$.

(d) $h = 10\,\mathrm{cm}$.

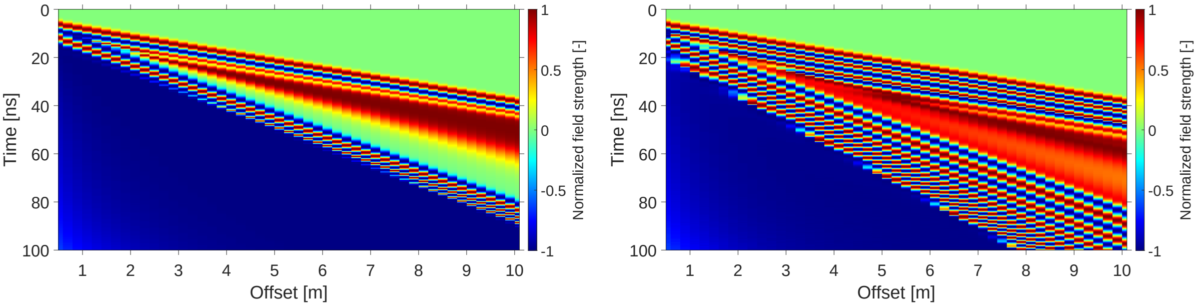

(e) $h = 25\,\mathrm{cm}$.

(f) $h = 25\,\mathrm{cm}$.

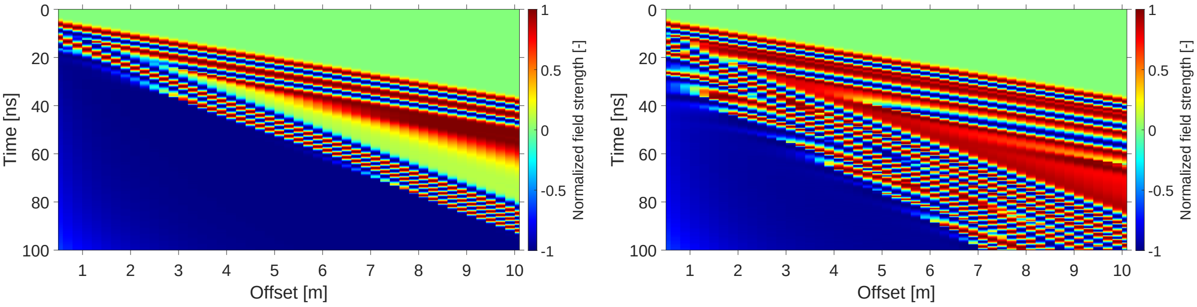

(g) $h = 50\,\mathrm{cm}$.

(h) $h = 50\,\mathrm{cm}$.

Figure A.5: Simulated B-scans for the decreasing gradient case. The left column shows scenarios according to (a), where the thickness h of the gradient layer is increased from $10\,\mathrm{cm}$, $25\,\mathrm{cm}$ to $50\,\mathrm{cm}$. The right column is analogous for the scenario in (b). The Hertzian Dipole is excited with a $200\,\mathrm{MHz}$ Ricker wavelet.

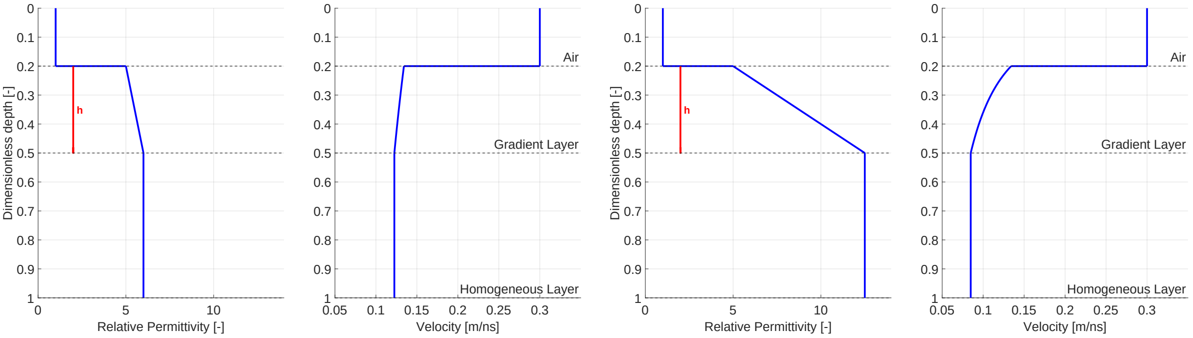

(a) Increasing gradient ($\epsilon_{r,1} = 5$ and $\epsilon_{r,k} = 6$).

(b) Increasing gradient ($\epsilon_{r,1} = 5$ and $\epsilon_{r,k} = 12.5$).

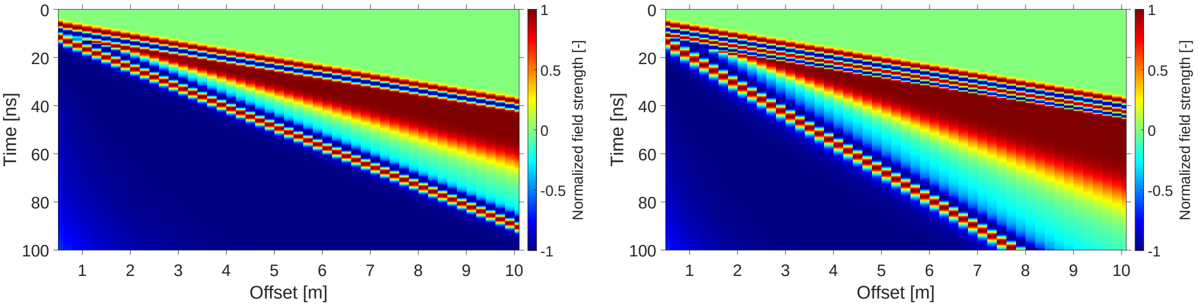

(c) $h = 10$ cm.

(d) $h = 10$ cm.

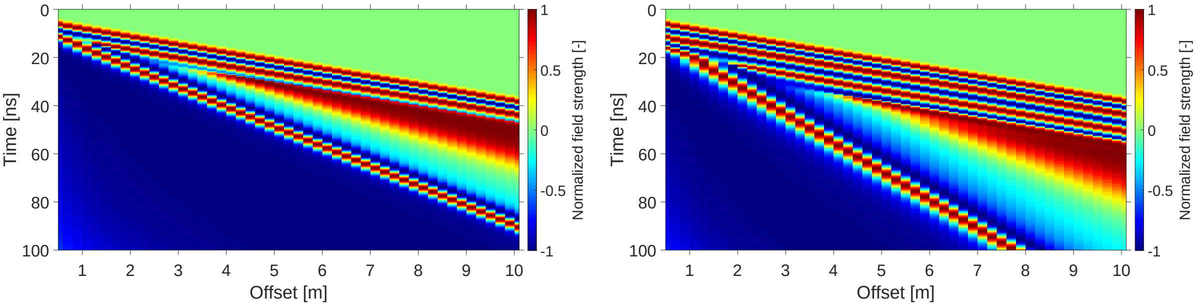

(e) $h = 25$ cm.

(f) $h = 25$ cm.

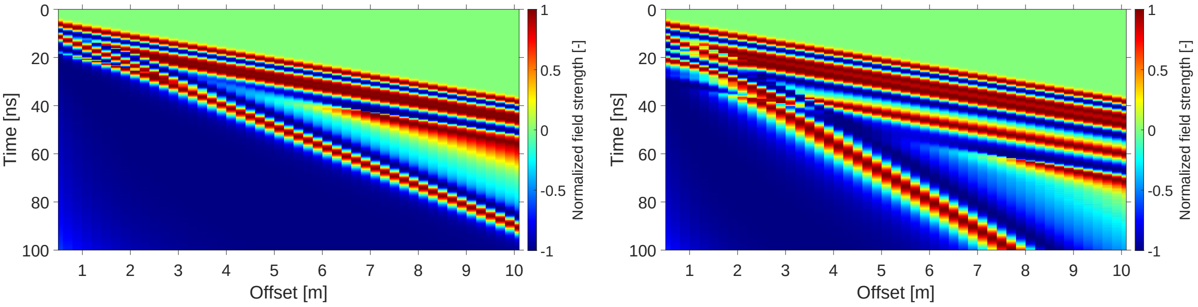

(g) $h = 50$ cm.

(h) $h = 50$ cm.

Figure A.6: Simulated B-scans for the increasing gradient case. The left column shows scenarios according to (a), where the thickness h of the gradient layer is increased from 10 cm, 25 cm to 50 cm. The right column is analogous for the scenario in (b). The Hertzian Dipole is excited with a 200 MHz Ricker wavelet.